Technische Universität München
Lehrstuhl für Fluidmechanik und Prozessautomation

Investigation of Intraoral Mechanical Effects on Sensory Sensations and their Contribution to Mouthfeel

Katrin Mathmann

Vollständiger Abdruck der von der Fakultät Wissenschaftszentrum Weihenstephan für Ernährung, Landnutzung und Umwelt der Technischen Universität München zur Erlangung des akademischen Grades eines

Doktor-Ingenieurs (Dr.-Ing.)

genehmigten Dissertation.

Vorsitzender:		Univ.-Prof. Dr. H.-Chr. Langowski
Prüfer der Dissertation:	1.	Univ.-Prof. Dr. A. Delgado (Friedrich-Alexander-Universität Erlangen-Nürnberg)
	2.	Univ.-Prof. Dr. Th. Becker
	3.	Univ.-Prof. Dr. H. Ulbrich

Die Dissertation wurde am 21.12.2010 bei der Technischen Universität München eingereicht und durch die Fakultät Wissenschaftszentrum Weihenstephan für Ernährung, Landnutzung und Umwelt am 03.06.2011 angenommen.

THERE IS

NO CONCEPTION IN MAN'S MIND

WHICH HATH NOT AT FIRST,

TOTALLY OR BY PARTS,

BEEN BEGOTTEN UPON

THE ORGANS OF SENSE

Thomas Hobbes

Leviathan, 1651

Abstract

The rheology of food capable of flowing has a major impact on human texture perception. To understand intraoral fluid flow greater, a series of tongue-palate models designed to study deglutition from the fluid-mechanical point of view have been presented. *Via* the theory of lubrication three new analytical models have been introduced. In particular, the model of a sphere in a hemisphere has given superior results compared to the established, but simpler, model of Stefan. A more complex geometry, treated numerically, confirmed these findings. The fluid-mechanical quantities obtained from the models employed for the first time give new insights into mechanoreception in the human oral cavity.

Die Rheologie eines fließfähigen Lebensmittels besitzt einen großen Einfluss auf die humane Texturwahrnehmung. Zum besseren Verständnis des intraoralen Fließverhaltens erfolgte die Gegenüberstellung unterschiedlicher Zunge-Gaumen-Modelle, die den Schluckvorgang aus strömungsmechanischer Sicht nachstellen. Die Schmierfilmtheorie ermöglichte die analytische Berechnung drei neuer Modelle. Insbesondere das Modell einer Kugel in einer Halbkugel lieferte Ergebnisse, die dem etablierten, aber einfacheren Modell nach Stefan überlegen sind. Numerische Berechnungen in einer komplexeren Geometrie bestätigten diese Ergebnisse. Die aus den erstmalig eingesetzten Modellen gewonnenen Strömungsgrößen lassen neue Erkenntnisse hinsichtlich der Mechanorezeption in der menschlichen Mundhöhle zu.

Contents

List of Symbols **v**

1 Introduction **1**

1.1 Motivation for Studying Texture 2

1.2 Aim of the Current Thesis 3

1.3 Approach 4

2 State of the Art **7**

2.1 Selected Aspects of Rheology 8

2.2 Fundamentals and Physics of Sensing 9

2.2.1 Definition of Food Texture and Mouthfeel 10

2.2.2 Impacts on Perceived Texture 12

2.2.3 Oral Food Texture Evaluation and Terminology 15

2.2.4 Oral Shear Stresses and Shear Rates 18

2.2.5 Numerical Simulations 23

2.3 Physiology of Texture Perception 27

2.3.1 Classification of the Mechanoreceptors 28

2.3.2 Impulse-Discharge Patterns 29

2.3.3 Occurrence of Mechanoreceptors 31

2.3.4 Comparison between Hand and Tongue 32

2.3.5 Histological Classification of the End Organs 33

2.3.6 Sensitivity 34

3 Analytical Models and Numerical Methods 37

3.1 Geometrical Model of the Oral Cavity 38

3.2 Basic Equations of Fluid Flow 40

3.3 Theory of Lubrication 44

3.3.1 Reynolds Equation 45

3.3.2 Squeezing Flow 50

3.3.3 Plane Circular Parallel Plates - Stefan Equation 51

3.3.4 Plane Elliptic Parallel Plates 57

3.3.5 Plane and Curved Circular Parallel Plates 61

3.3.6 Sphere in a Hemisphere 64

3.3.7 Summary of Analytical Equations 69

3.4 Numerical Simulations 69

3.4.1 Procedure of a CFD Analysis 71

3.4.2 Discretization Methods 72

3.4.3 Types of Grids 73

3.4.4 Software 73

3.4.5 Introduction of the Geometrical Model 76

4 Results and Discussion **79**

4.1 Rheological Measurements and Fittings 80

4.2 Theory of Lubrication 85

4.2.1 Plane Circular Parallel Plates - Stefan Equation 85

4.2.2 Plane Elliptic Parallel Plates 90

4.2.3 Plane and Curved Circular Parallel Plates 95

4.2.4 Sphere in a Hemisphere 99

4.2.5 Conclusion 108

4.3 Numerical Simulations 110

4.3.1 Pressures 112

4.3.2 Velocities 118

4.3.3 Shear Rates 123

4.3.4 Viscosities 128

4.3.5 Shear Stresses 131

4.4 Summary of Analytical and Numerical Findings 133

5 Conclusions **135**

5.1 Analytical Models 136

5.2 Numerical Models 139

5.3 Mechanoreception 142

5.4 Outlook 142

Bibliography **145**

Appendices **157**

A Peer-reviewed Papers **157**

B Calculation of the Arc of Circle **159**

C Code `nonNewtonianIcoDyMFoam` **161**

List of Symbols

There are three different coordinate systems, which are used for the derivation of the different fluid-mechanical models, namely the Cartesian coordinate system (x, y, z), the cylindrical coordinate system (r, φ, z) and the spherical coordinate system (r, φ, θ). The fluid mechanical quantities that are subscribed with these coordinates stand for the components in those directions. Tensor index notation is used for the subscripts i and j. These run from 1 to 3 and represent the coordinates of the different systems.

Latin

A	area
a	semi-major axis of the ellipse
b	semi-minor axis of the ellipse
C_1, C_2	constants of integration
c	clearance
c_e	ratio of the ellipse axes $\frac{b}{a}$
D	shear rate
e_z	eccentricity
F	external force required to drive the different geometries together
f_c	constant used in the ansatz function for plane elliptic parallel plates
g	gravity constant
h	film thickness of a fluid film

h_0	minimal film thickness (1 mm)
m	consistency factor
n	flow-behavior index
p	pressure
p_0	ambient pressure
r	coordinate in radial direction
R	general plate radius or sphere radius (35 mm), respectively
R_1	radius of the key points in the frontal plane
R_2	radius of the key points in the sagittal plane
R_{a1}	minimal averaged radius on the basis of the arc of the circle in the frontal plane (26 mm)
R_{a2}	maximal averaged radius on the basis of the arc of the circle in the sagittal plane (35 mm)
R_{p1}	minimal averaged radius in the transverse projection plane (18 mm)
R_{p2}	maximal averaged radius in the transverse projection plane (29 mm)
t	time
u	velocity
u_{mag}	magnitude of velocity
$\bar{u}$	average velocity
$\dot{V}$	volume flow rate
v_{p}	uniform velocity of the moving geometry part (1 cm/s)
w_0	velocity of the lower movable surface used in the derivation of the Reynolds equation
w_h	velocity of the upper movable surface used in the derivation of the Reynolds equation

Greek

α	constant in the Cross law associated with the rupture of linkages
β	curvature parameter in the plane and curved circular parallel plate model
$\dot{\gamma}$	shear rate
η	dynamic viscosity
η_∞	dynamic infinite-shear viscosity
η_0	dynamic zero-shear viscosity
ν	kinematic viscosity
ν_∞	kinematic infinite-shear viscosity
ν_0	kinematic zero-shear viscosity
ρ	density of the fluid
σ	shear stress
σ_0	yield stress
τ_{ij}	viscous stress tensor
τ_{zr}	shear-stress component perpendicular to the main fluid-flow direction r for cylindrical coordinates
τ_{zz}	normal stress component in z-direction
ψ	angle by which hemispherical shell can be tilted
ω	angular velocity

Chapter 1

Introduction

Foods are evaluated using four principal parameters. These are appearance, flavor, texture and nutrition. Of these, only the last parameter, nutrition, cannot be perceived by the human senses. The other attributes are perceived by the five senses - sight, hearing, smell, taste, and touch.

Appearance is sensed optically with the eyes. Flavor is a matter of the chemical senses. They perceive gustatory and olfactory stimuli by means of the tongue and nose. Texture is a multifaceted parameter mainly sensed by the tactile and kinesthetic senses. Here, the tactile sense refers to touch, the kinesthetic sense to joint position. Moreover, vision and hearing are involved in the process of texture perception.

The process of texture perception is a sequence of several impressions. Thinking of an apple as an example, we first evaluate its texture visually. We look at shape and color and check if the apple is undamaged. Afterwards, we bite into it while listening to the quality of the crunching sound. Last but not least, we start to chew the apple and therefore employ our tactile and kinesthetic senses in order to evaluate the texture from a mechanical point of view. Our brain combines all these sensations and makes a decision about the quality of the apple.

This sequence of steps takes place subconsciously. We will only pay attention to them if the texture of the apple is different from our expectation. Nevertheless, the food will be

rejected if the expectations are not met. For that reason, the food industry is more and more interested in designing perfect textures to keep customers. Hence, food texture and texture perception are worth a closer glance.

1.1 Motivation for Studying Texture

Texture perception and mouthfeel are sensory variables that only came into the focus of research in the 1960s, whereas flavor has been studied for a much longer time. As a result, these concepts still need basic understanding and further clarification. The early attempts of research in this field consisted of work establishing terminology, definitions and concepts of food texture as well as determining the different factors that affect perception. Soon it became obvious that texture is a collective term with many facets. One mode of sensing is not enough to collect a comprehensive impression of all the textural information of food. Nevertheless, there is a consensus in the literature that texture and mouthfeel are dominated by mechanical attributes. These attributes cover a wide range from hardness-related to viscosity-related terms. Although concentrating only on mechanical stimuli, it is obvious that the description of texture exhibits much more complexity than flavor, which can be related to individual chemical compounds.

Due to this complexity, a reliable method to describe mouthfeel quantitatively by means of physical measurements is currently missing. Nevertheless, finding such a method is the desired and ultimate aim of food-texture research. Peleg (1993) aptly states that *"if a 'perceived texture' is, indeed, a sensory response to ... objective mechanical attributes, then the creation of a 'tailored texture' is a realistic possibility"*. This vision of food that is not only harmonious in flavor but also blends well with its texture spurs on food scientists all over the world.

One big challenge is the diversity of foodstuffs. Only taking into account those foods that are capable of flowing slightly reduces the huge variety of foods. There still remains a widespread collection of food that can obviously be distinguished by its fluid-flow behavior.

Every consumer knows from daily-life breakfast experience that the contents of a coffee cup spill widely over the whole table after tipping the cup over while honey is difficult to spread properly on toast. These different behaviors also occur in the oral cavity. They are one aspect by which the consumer judges texture and decides about individual preferences. One branch of research on food texture aims at expressing these experiences with differently behaving foods mathematically. The resulting mathematical models should act as a basis for understanding the food-consumer interaction objectively.

The most important terms describing texture and mouthfeel for foods capable of flowing are viscosity-related terms. Hence, some studies dealing with sensory evaluations of food thickness are available as well as some others discussing the shear rates and stresses that occur in the mouth. So far the fluid mechanical quantities occurring in the mouth have been quantified by both experimental approaches and calculations. These quantities are said to be detected by the oral mechanoreceptors and give an idea about the mechanically-induced mouthfeel sensations. For this reason, one of the aims of food-texture research is to close the existing gap between instrumental and human sensory measurements.

1.2 Aim of the Current Thesis

The current thesis concentrates on the calculation of fluid flow in several oral model systems. The models introduced increase in complexity. The simple models are solved analytically by means of the theory of lubrication. The advanced models, with a geometry that is based on dentist replicas, require numerical treatment. Evaluating the results of these analytical fluid-mechanical investigations gives good estimates of the order of magnitude of the different fluid-mechanical quantities.

The analytical calculations help to estimate the influence of different geometries on fluid flow. The numerical simulations visualize vector fields of fluid-flow variables in a more complex geometry. Moreover, a model including a non-Newtonian fluid is introduced. This is interesting as most foodstuffs capable of flowing are non-Newtonian fluids.

The current thesis reviews literature concerning the concept of texture, existing models of the oral cavity, and the fundamentals of mechanoreception. Subsequently, the different models of the oral cavity are introduced and the results of the calculations are discussed and compared. The final validation of each flow variable is accomplished by means of comparison to existing literature values. Hence, the present thesis provides a more detailed insight into the fluid-mechanical processes in the oral cavity than ever before.

1.3 Approach

The analytical approaches that have been employed so far all relate to a well-known tongue-palate model system consisting of two plane circular parallel plates. This system can roughly mimic the squeezing flow that occurs during deglutition (swallowing) and gives an idea of the expected order of magnitude of fluid-mechanical quantities. Nevertheless, this analytical approach lacks a geometry that is closer to reality.

The in-mouth models employed in the current thesis enable the investigation of fluid-flow processes in the oral cavity that accompany consumption. Two approaches are introduced, an analytical one and a numerical one. Concerning the analytical one, first of all the established geometry of two plane circular parallel plates is introduced. This geometry is well described concerning all fluid-mechanical quantities as it is often used as a reference.

The established model is compared to geometries that consider different aspects of the real oral cavity. The first geometry for comparison consists of two plane elliptical parallel plates. The pressures and the force required to drive the geometry together have been known for a long period. Additionally, the current thesis determines velocities, shear rates and shear stresses. The same is performed for a second geometry consisting of a plane and a curved circular parallel plate. Finally, the analytically solvable model of a sphere in a hemisphere is derived from a general approach to lubrication.

The numerical approach employs a geometrical model that is built on average values of oral cavities. The flow of fluids featuring different viscosities is calculated. Here, three

different low viscosities are employed to investigate the effect of small viscosity changes on the distribution of the fluid-mechanical quantities. Additionally, one fluid with a higher viscosity that represents both vegetable oils and the apparent viscosity of yogurt is used. Lastly, a non-Newtonian fluid fitted with the Cross law is implemented in the numerical calculation. This approach of implementing a different flow-curve characteristic is reasonable as most foodstuffs exhibit non-Newtonian fluid flow behavior. This makes the comparison of Newtonian and non-Newtonian results essential as the differences are likely to have a great effect on texture perception.

All the different approaches reveal mechanical stimuli that occur due to the movement of the tongue during deglutition. These stimuli are detected dynamically by the human mechanoreceptors in the oral cavity. The tactile sensation is then transmitted to the human brain. For this reason, this thesis establishes a link to perception. Knowledge of what the mechanoreceptors detect and magnitudes of different physical quantities of fluids within the oral cavity means a novel understanding of the food-consumer interaction.

Chapter 2

State of the Art

This chapter begins with a short introduction to the idea of rheology. This is necessary as the term is frequently used when dealing with texture and mouthfeel. Thereafter, the sensory, physical and physiological fundamentals of texture perception are presented. Starting with the concept of texture, definitions, influences on perception and terminology of mouthfeel attributes are outlined. In this context, it will be shown that viscosity is the most dominant mouthfeel attribute for food capable of flowing. Therefore, it becomes obvious why the current investigation concentrates on models that mimic the squeezing flow in the oral cavity.

Furthermore, the shear stresses and rates occurring in the mouth that result from experimental investigations and theoretical considerations are discussed. Previous numerical simulations of deglutition have focused on the pharynx and the esophagus as these organs in particular have attracted the attention of medical scientists so far. Their primary aim was the understanding of dysphagia in order to develop a cure for this condition. Nevertheless, numerical models of the oral cavity are rare.

The chapter ends with a short introduction to the physiology of perception. Mechanoreceptors are referred to in many papers dealing with texture perception. Hence, their morphology and functionality are illustrated. An improved knowledge of mechanoreceptors is the basis for understanding the signal transmission from the food through the oral tissues to the brain, which evaluates the sensations.

2.1 Selected Aspects of Rheology

Rheology deals with the deformation and flow of matter in response to an applied stress or strain. The reaction of matter caused by the applied stress or strain is used to characterize rheological behavior (Steffe, 1996). In principle, rheological characteristics can be classified into Newtonian and non-Newtonian behavior. Newtonian fluids feature a constant viscosity, while the viscosity of non-Newtonian fluids depends on the applied shear rate. Typical examples of Newtonian fluid-flow behavior are water, vegetable oils and honey. In contrast, most foods show non-Newtonian behavior (Steffe, 1996, Bourne, 2002).

Rheologists distinguish between some major material behaviors. Figure 2.1 introduces the time-independent characteristics by plotting shear stress σ versus shear rate $\dot{\gamma}$ (Steffe, 1996). Time-dependent models are not considered in the current study due to their complexity. Newtonian fluids exhibit a direct proportionality between shear stress σ and shear rate $\dot{\gamma}$. The slope of the flow curve is the dynamic viscosity η.

Non-Newtonian materials do not feature this direct linear proportionality. However, the local quotient $\frac{\sigma}{\dot{\gamma}}$ is often used to define an apparent viscosity η. If the apparent viscosity η decreases with an increasing shear rate $\dot{\gamma}$, the material is said to exhibit shear-thinning behavior. An example of this kind of fluid-flow behavior is orange-juice concentrate. The opposite case, where the apparent viscosity η increases with an increasing shear rate $\dot{\gamma}$, is known as shear-thickening behavior. This behavior can be observed in the case of starch solutions (Steffe, 1996).

Both, the Bingham and the Herschel-Bulkley fluids are said to require a minimum applied stress to make them deform and flow. This stress is called the yield stress σ_0. Below this yield stress, the material behaves like a solid. Its value can be read off the y-axis intercept. Above this yield stress, when the matter flows, the curves can show a linear proportionality between shear stress σ and shear rate $\dot{\gamma}$ once again (Bingham) or a shear-thinning characteristic (Herschel-Bulkley). Tomato paste is said to comply with the Bingham model, ketchup with the Herschel-Bulkley model (Steffe, 1996). However, the yield-stress concept has been criticized as being an idealization, which has arisen due to

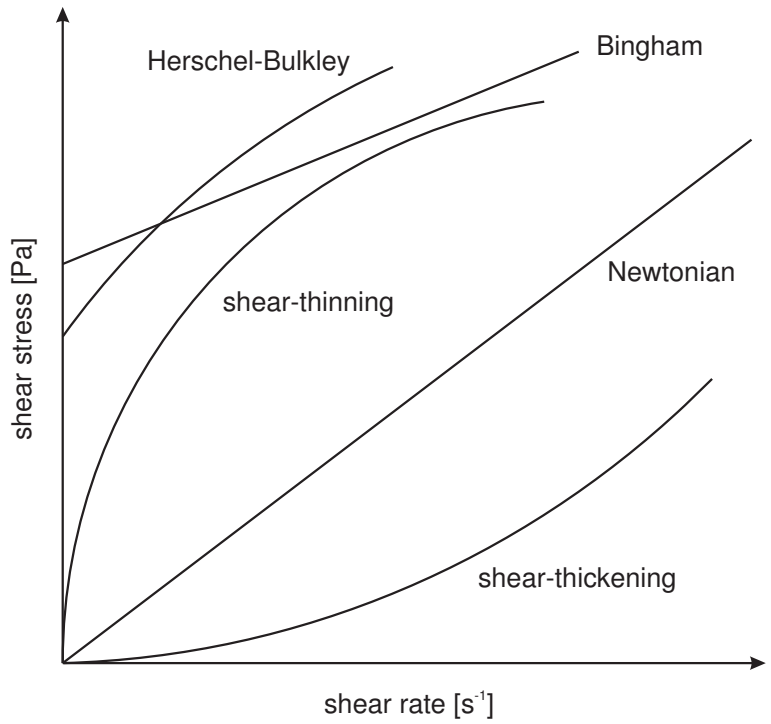

Figure 2.1: A survey of different flow behaviors of time-independent fluids (Steffe, 1996).

a lack of accurate measurements. Barnes & Walters (1985) have stated that the yield stress does not exist.

There are numerous approaches to approximate real fluid-flow behavior by analytical functions. These flow equations are usually based on empirical investigations. A theoretical background is seldom. The free parameters of the models are determined from experimental data (Böhme, 2000).

2.2 Fundamentals and Physics of Sensing

The second part of this literature review deals with texture and mouthfeel. Several definitions developed over the last decades are introduced. Possible influences on texture and mouthfeel are outlined, followed by presenting the terminology in general and the adapted terminology for food capable of flowing. Afterwards, strategies to quantify oral shear stresses and shear

rates are outlined. The section closes with a summary of numerical studies that have been employed previously in order to visualize the process of swallowing.

2.2.1 Definition of Food Texture and Mouthfeel

Scientists have long been aware of the importance of flavor for consumer acceptance. However, the multi-parameter attribute texture has only attracted attention since the 1960s (Szczesniak, 2002). There are several definitions of food texture presented in the literature. Some of them take only one kind of foodstuff into consideration whereas others are more general.

In one of her early publications Szczesniak (1963) defined that texture can be *"considered as the composite of the structural elements of food and the manner in which it registers with physiological senses"*. A few years later, Muller (1969) regarded the concept of texture as confusing because it relates to both a physical and a perceived property. He suggested a separation in the terms "rheology" and "hapaesthesis" instead. According to this concept, rheology is measured objectively in SI units, while hapaesthesis is recorded by means of statistical investigations.

Although Szczesniak tried to define texture in 1963, she admitted in the same paper that a clearer appreciation of the concept must be worked out. She recognized that *"a rigorous definition of texture will have to await a better understanding of the basic principles involved, especially those concerned with rheological or mechanical properties of food"*. Following her, these early definitions have been updated continuously.

Texture was much debated in the 1970s. Sherman (1970) refined the definition of Szczesniak (1963) saying that texture is *"the composite of those properties (attributes) which arise from the structural elements of food and the manner in which it registers with physiological senses"*. With this definition he wanted to emphasize that single aspects of texture are measurable instrumentally and are thereby quantifiable. By comparison, Jowitt (1974) suggested that texture is *"the attribute of a substance resulting from a combination of physical properties and perceived by the senses of touch (including kinesthesis and mouth-*

feel), sight and hearing. Physical properties may include size, shape, number, nature and conformation of constituent structural elements". Discussions on this topic continued in the 1980s and 1990s.

In 2002, Bourne confirmed that one fundamental property of texture is that it has various single attributes, which yield a multifaceted collective term. One of the most recent definitions was published by Szczesniak (2002) after she had spent her whole professional career investigating texture. She concluded that *"texture is the sensory and functional manifestation of the structural, mechanical and surface properties of foods detected through the senses of vision, hearing, touch and kinesthetics"*. She emphasized the four aspects that texture

- is a sensory property,
- is a multi-parameter attribute,
- derives from the structure and
- is detected by several senses.

Texture evaluation requires at least three of the five available human senses. Most information is obtained by touch. Sight and hearing deliver additional details. Smell and taste sense flavor-active molecules. In the case of creaminess, both texture scientists (Kokini & Cussler, 1983) and flavor scientists (Schlutt, Moran, Schieberle & Hofmann, 2007) claim the right to define the characteristics of the attribute. Hence, it is even questionable as to whether a clear differentiation between flavor and texture is ultimately practicable.

de Wijk, Terpstra, Janssen & Prinz (2006) explain that the properties of food are perceived at distinct points in time. Flavor is always the first property that is analyzed, followed by textural properties. Thickness is the first textural attribute that is rated. Its immediate perception means that it is not influenced significantly by the mixture with and dilution effects of saliva (van Aken, Vingerhoeds & de Hoog, 2007). Some sensations like creaminess need intensive movement and processing by the tongue to be evaluated.

The importance of texture is pointed out by Szczesniak & Kahn (1971). They state that food texture will scarcely be noticed as long as it complies with the expectation of the consumer. But if it differs from this expectation the food will be criticized and rejected. For this reason, the authors are of the opinion that the importance of texture should not be underestimated and that it is necessary to bring *"texture awareness ... to the conscious level"*. Most people are only able to deal with the concept after they have been made familiar with its terms and vocabularies.

Mouthfeel is related closely to texture. Jowitt (1974) establishes the connection that mouthfeel arises from *"those textural attributes of a food responsible for producing characteristic tactile sensation on the surfaces of the oral cavity"*. This means that texture perception and therefore mouthfeel can be related to the mechanical behavior of the investigated food sample.

2.2.2 Impacts on Perceived Texture

According to Engelen & van der Bilt (2008), there is a missing link between physical measurements and texture perception, which can possibly be found in physiology. While measurements only evaluate strictly physical properties of materials, human subjects judge food by manipulating it during oral processing. All the changes that occur due to the processing can hardly be mimicked by technical instruments. Figure 2.2 provides an overview of possible direct and indirect influences on texture perception, which may be interwoven. The physiological aspects of oral sensitivity, tongue movements, temperature and saliva composition are especially emphasized by the authors. They conclude that oral physiology can presumably explain some of the inter-individual variation. The current study focuses on tongue movement and the resulting fluid flow in the oral cavity. The importance of the other effects is beyond doubt, but neglected here due to the restrictions of the employed models. In order to give an idea about these aspects, example studies are introduced below.

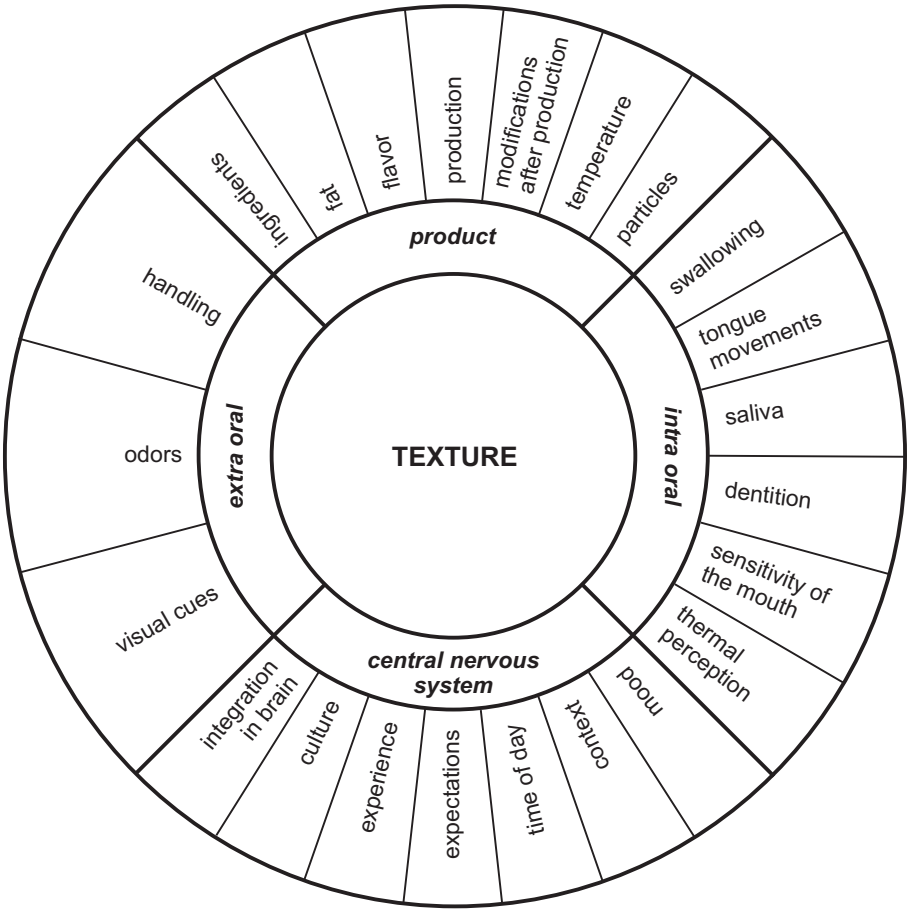

Figure 2.2: The possible direct and indirect influences on texture perception [adapted from Engelen & van der Bilt (2008)].

Oral Sensitivity

In general, oral sensitivity is difficult to define precisely. Many different influences and their interactions play a decisive role. For particles in suspensions, these influences are size, shape and hardness of the particles. Tyle (1993) investigated the phenomena of grittiness. He found that particles up to about 80 µm in size are not perceived as gritty if they are soft and round or hard and flat. However, hard and angular particles of 11 to 22 µm size evoked the sensation of grittiness.

Peleg (2006) states that there is no constant sensitivity in humans. People can judge very soft and very hard food with a maximum sensitivity at intermediate stiffnesses. At

both ends of the scale, however, they have difficulties to discriminate.

Strassburg, Burbidge, Delgado & Hartmann (2007) found similar results. The authors investigated the oral evaluation of the thickness of flexible circular disks. These disks had a constant diameter of 3 mm and a constant elastic modulus of 480 MPa. Their thicknesses ranged from 12.5 µm to 350 µm. A range from 125 µm to 190 µm thickness could be found in which the disk geometries could not be discerned by the tactile senses in the mouth although the difference between two consecutively evaluated disks lies above the known threshold of 25 µm.

Temperature

Temperature has a crucial influence on food thickness. Food has an initial temperature when consumption starts. This temperature changes during consumption due to the thermal diffusivity of the food and the oral temperature. This change in temperature is followed by a viscosity change (Stanley & Taylor, 1993). The thickness of semi-solid foodstuff decreases significantly with an increasing product temperature.

According to Rao (1977), the change of viscosity in foods due to temperature can be calculated by

$$\eta = Be^{\frac{E}{RT}}, \tag{2.1}$$

which is known as the Arrhenius equation. Here, η stands for the viscosity, B for a constant, E for the activation energy, R for the gas constant and T for the temperature. The equation is valid for both Newtonian and non-Newtonian fluids. The constant B is dependent on the weight fraction of total solids.

Engelen, de Wijk, Prinz, Janssen, Weenen & Bosman (2003) also investigated the influence of the oral temperature on thickness perception. For that purpose, they asked their subjects to rinse their mouths with water of different temperatures immediately before tasting. The oral tissues slightly changed their temperature due to this procedure. The same

tempered product was evaluated to have different subjective thicknesses due to the different temperatures in the oral cavity. This effect is small, but present.

Saliva

Saliva is a viscoelastic fluid with a varying viscosity between 2 mPas and 13 mPas at high and low shear rates (Roberts, 1977). It alters the properties of food during consumption by warming and diluting the solution in the mouth, resulting in an inhomogeneous mixture (Christensen & Casper, 1987). Stanley & Taylor (1993) claimed that the dilution effect is too small to be significant, but it was observed to decrease the tendency for turbulent flow in thin solutions (Christensen, 1984). Less turbulent flow will, in turn, lead to decreased perceived viscosity (Parkinson & Sherman, 1971). The effects of saliva are not taken into consideration in the current study as the duration of the process of deglutition is short compared to the time of possible interactions of saliva with the samples.

2.2.3 Oral Food Texture Evaluation and Terminology

Christensen (1984) states that texture perception is a very complex process. Texture perception requires an active manipulation and deformation of the food, which in turn modifies the physical properties. van Aken et al. (2007) emphasized that it is necessary to apply a little oral processing before swallowing and perceive the attributes at or shortly after food intake for this reason.

Szczesniak (1963) defined three main classes of textural characteristics:

- mechanical characteristics - reactions according to stress,
- geometrical characteristics - arrangement of the constituents/appearance and
- other characteristics that refer mainly to moisture and fat content.

The mechanical characteristics can be classified in the five primary groups

- hardness,
- cohesiveness,
- viscosity,
- elasticity and
- adhesiveness.

Every attribute is evaluated on a reference scale. Each rating on the specific scale is standardized with a specific product of a specific brand and manufacturer. Hence, the sensory results are reproducible. This approach is called sensory texture profiling.

In the early 1970s, a sub-committee on Sensory Analysis of the British Standards Institution worked on food texture terminology. JOWITT, a member of this committee, proposed the first list of food texture terminology in 1974 in order to achieve a general international agreement. His list included

- the definition of general terms (structure, texture, consistency),
- an itemization of material behavior under applied stress or strain including definitions,
- terms describing material structure (particle size or shape, shape and arrangement of structural elements) and
- an itemization and definitions of mouthfeel characteristics.

Additionally, JOWITT suggested a term be defined for those sensations that cannot be related to textural properties but also influence mouthfeel, like astringency and temperature. The general terminology includes all texture attributes for both solid and fluid food. This is not appropriate for food capable of flowing. For this reason, special terminologies were developed.

SZCZESNIAK (1979) introduced a list of mouthfeel attributes, which arise due to the consumption of beverages. Table 2.1 gives an overview of the occurring attributes, which

are grouped into distinct categories. The second column declares the relative frequency attributes of a specific category were mentioned. Obviously, the viscosity-related terms are dominant when describing the mouthfeel of beverages but are not the only terms.

Table 2.1: The classification of mouthfeel terms for beverages (Szczesniak, 1979).

Category	[%]	**Typical words**
viscosity-related terms	30.7	thin, thick, viscous
feel on soft tissue surfaces	17.6	smooth, pulpy, creamy
carbonation-related terms	11.2	bubbly, tingly, foamy
body-related terms	11.2	heavy, watery, light
chemical effect	7.3	astringent, burning, sharp
coating of oral cavity	4.5	mouthcoating, clinging, fatty, oily
resistance to tongue movement	3.6	slimy, syrupy, pasty, sticky
afterfeel - mouth	2.2	clean, drying, lingering, cleansing
afterfeel - physiological	3.7	refreshing, warming, thirst quenching, filling
temperature-related	4.4	cold, hot
wetness-related	1.3	wet, dry

Pollen, Daubert, Prabhasankar, Drake & Gumpertz (2004) investigated the quantifying of liquid food texture using a reduced set of characteristics, which can be understood by means of rheological measurements. The study is built up on the example of six commercial products featuring different properties: tomato ketchup, condensed milk, caramel topping, chocolate syrup, salad dressing and pancake syrup. Concerning the oral properties, the authors only distinguished between the viscosity-related properties consistency (force required to slurp the sample off a spoon) and thickness (thickness of the sample after 3 s of tongue manipulation), and the yield-stress related property slurp (force required to initiate flow on a spoon by gently slurping).

2.2.4 Oral Shear Stresses and Shear Rates

Janssen, Terpstra, de Wijk & Prinz (2007) state that the exact range of shear rates in the mouth is not known, although several attempts employing different strategies have been undertaken in order to find a remedy. Some scientists came from an experimental background, others from a mathematical one. These approaches are presented separately in the following sections.

Experimental Approaches

First approaches, for example the approach from Stevens & Guirao (1964), established empirical relationships in terms of a power function between subjective and objective attributes of viscosity emanating from perception and rheology. A pioneer in this field of research was Wood (1968) who characterized different foodstuffs and a Newtonian solution rheologically. Equivalent shear stresses and shear rates occur at the intersection points of the Newtonian curve with the non-Newtonian curves in a diagram of shear stress *vs* shear rate.

Panelists were asked to evaluate the viscosities of the non-Newtonian foods compared to the Newtonian solution. The non-Newtonian foods that came closest in perceived consistency defined the shear-rate range employed for the oral evaluation. Wood concluded that the shear rate that is relevant for the perception of thickness is about $50\,s^{-1}$. He hypothesized that the corresponding shear stress is the perceived stimulus.

Years later, Cook, Hollowood, Linforth & Taylor (2003) confirmed this hypothesis by stating that shear stress is the stimulus that is used for the oral evaluation of viscosity. Thus, it has a special meaning for the somatosensory sense (see chapter 2.3). Apart from the detection of flow by means of the mechanoreceptors located in the surfaces of the oral tissues, the solution's resistance to flow is detected by the intramuscular receptors of the kinesthetic sense (Christensen & Casper, 1987). They measure the force or effort applied to move the solution.

Employing the same strategy as Wood, Shama & Sherman (1973) investigated oral shear rates and shear stresses over a wider range of food viscosities. Similar foods were grouped together with a Newtonian solution of a comparable viscosity. The area where rheological and sensory measurements agreed was marked by a broken line rectangle in their graph of shear stress *vs* shear rate.

The upper diagram in figure 2.3 shows the resulting rectangles. The two continuous curves represent the approximate limits of shear rates and shear stresses in which foods were evaluated in the oral cavity. It was concluded that oral shear rates lie between $10\,s^{-1}$ and $1000\,s^{-1}$, and the resulting oral shear stresses between 10 Pa and 1000 Pa. Furthermore, the results suggest that stimuli of liquid foods can be traced back to shear rates evaluated at approximately constant shear stresses of about 10 Pa. In viscous foods, shear stresses at an approximately constant shear rate of $10\,s^{-1}$ are responsible for the stimuli.

The lower diagram in figure 2.3 delivers information about the evaluated foods. Their rheological characteristics are superimposed upon the continuous curves in the upper diagram. Hence, it is possible to estimate the shear rate and shear stress that occur in the oral cavity for each single foodstuff.

The correlation between shear rates and stresses, and foodstuffs is quite good. Nevertheless, Christensen (1979) makes the alternative assumption that a certain range of shear rates is always generated in the oral cavity. Panelists evaluate the viscosity of the solution along the whole shear rate range and come up with an averaged viscosity. This would explain why solutions of carboxymethylcellulose of different polymer length but identical viscosity are evaluated to be thinner the more distinct their non-Newtonian behavior is. Cutler, Morris & Taylor (1983) came to a similar conclusion, but added that objective viscosity measurements at $10\,s^{-1}$ correlate well with the perceived thickness of most fluids.

Houska, Valentova, Novotna, Strohalm, Sestak & Pokorny (1998) employed five different sensory methods (mixing with a spoon, pouring from a spoon, slurping from a spoon, compressing between tongue and palate, and swallowing effort) in order to evaluate rheologically-measured samples. The authors established power-law functions between

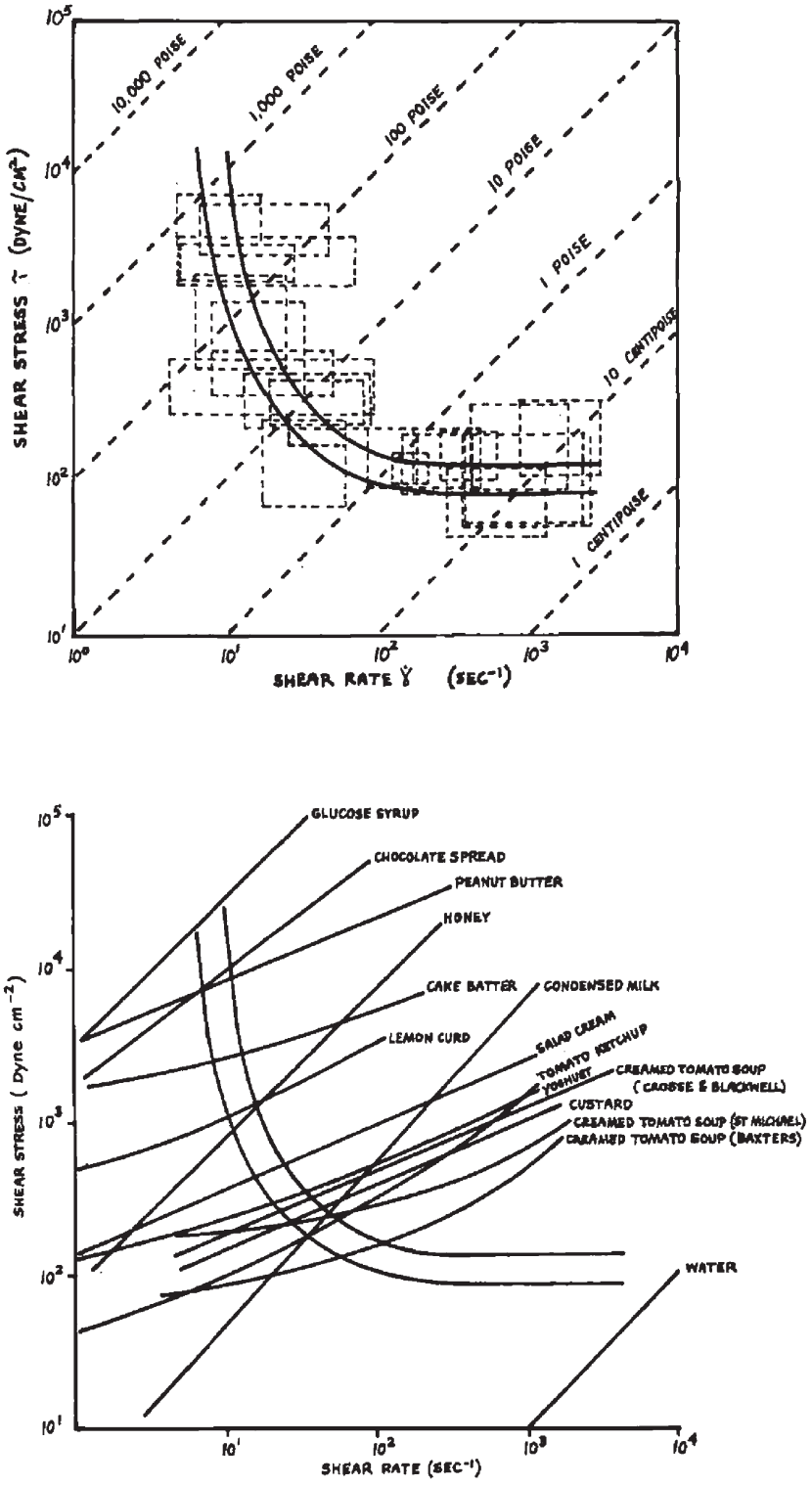

Figure 2.3: The shear rates and shear stresses occurring in the mouth during food evaluation (Shama & Sherman, 1973).

the sensory evaluations and the rheological measurements. They found shear rates up to questionable 15307470 s^{-1} for the slurping of low viscosity strawberry-yogurt drinks.

Other approaches have employed dynamic-viscosity measurements combined with smaller deformations than the steady-shear approaches used before (Stanley & Taylor, 1993). Bistany & Kokini (1983) were the first who showed that the dynamic viscosities are much larger than the steady viscosities. Richardson, Morris, Ross-Murphy, Taylor & Dea (1989) found that the measurements under oscillatory shear at the single frequency of 50 rad/s correlate directly with panel scores for the perceived thickness of solutions with and without yield stress.

Analytical Approaches

Starting in the 1970s, the groups of the researchers Cussler and Kokini developed a mathematical model for the prediction of subjective attributes. In a first attempt, DeMartine & Cussler (1975) developed a set of equations in order to predict the subjective spreadability, viscosity and stickiness evaluated by using one's fingers. The mathematical model was developed in three steps. At first, the fingers were approximated by two parallel plates and the fluid rheology by the power law. Then the film thickness of the fluid was expressed by means of the Stefan equation, which can be derived from the theory of lubrication. This theory is introduced in detail in chapter 3.3. DeMartine & Cussler implemented the power law in the friction term of an equation of squeezing flow and solved the equation for the fluid film. The height of the film is dependent on time, plate radius and fluid rheology. The final step, the prediction, was based on the developed equation. The authors assume proportionalities between spreadability and reciprocal shear rate, viscosity and shear rate, and stickiness and the quotient of the initial height and plate velocity.

The subjects evaluated the samples by using their fingers. Spreadability was evaluated by spreading the sample along a plate with the index finger, viscosity by rubbing the fluid between the fingers and stickiness by removing the finger after touching the fluid on the

plate. These measurements were compared to the results of the equations. The successful fits exhibit correlation coefficients of at least 0.90.

Kokini, Kadane & Cussler (1977) applied the preceding ideas to the tongue-palate system in the mouth. Again, they approximated the tongue and palate by a system of two parallel plates. Ten original attributes were reduced to three, which were related to physical quantities. Thickness was related with viscous forces, smoothness with frictional forces, and slipperiness with a combination of both. The rest of the procedure remains the same as described above.

On the basis of this mathematical model, Dickie & Kokini (1983) calculated the shear rates that are supposed to occur in the mouth. They came out with a range between $5.09\,\mathrm{s}^{-1}$ for thicker foods like marshmallows and $36.50\,\mathrm{s}^{-1}$ for thinner foods such as ketchup assuming the fluids follow the power law.

Elejalde & Kokini (1992) stated that shear stress in the mouth is the sensory mechanism used for the oral evaluation of viscosity. For this reason, they used the model introduced above in order to calculate shear rates and shear stresses. They performed their own study using syrups. Their rheological characterizations yielded shear rates in the range from $11.78\,\mathrm{s}^{-1}$ to $99.78\,\mathrm{s}^{-1}$ and shear stresses in the range from 4.4 Pa to 131 Pa. In order to verify the model, they employed further data published by Cutler et al. (1983). These data led to a minimum shear rate of $10.03\,\mathrm{s}^{-1}$ for lemon curd and a maximum shear rate of $415.99\,\mathrm{s}^{-1}$ for fresh milk. The calculated shear stresses ranged between 1.0 Pa for fresh milk and 683 Pa for chocolate spread.

Other authors enhanced the findings introduced above. Campanella & Peleg (1987) deduced an advanced mathematical model consisting of one rigid and one elastic plate. The elastic plate represents the deformable tissue of the tongue. The authors quantified the effect on the force-time curve dimensionlessly. Nicosia & Robbins (2001) used the rigid set-up in order to investigate the fluid mechanics of bolus ejection from the oral cavity, with close attention regarding the bolus-ejection time.

2.2.5 Numerical Simulations

Numerical simulations in structural and fluid mechanics are a powerful and efficient tool to calculate shear and normal stresses in solid and liquid materials. The method is employed when analytical solutions fail due to the complexity of the geometry. The application of numerical simulations provides the required insight into those complex systems (Datta, 1998).

The area of application is widespread in all disciplines of engineering, ranging from automotive engineering to medical technology. This section gives a concise overview of numerical simulations relating to different aspects of oral biomechanics. The motivation of previous investigations was dominated by medical questions like implant dentistry, rehabilitation after tongue surgeries and dysphagia. Additionally, there is a bionics-motivated study about ram feeding fish.

Nowadays, finite element analysis is a very common method in implant dentistry. Weinstein, Klawitter, Anand & Schuessler (1976) published the first paper in this area of research. They performed a two-dimensional stress analysis in porous rooted dental implants, after which the method gained ground.

At the beginning of the last decade, Geng, Tan & Liu (2001) composed a review paper about the advances in biomechanics of dental implants. Emphasis was put on the prediction of stress on implants and their surrounding bones due to mastication. In this context, the three aspects of bone-implant interface, implant-prosthesis connection and multiple-implant prosthesis are of importance.

Only recently, Wakabayashi, Ona, Suzuki & Igarashi (2008) published another review article about nonlinear finite element analyses for dental applications. The authors state that nonlinear stress-strain relationships mirror the intraoral environment more realistically. The aspects of displacement of periodontal ligament, plastic and viscoelastic behaviors in restoration materials, tooth-to-tooth contact, mechanical contacts of implant prostheses and tooth-restoration complexes were discussed in detail.

Tongue movement is another branch analyzed by means of structural-mechanics approaches. The deformable nature of the tongue turns out to be a great challenge to simulate. Nevertheless, modern computer hardware enables the highly complicated realization of this ambitious objective.

Vogt, Lloyd, Buchaillard, Perrier, Chabanas, Payan & Fels (2006) developed an innovative three-dimensional biomedical finite-element-based simulation of a muscle-activated human tongue with a simulation time ten times larger than real-time. Their intention was to contribute to the clarification of physiological activities like speech production, breathing and swallowing, surgical and dental training, and outcome prediction for clinical procedures.

In a next step, Buchaillard, Brix, Perrier & Payan (2007) extended the model including jaw, palate and pharyngeal walls, as can be seen in figure 2.4. By means of this model, the effect of tissue loss and reconstruction on the tongue movement was studied. In particular, the study deals with two common tongue surgeries used to remove tongue tumors, namely hemiglossectomy, which is the surgical removal of one half of the tongue, and mouth-floor resection. Subsequent reconstruction is modeled implementing flaps of different stiffness. These simulations clarify the potential impact on speech articulation. The long-term perspective is to adapt the simulation individually. The method can thereby contribute to help cancer patients in regaining quality of life.

Oral fluid mechanics has been analyzed only rarely using numerical simulations. Exceptions are some studies of oropharyngeal mechanics for a greater understanding of dysphagia. Chang, Rosendall & Finlayson (1998) and Meng, Rao & Datta (2005) simulate the pharyngeal bolus transport of isothermal, homogeneous and incompressible Newtonian and non-Newtonian fluids. The Newtonian fluid flow was represented using the dynamic viscosity $\eta = 1$ mPas and the density $\rho = 1000$ kg/m^3 as well as the parameters $\eta = 150$ mPas and $\rho = 1800$ kg/m^3. Non-Newtonian behavior was reflected by the power law $\sigma = K\dot{\gamma}^n$. The consistency index was set to $K = 2.0\,\mathrm{Pas}^n$, the flow behavior index $n = 0.7$. As the exponent n is < 1, the fluid-flow behavior is shear-thinning. The pharyngeal bolus transport

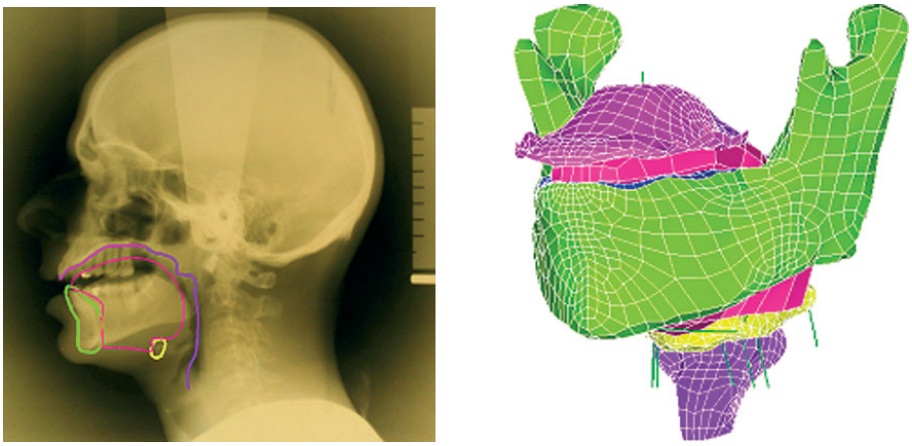

Figure 2.4: An X-ray and finite element model of the tongue in its natural environment of jaw, palate and pharyngeal walls (Buchaillard et al., 2007).

is observed in the 5 cm long segment of the human throat from the glossopalatal junction to the upper esophageal sphincter. This segment is mimicked by an axisymmetric pipe with movable walls. The pipe is closed and widened with a wavelike movement resulting in squeezing of the food.

The intention of the study was to find out which food meets the demands of dysphagia patients best. The swallowing process is safer the longer it lasts as it reduces the risk of aspiration (*i.e.* the process of food entering the trachea and lungs) in consequence of not shutting off the airways. For this reason, the impact of the fluid-flow behavior on swallowing time is studied. The authors discovered that shear-thinning fluid-flow behavior seems to slow down the swallowing process, concluding that non-Newtonian products are safer for dysphagia patients.

Studies of the esophageal bolus transport can be seen as a continuity of the previous study. Li, Brasseur & Dodds (1994) introduced a numerical model of the esophagus. The numerical code was based on the lubrication theory for Newtonian materials, which was adapted appropriately to the description of peristaltic waves traveling along a tube of finite length (Li & Brasseur, 1993). The simulation helped to analyze the relationship between the muscle-induced wall deformation of the esophageal tube and the intraluminal pressure. Yang, Fung, Chian & Chong (2007) utilized the finite element method to

illustrate the interaction of tissue, Newtonian food bolus and the peristaltic wave due to muscle contraction for the first time.

Nicosia (2007) introduces the only model of the oral cavity that deals with fluid mechanics. This model is two dimensional. The palate is represented by a stiff line. The contour of the tongue moves dynamically based on trigonometric functions. Hence, the central gap between tongue and palate decreases and increases again. The junction between the palate and the base of the tongue opens and closes. The Newtonian bolus has the dynamic viscosities 10 mPas, 100 mPas and 1000 mPas. Figure 2.5 illustrates the geometrical configuration for different time steps and shows the behavior of the bolus for a dynamic viscosity of 1000 mPas.

The purpose of the study was to analyze premature bolus spillage into the pharynx as this causes problems for dysphagia patients. It can be concluded that boluses of higher viscosities remain in the oral cavity longer. Additionally, a decreased magnitude of tongue movement is important. Therefore, the use of thickened liquids for dysphagia patients is suggested in order to prevent premature spillage into the pharynx.

Besides the medically-motivated considerations of human swallowing behavior, there is a study with a bionic focus. Cheer, Ogami & Sanderson (2001) investigated the fluid mechanics in the oral cavity of suspension-feeding fish. These fish capture water that contains food by swimming forward continuously with a completely open mouth. The streamed oral cavity of the fish was imitated by simplified cylindrical and conical geometries. Some vertical or slanted branchial slits were included near the outflows. The analysis of the numerical simulations concentrated on the transport of food particles and the velocity profiles of the streaming water. The authors hope to understand the functionality of the gill rakers that

Figure 2.5: The two-dimensional model of bolus containment in the oral cavity according to Nicosia (2007) considering a viscosity of 1000 mPas.

retain food organisms at the gill arch filaments. The ultimate aim of their work is to design industrial hydrosol filtration methods modeled on these effective ram suspension feeders.

2.3 Physiology of Texture Perception

Food texture is perceived by both tactile and kinesthetic senses (Kilcast & Eves, 1991, Christensen, 1984, Verhagen & Engelen, 2006). The tactile sense perceives touch on the surface of the skin. Therefore, this sense transmits stimuli from the environment. The surfaces of the oral cavity that receive this kind of stimuli by means of mechanoreceptors are the tongue, the palate and the pharyngeal regions.

In contrast, the kinesthetic sense is an internal body sense. It delivers information concerning the static position of specific parts of the body and the relative position of several parts to each other. Additionally, it measures the effort required for motion. In the case of the oral cavity this sense is important for the movement of the jaw and tongue. Occurring stimuli are transmitted by proprioceptors. The most relevant receptors in kinesthesis are muscle spindles. They send signals due to changes in their length.

The stimulation of a receptor is followed by a signal transduction pathway *via* nerve cells, the so-called axons. Mechanoreceptors are stimulated by deformations of their cell membrane. These deformations result in an opening of ion channels. In consequence of the ion exchange the cells are depolarized. If a certain threshold of depolarization is achieved an action potential will be sent. This is a temporary change of voltage, which is transmitted from axon to axon to the brain. Long-lasting depolarizations trigger series of action potentials. The frequency of the action potentials decreases with time until the resting potential of the cell is recovered. Hence, a constant stimulation leads to an adaptation of the receptor. Finally, the signal patterns that are sent are decoded and analyzed in the brain (Mörike, Betz & Mergenthaler, 1997, Schmidt, 1998).

2.3.1 Classification of the Mechanoreceptors

As the tactile sense is supposed to be the most relevant one for texture perception, it is presented here. In general, there are four different types of mechanoreceptors. Each of them has different perceptual functions. The single transmitted stimuli responses correspond to a specific tactile sensation (Johnson, 2001).

Jacobs, Wu, Goossens, van Loven, van Hees & van Steenberghe (2002) state that the mechanoreceptors can be distinguished by several properties. The primary classification is based on their velocity of adaptation and on the properties of their receptive field. The slowly-adapting mechanoreceptors are abbreviated SA, the rapidly-adapting ones RA. Furthermore, type-I receptors feature small and distinct receptive fields, while type-II receptors exhibit large and diffuse ones. Table 2.2 illustrates the classification.

A receptive field is the circular- or oval-shaped area, which covers the mechanoreceptive end organs connected with one single afferent nerve (Schmidt, Lang & Thews, 2005). A high sensitivity of mechanoreception is partially associated with a high overlap of the receptive fields (Trulsson & Essick, 1997). The receptive fields of type-I receptors in the glabrous skin of the human hand, which is highly sensitive, overlap by about 20% to 30% (Vallbo & Johansson, 1984).

The microstructure of the receptive fields is characteristic for each kind of mechanoreceptor. Figure 2.6 shows an example of the isosensitivity lines of the receptive fields in the glabrous skin of the human hand. A defined stimulus spreads out from the point of contact

Table 2.2: The classification of mechanoreceptors according to their velocity of adaptation and the properties of their receptive field.

		Characteristic of receptive field	
		Small Distinct	Large Diffuse
Velocity of adaption	Slowly adapting	SA I	SA II
	Rapidly adapting	RA I	RA II

to a line representing a certain sensitivity. Hence, the size of the receptive field increases with the power of the stimulus.

The type-I receptors exhibit a dense occurrence of isosensitivity lines including four to seven sensitivity peaks in case of SA receptors and 12 to 17 in case of RA receptors. These sensitivity peaks can presumably be ascribed to the exact number of end organs or the number of end-organ clusters connected to one parent axon. In contrast, the type-II receptors exhibit sparse isosensitivity lines and only one single sensitivity peak.

Figure 2.7 depicts the detection thresholds along the lines plotted in figure 2.6. The figure represents the smallest detectable level of mechanoreception possible. The abscissa represents the distance in mm. The left ordinate displays the detection threshold as a multiple of the lowest threshold T, the right ordinate the absolute indentation threshold in µm.

The threshold is very low over a wide range in the case of the type-I receptors. It increases to a twentyfold value at the borders of the receptive field. Therewith, the receptive fields of type-I receptors are distinct. These borders are missing in the case of type-II receptors. Here, the sensitivity falls off gently over the complete distance. Furthermore, the threshold only achieves fivefold values comparing the center and border of the receptive field.

The absolute indentation thresholds differ strongly. While the maximum occurring threshold is 50 µm for RA receptors, SA receptors have a threshold of 600 µm and 1000 µm, respectively.

2.3.2 Impulse-Discharge Patterns

The different types of mechanoreceptors respond to different modes of skin deformation (Schmidt et al., 2005). The SA-I mechanoreceptors react to the intensity of skin impression, which is a stress causing deformation from the mechanical point of view. The SA-II mechanoreceptors are sensitive to the intensity of skin stretch, which is equivalent with strain. The RA-I mechanoreceptors respond to the velocity of the skin deformation,

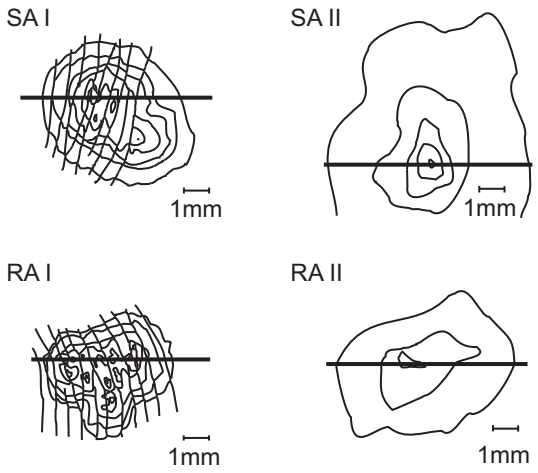

Figure 2.6: The isosensitivity lines in the microstructure of receptive fields of the cutaneous mechanoreceptors of the human hand (Vallbo & Johansson, 1984).

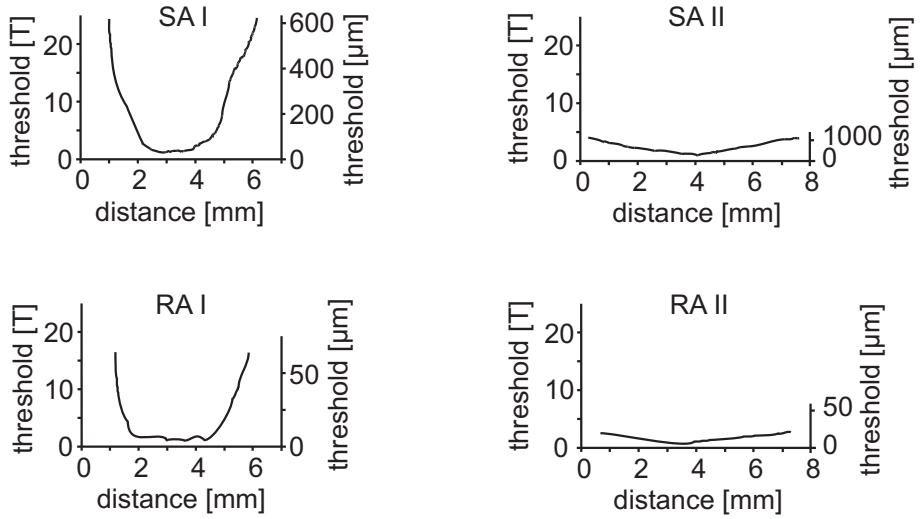

Figure 2.7: The detection thresholds measured relatively in multiples of the lowest threshold T and absolutely in indentation [µm] of receptive fields of the cutaneous mechanoreceptors of the human hand (Vallbo & Johansson, 1984).

while the RA-II mechanoreceptors respond to the acceleration. The temporal gap that occurs between the discharged action potentials is dependent on the intensity of the stimulus in each case.

Figure 2.8 shows the characteristic impulse discharges arising due to a perpendicularly applied stimulus. The skin is deformed with a constant velocity in a first phase. The resulting indentation is retained in a second phase. Finally, the stimulus is removed during a third phase.

The slowly-adapting mechanoreceptors react to both static and dynamic stimuli. In contrast, the rapidly-adapting ones respond only to dynamic impulses (Jacobs et al., 2002). Although the response of mechanoreceptors to stimuli is well known, there is little knowledge about the exact modes of encoding mechanoreceptive signals in the human brain and the formation of sensory assessments in terms of textural attributes (Peleg, 1993, 2006).

2.3.3 Occurrence of Mechanoreceptors

The occurrence of the different kinds of mechanoreceptors depends on the character of the skin. All four types can be found in glabrous skin, while hairy skin lacks the RA-I mechanoreceptors and the oral mucosa the RA-II mechanoreceptors, respectively. Table 2.3 gives an overview of the occurrences of the mechanoreceptors in different kinds of tissue.

Table 2.3: The occurrences of the different mechanoreceptors in the different kinds of tissues [adapted from Jacobs et al. (2002)].

Receptor	**Glabrous skin**	**Hairy skin**	**Oral mucosa**
SA I	+	+	+
SA II	+	+	+
RA I	+	–	+
RA II	+	+	–

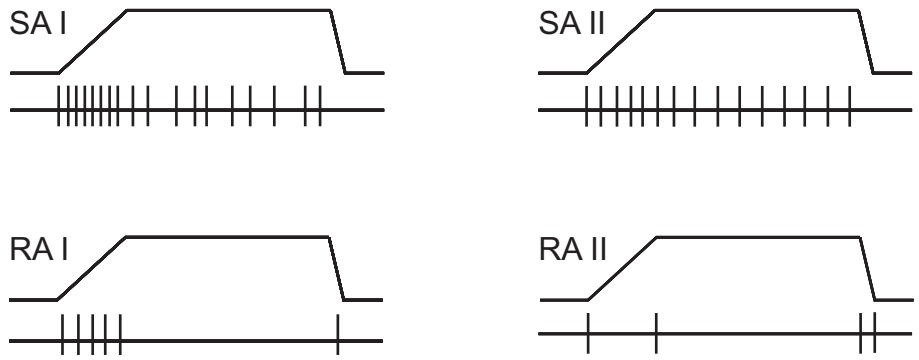

Figure 2.8: The characteristic impulse discharges of the four different kinds of mechanoreceptors arising due to a stimulus in terms of a perpendicularly applied skin deformation (Vallbo & Johansson, 1984).

2.3.4 Comparison between Hand and Tongue

Very little is known about the mechanoreceptors in the tongue. In contrast, the mechanoreceptors of the glabrous skin of the human hand are well investigated. As the structure of both tissues is quite comparable, the knowledge about mechanoreception in the hand is useful for an understanding of the mechanisms in the oral cavity (Trulsson & Essick, 1997). Additionally, the skills of the hand can act as a useful frame of reference. Therefore, table 2.4 compares numbers about the mechanoreceptors in the glabrous skin of the hand (Vallbo & Johansson, 1984) and the mechanoreceptors in the tip of the tongue (Trulsson & Essick, 1997). The numbers are based on 17000 mechanoreceptors for the hand and on 22 for the tongue.

Though the RA II receptors are missing on the tongue the percentile distribution of SA and RA units does not vary significantly between tongue and the glabrous skin of the hand. In both cases the RA units represent about two thirds of the total number of mechanoreceptors. Therefore, the response to dynamic stimuli is predominant. This is different in other parts of the body, where SA receptors are more prevalent (Trulsson & Essick, 1997), such as the hairy skin of the hands and face, the lips and the oral mucosa. It must be assumed that there is a commonness between the different regions: the glabrous skin of the hand and the tongue fulfill explorative and manipulative tasks, while the SA receptors are more attuned

Table 2.4: The values of the mechanoreceptors in the glabrous skin of the human hand (H) (Vallbo & Johansson, 1984) and the mechanoreceptors in the tip of the tongue (T) (Trulsson & Essick, 1997).

	SA I		**SA II**		**RA I**		**RA II**	
	H	T	H	T	H	T	H	T
Occurrence [%]	25	9	19	27	43	64	13	–
Median size of receptive field [mm^2]	11.0	1.0	59	5.3	12.6	2.0	101	–
Diameter assuming circular receptive fields [mm]	3.7	0.36	8.7	2.6	4.0	0.5	11.3	–
Innervation density per cm^2	70	–	10	–	140	–	20	–
Detection threshold [mN]	–	0.19	–	0.31	–	0.11	–	–

to proprioception.

The median size of the receptive fields is generally smaller at the tip of the tongue than at the hand. This confirms that the tactile acuity of the tongue is by far bigger than in any other part of the body. The innervation density, along with the overlap of the receptive fields, is an index for the sensitivity of mechanoreception (Trulsson & Essick, 1997). These densities are not known for the tip of the tongue. Due to the comparability of hand and tongue, the innervation densities of the hand act as an indication for the tongue. The innervation density of the RA units is twice as high as that of the SA units. Analogous to their occurrence, the RA mechanoreceptors play the predominant role. Figure 2.9 presents the relative size and distribution of the 22 mechanoreceptive units identified on the tip of the tongue.

2.3.5 Histological Classification of the End Organs

The end organs of the different kinds of mechanoreceptors are identified histologically in glabrous and hairy skin. Here, the SA-I receptor is represented by the Merkel cells, the

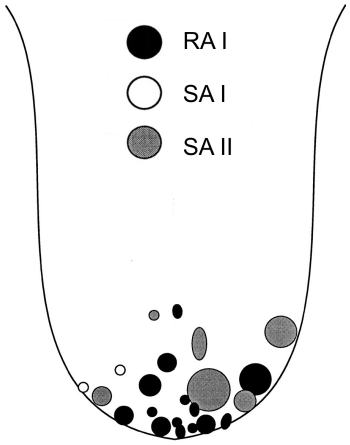

Figure 2.9: The relative size and location of the 22 identified receptive fields belonging to superficial units on the dorsum of the human tongue (Trulsson & Essick, 1997).

SA-II receptor by the Ruffini corpuscles, the RA-I receptor by the Meissner corpuscles, and the RA-II receptor by the Pacinian corpuscles (Schmidt et al., 2005). These end organs cannot be found in the human tongue. Instead, free nerve endings, semiorganized coiled endings and organized endings are identified histologically. However, none of these three end organs could be associated to the different kinds of receptive fields (Trulsson & Essick, 1997).

2.3.6 Sensitivity

There is scarce information about the sensitivity of humans, especially in the mouth region. Sensitivity can be divided into the threshold of detection and the ability to discriminate above the threshold level (Peleg, 1993). Medical literature provides little information concerning the first type of sensitivity in the oral cavity and nothing is known about the second type.

According to Jacobs et al. (2002), light touch sensation is commonly measured by Semmes-Weinstein monofilaments. Von-Frey hairs and esthesiometer are synonyms for this method. The monofilaments consist of nylon and vary in their stiffness, diameter, length and mass. They are applied vertically on the tissue until the point of bending. The stimulus

is retained for 1 s. The monofilaments are applied in ascending order of intensity until the subject perceives the stimulus. Special mini kits enable their application to the oral cavity.

Zur, Genden & Urken (2004) developed a topographic sensory map of the oral cavity. They measured pressure thresholds of the central part of the tongue, the lateral part of the tongue, the lower lip and the buccal mucosa. For this, they used the established Semmes-Weinstein method and compared their results with those measured by means of a novel computerized pressure specified sensory device. The advantage of the latter method is its easier application in the oral cavity and its continuous measurement.

Figure 2.10 shows the averaged threshold values for pressure recognition for both measuring methods. According to these measurements it can be stated that the pressure threshold varies around 2 kPa. It is clear from the figure that the pressure specified sensory device records lower values. Trulsson & Essick (1997) measured the lowest value of 120 Pa for SA-I mechanoreceptors at the tip of the tongue by means of Semmes-Weinstein monofilaments.

Boliek, Rieger, Li, Mohamed, Kickham & Amundsen (2007) report on a better detection of cotton wisps compared with Semmes-Weinstein monofilaments. However, the pressure of the cotton wisps was not standardized and the contact area with the tongue was greater, indicating the stimulation of more sensory afferents.

Komiyama & de Laat (2005) also use the Semmes-Weinstein monofilaments for investigations at the tip of the tongue of males and females. They do not find any differences between the genders. The same group investigated ethnic differences exemplified by Belgium and Japanese subjects (Komiyama, Kawara & de Laat, 2007), with no significant differences found either.

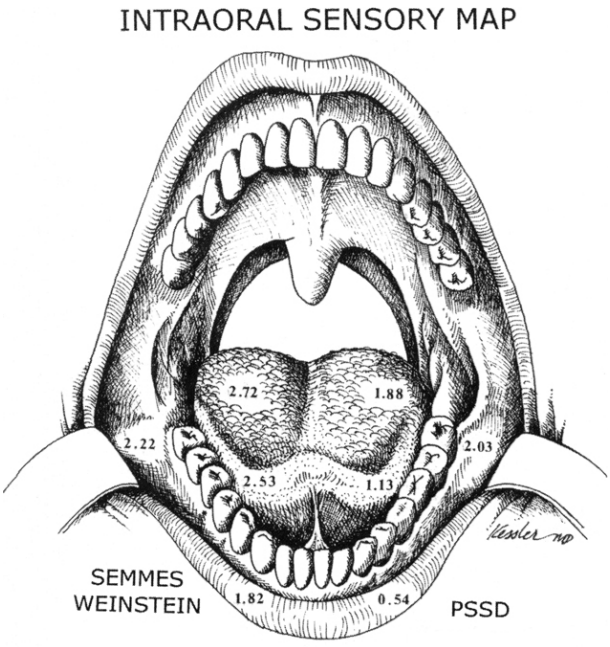

Figure 2.10: The intraoral sensory map representing pressure thresholds for central tongue, lateral tongue, lower lip and buccal mucosa in kPa resulting from measurements by means of Semmes-Weinstein monofilaments on the left-hand side and a pressure specified sensory device (PSSD) on the right-hand side (Zur et al., 2004).

Chapter 3

Analytical Models and Numerical Methods

In this chapter, the analytical and numerical approaches used to model the squeezing flow in the oral cavity are presented. These approaches are based on the geometries of dentist replicas of the oral cavity, from which the averaged dimensions being used for the model geometries are devised.

The basic equations of Newtonian and non-Newtonian fluid flow are outlined. Using these basic equations, the concept of the theory of lubrication is introduced. By means of this theory, flows are described that feature a geometry in which one dimension is significantly smaller than the others. This is important for modeling the squeezing flow in the oral cavity, as the thickness of the fluid film between the tongue and palate is significantly smaller than the oral cavity itself.

The starting point of the analytical investigation of squeezing flows in the oral cavity is the well-known model of Stefan, consisting of two plane circular parallel plates, that is derived from the theory of lubrication. Beginning from this, three other models that have not previously been used to model squeezing flow in the oral cavity are introduced. The derivation of the elliptic plane parallel plate model includes for the first time (as far as is known) the velocities and shear rates and stresses of the flow field. Similarly, new

quantities are derived for a plane and curved circular parallel plate model. A completely new squeezing-flow model, a sphere in a hemisphere, has been deduced on the basis of the REYNOLDS equation in spherical coordinates. These four squeezing-flow models allow for the first time the analytical investigation of the effects of different three-dimensional geometries on the flow behavior in the oral cavity. The last model is of particular importance as it mimics the real oral-cavity geometry the best.

The final part of the chapter gives details of the numerical simulations. The method and the software employed are explained and the geometrical model used for the simulations is introduced.

3.1 Geometrical Model of the Oral Cavity

The geometry of the oral cavity varies from individual to individual. Moreover, the tongue can assume different shapes and is not static during eating and drinking (STANLEY & TAYLOR, 1993). Deglutition starts with pushing the tongue against the front teeth. Afterwards, it is elevated against the palate in a wavelike backward movement. This movement ensures the squeezing out of the bolus from the oral cavity (NICOSIA, 2007).

For the current numerical study it is necessary to assume static states of both the palate and tongue. The simplified model of the oral cavity consists of two ellipsoids without any surface structure (figure 3.1). The geometry of the ellipsoids is based on dentist replicas of the palate. These replicas were taken from four adults; two males and two females.

The maximum dimensions along the different axes of each of the replicas were measured; table 3.1 gives an overview. The averaged values for height, width and length of the measured palates are 16 mm, 36 mm and 58 mm, respectively. For the numerical simulations, the ellipsoidal model of the computational domain was constructed using ANSYS ICEM CFD (ANSYS, 2008). This software allows the construction and the mesh generation of the ellipsoids based on the given key data.

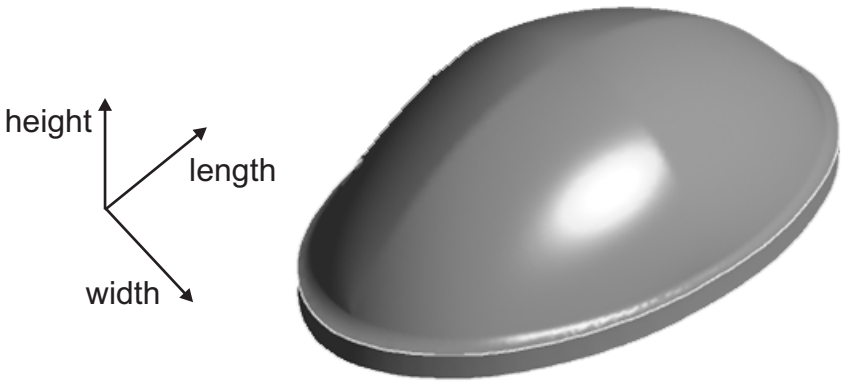

Figure 3.1: The simplified three-dimensional model of the oral cavity consisting of two ellipsoids.

Table 3.1: The maximum dimensions of the dentist replicas of the palates in mm.

	Height	**Width**	**Length**
Male			
Subject 1	13	30	61
Subject 2	20	30	48
Female			
Subject 3	15	42	66
Subject 4	15	41	59
Averaged	16	36	58

The analytical calculations of squeezing flows by means of the theory of lubrication are also based on the key points given in table 3.1. However, the analytical models exhibit even more simplified geometries and therefore do not allow an exact replication of the results obtained by the numerical simulations employing the geometry shown in figure 3.1. Nevertheless, the approximations are reasonable as they consider the main influencing variables of the squeezing flow and allow a quick estimation of the fluid-mechanical quantities. Thus, a decision for the key points in the geometry to consider is necessary. Here, two different concepts are used.

The first concept deals with the dimensions of the tongue-palate model system, which can be measured in the projection screen in the transverse plane (figure 3.2). This results in the radius or rather semi-minor axis $R_{\mathrm{p1}} = 18$ mm for the width and the radius or semi-major axis $R_{\mathrm{p2}} = 29$ mm for its length.

The second concept takes into consideration that the fluid streams in an arc. Hence, circles are constructed through the key points of both the frontal and the sagittal planes. Their radii are approximately $R_1 = 18$ mm and $R_2 = 34$ mm, respectively. The lengths of the arcs between the key points of the two circles are calculated. This approach results in the radius or semi-major axis $R_{\mathrm{a2}} = 35$ mm for the sagittal plane and $R_{\mathrm{a1}} = 26$ mm for the frontal plane (for further details see appendix B). In order to get a better overview, table 3.2 compares the dimensions of the radii and axes.

Table 3.2: The dimensions of the radii and axes employed in the analytical models.

	Frontal	**Sagittal**
Projection	$R_{\mathrm{p1}} = 18$ mm	$R_{\mathrm{p2}} = 29$ mm
Arc	$R_{\mathrm{a1}} = 26$ mm	$R_{\mathrm{a2}} = 35$ mm

3.2 Basic Equations of Fluid Flow

The basic equations of fluid flow have been known since the beginning of the 19$^{\mathrm{th}}$ century (Durst, 2006). The conservation of mass for an incompressible fluid is represented by the equation of continuity

$$\frac{\partial u_i}{\partial x_i} = 0, \tag{3.1}$$

where u_i represents the velocity vector, x_i the position vector and Cartesian tensor index notation is used. The conservation of momentum equation in Cartesian tensor index notation,

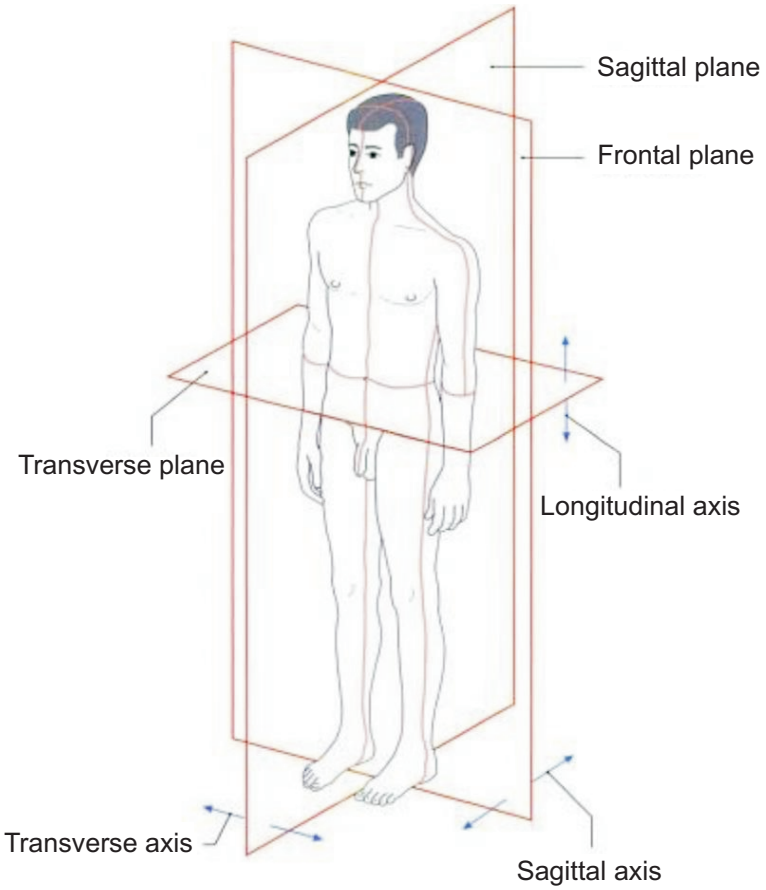

Figure 3.2: The cardinal planes and axes in the human body (SCHUENKE ET AL., 2006).

$$\rho\left(\frac{\partial u_j}{\partial t}+u_i\frac{\partial u_j}{\partial x_i}\right)=-\frac{\partial p}{\partial x_j}-\frac{\partial \tau_{ij}}{\partial x_i}+\rho g_j, \tag{3.2}$$

describes the forces affecting the fluid, namely inertia, pressure, friction and gravity. Here, ρ stands for density, t for time, p for pressure, τ_{ij} for the viscous stress tensor and g_j for the body acceleration, which includes acceleration due to gravity. These two basic equations are valid for nonpolar, isothermal and inert fluids.

The viscous stress tensor τ_{ij} governs the behavior of the fluid. In the incompressible Newtonian case, it takes the form $-\eta\left(\frac{\partial u_j}{\partial x_i}+\frac{\partial u_i}{\partial x_j}\right)$ yielding the equation

$$\rho\left(\frac{\partial u_j}{\partial t}+u_i\frac{\partial u_j}{\partial x_i}\right)=-\frac{\partial p}{\partial x_j}+\eta\frac{\partial^2 u_j}{\partial x_i^2}+\rho g_j, \tag{3.3}$$

which is called the NAVIER-STOKES equation. From the non-Newtonian point of view, several material laws representing distinct characteristics of fluid flow can be modeled using different forms of τ_{ij}. The decision of which one is to be used is based on the experimental data and on which model fits best.

Yogurt was chosen to be the example food for the current study. It features a complex internal microstructure consisting of a gel structure of milk proteins and fat molecules. This structure is irreversibly damaged by increasing temperature and applying shear. Additionally, the rheological behavior of yogurt is time dependent. Many different models have been employed to describe its response to shear and stress (MULLINEUX & SIMMONS, 2008).

The three most common models that are used to describe the rheology of food in general are the power law with an occurence of 47%, the Herschel-Bulkley model (20%) and, with a frequency of 15%, the Casson model (HOLDSWORTH, 1993). One drawback of these models is that they are not suitable over a wide ranges of shear rates as they all give large values for the viscosity η at low shear rates. Although not commonly used, the CROSS model eliminates this disadvantage and can successfully be applied over a wide range of shear rates (CROSS, 1965, GERAGHTY & BUTLER, 1999, MULLINEUX & SIMMONS, 2008).

The appropriateness of the CROSS model for stirred commercial yogurt has been reported by KRULIS & ROHM (2004). Their measurements were carried out by using a four-bladed vane tool and a stress-controlled rheometer. Figure 3.3 shows the very low shear stresses that occur at very low shear rates. The authors successfully applied the CROSS model to these measurements. This observation substantiates the assumption of BARNES & WALTERS (1985) that materials only appear to exhibit yield stress because it is so difficult to measure flows with low shear rates. For this reason, the CROSS law is employed in the non-Newtonian numerical simulation of the current study.

The CROSS model was developed on the basis of molecular considerations. The model follows the assumption that the average group size of flocculated interlinked particles is dependent on the magnitude of the applied shear. The higher the shear rate, the lower the rate of linkage becomes resulting in a limiting viscosity η_∞ at the point of no linkage. The

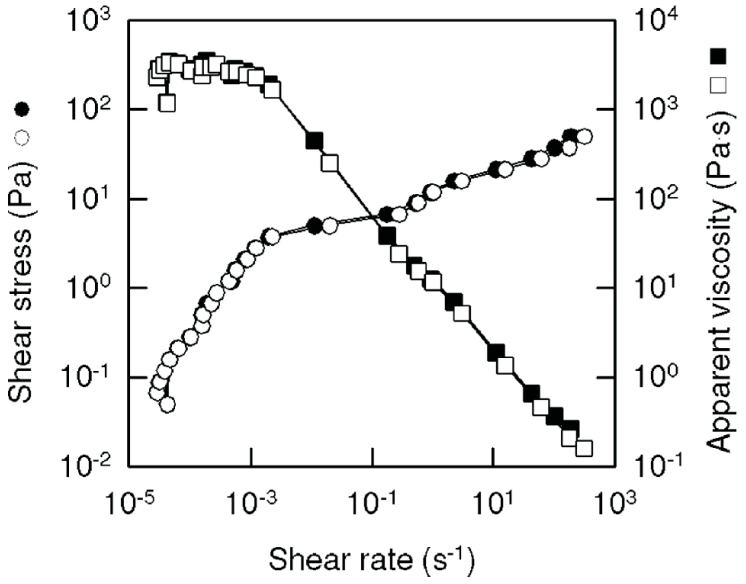

Figure 3.3: The flow curves and viscosity curves for plain yogurt (open symbols) and yogurt with dried cranberries (closed symbols), as measured with a vane tool (Krulis & Rohm, 2004).

highest viscosity η_0 can be assigned to the zero rate of shear.

With this background, Cross develops the equation

$$\eta = \frac{\eta_0 - \eta_\infty}{1 + \alpha D^{2/3}} + \eta_\infty \tag{3.4}$$

where D stands for the shear rate and α is a constant associated with the rupture of linkages. The slightly adapted form

$$\nu = \frac{\nu_0 - \nu_\infty}{1 + (m\dot{\gamma})^n} + \nu_\infty \tag{3.5}$$

is implemented in the module `CrossPowerLaw` of the open-source software OpenFOAM, which is employed in the current study for the numerical simulations of fluid flow (OpenCFD Ltd., 2008). In this representation, m is an arbitrary consistency factor and n the flow behavior index. The advantage of employing this model in numerical codes lies in the fact that no division by zero can occur, which would cause problems.

3.3 Theory of Lubrication

The theory of lubrication is based on Reynolds' classic paper from 1886. It deals with the behavior of thin Newtonian fluid films between two movable close surfaces. In various technical applications, this approach helps to prevent damage occurring to surfaces due to their sliding against each other (Cameron, 1966). On the occasion of the centennial of Reynolds's paper, Pinkus (1987) published an overview of the historical developments in the theory of lubrication.

Due to the technical relevance of non-Newtonian fluid flow behavior the theory has been expanded over the years. There have been several attempts to derive generalized Reynolds equations for any kind of fluid-flow behavior, see for example Bourgin, Francois & Gay (1985), Najji, Bousaid & Berthe (1989), Peiran & Shizhu (1990), Wolff & Kubo (1996). In contrast to the approaches for Newtonian fluids derived by Reynolds, these equations can no longer be solved analytically.

In bioengineering, the theory of lubrication obtained importance in respect of squeezing films. Numerous research papers deal with the lubrication phenomena in human or animal joints, for example Unsworth, Dowson & Wright (1975). Only recently, Tanaka, Detamore, Tanimoto & Kawai (2008) published a review article concerning the lubrication of the temporomandibular joint. These investigations make it possible to reconstruct joints or implant artificial joints after accidents.

In the context of the present thesis, the theory of lubrication is used in another aspect of bioengineering. Four different geometrical models that mimic the squeezing flow in the oral cavity in a greatly simplified way are derived. The simplest geometrical model consisting of two plane circular parallel plates is well accepted in literature as a tongue-palate model. The further models are used for the first time to model squeezing flow in the oral cavity and are meant to discover the influence of different geometries, which are closer to the real geometry in the human mouth. Therefore, the basic Reynolds equations for Newtonian fluid flow behavior adapted to different coordinate systems are reduced according to the consideration of a pure squeezing flow. These equations facilitate the calculation of the distributions of

different physical quantities in different geometrical configurations.

The theory of lubrication is based on some major assumptions (Cameron, 1966, Meyer, 2003). These are

- Newtonian fluid
- neglect of fluid inertia and body forces
- constant viscosity and pressure throughout the fluid film
- negligible velocity gradients apart from those in the cross-film direction
- no slip at the boundaries and
- laminar flow.

3.3.1 Reynolds Equation

Reynolds (1886) developed his equation on the basis of a streamed control cuboid in a Cartesian coordinate system (figure 3.4). The thin Newtonian fluid film of height h is located between two movable surfaces in the xy-plane. Their motion with velocities w_0 and w_h in z-direction is followed by volume changes of the control cuboid. Additionally, these surfaces are movable in parallel to the xy-plane with velocities u_0 and u_h in x-direction and with velocities v_0 and v_h in y-direction. These movements are not followed by volume changes of the control cuboid. For clarity, these velocities are not plotted in figure 3.4.

The fluid flow with the velocities u and v takes place in the yz- and the xz-planes, respectively. The fluid exits through the same planes displaced by dx and dy with velocities differing by $\frac{du}{dx}dx$ and $\frac{dv}{dy}dy$.

Fluid Flow Velocities u and v

When dealing with lubrication, it is assumed that fluid inertia can be neglected, as the inertia force is small compared to the viscous force, and also that body forces can be neglected. As a

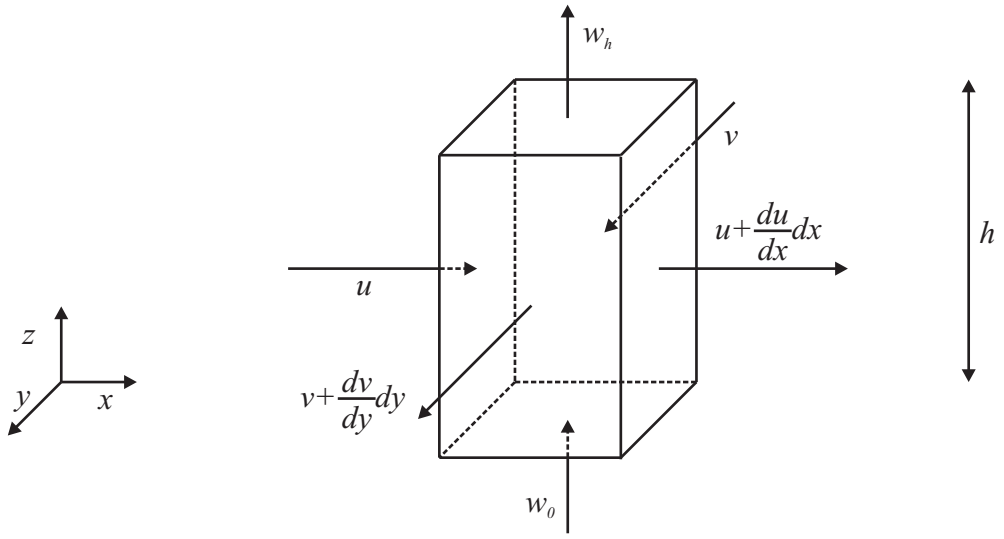

Figure 3.4: The continuity of fluid flow in a streamed control cuboid representing an element of the thin fluid film of the height h between two movable surfaces in the xy-plane.

result, only the second and third terms of the NAVIER-STOKES equation (3.3) remain. This simplified equation allows the flow velocities u and v to be determined. As the derivation for each direction takes place in an analogous manner, it is shown for the x-component only. The final simplified equation

$$\frac{dp}{dx} = \eta \frac{d^2u}{dz^2} \tag{3.6}$$

needs to be integrated twice with respect to z. The resulting equation

$$u = \frac{1}{2\eta}\frac{dp}{dx}z^2 + C_1 z + C_2 \tag{3.7}$$

contains the two constants of integration C_1 and C_2. These constants are determined by employing boundary conditions. Remembering that the lower and upper surface of the cuboid are movable in the x-direction, the boundary conditions are $u(z = 0) = u_0$ and $u(z = h) = u_h$. Therefore, constant C_2 is u_0 and constant C_1 is equal to $\frac{u_h - u_0}{h} - \frac{1}{2\mu}\frac{dp}{dx}h$. Hence, the velocity u is described by the equation

$$u = \frac{1}{2\eta}\frac{dp}{dx}(z^2 - hz) + \frac{u_h - u_0}{h}z + u_0. \tag{3.8}$$

The equation for the velocity v,

$$v = \frac{1}{2\eta}\frac{dp}{dy}(z^2 - hz) + \frac{v_h - v_0}{h}z + v_0, \tag{3.9}$$

arises from an analogous derivation.

Volume Flows

The velocity of fluid flow changes with dependence on the variable z. However, it is constant along the width of the control cuboid. Thus, the volume flow $\dot{V}_x$ is obtained by

$$\dot{V}_x = \int_0^h u dz dy, \tag{3.10}$$

where dy stands for the width of the control cuboid perpendicular to the flow direction x. Considering equation (3.8) gives

$$\dot{V}_x = \left(\frac{1}{2\eta}\frac{dp}{dx}\left[\frac{1}{3}z^3 - \frac{1}{2}hz^2\right]_0^h + \frac{u_h - u_0}{h}\left[\frac{1}{2}z^2\right]_0^h + u_0\left[z\right]_0^h \right) dy \tag{3.11}$$

and with further analysis

$$\dot{V}_x = \left(\frac{1}{2}(u_h + u_0)h - \frac{1}{12\eta}\frac{dp}{dx}h^3 \right) dy \tag{3.12}$$

for the volume flow $\dot{V}_x$ in the x-direction. The analogous derivation yields

$$\dot{V}_y = \left(\frac{1}{2}(v_h + v_0)h - \frac{1}{12\eta}\frac{dp}{dy}h^3 \right) dx \tag{3.13}$$

for the volume flow $\dot{V}_y$ in the y-direction.

Equation of Continuity

For the streamed volume element, without sources and sinks, considered here, the equation of continuity must be valid. Assuming a fluid of constant density ρ, the rate of volume flow must be constant. This brings

$$\dot{V}_x + \dot{V}_y + w_0 dxdy = \left(\dot{V}_x + \frac{d\dot{V}_x}{dx}dx\right) + \left(\dot{V}_y + \frac{d\dot{V}_y}{dy}dy\right) + w_h dxdy \tag{3.14}$$

by employing the velocities w_0 and w_h for the velocities of the upper and lower surfaces in the z-direction. Equivalent transformation gives

$$\frac{d\dot{V}_x}{dxdy} + \frac{d\dot{V}_y}{dxdy} + (w_h - w_0) = 0, \tag{3.15}$$

taking into account a division by the area $dxdy$.

Reynolds Equation

The equation

$$\frac{d}{dx}\left(\frac{1}{2}(u_h + u_0)h - \frac{1}{12\eta}\frac{dp}{dx}h^3\right) + \frac{d}{dy}\left(\frac{1}{2}(v_h + v_0)h - \frac{1}{12\eta}\frac{dp}{dy}h^3\right) + (w_h - w_0) = 0 \tag{3.16}$$

arises from substituting the volume flows $\dot{V}_x$ and $\dot{V}_y$ in equation (3.15) by the relationships deduced in equations 3.12 and 3.13. Factorizing gives

$$\frac{d}{dx}\left(h^3\frac{dp}{dx}\right) + \frac{d}{dy}\left(h^3\frac{dp}{dy}\right) = 6\eta\left(\frac{d}{dx}((u_h + u_0)h) + \frac{d}{dy}((v_h + v_0)h) + 2(w_h - w_0)\right), \tag{3.17}$$

which is named the Reynolds equation. As only one plate is moved in most cases, the variable names of the velocities in the x- and y-direction, which are not zero, are replaced by u and v. Thus, the simplified Reynolds equation,

$$\frac{d}{dx}\left(h^3\frac{dp}{dx}\right) + \frac{d}{dy}\left(h^3\frac{dp}{dy}\right) = 6\eta\left(\frac{d}{dx}(uh) + \frac{d}{dy}(vh) + 2(w_h - w_0)\right), \tag{3.18}$$

is the starting point for analyzing the fluid flow in lubricating films.

Reynolds Equation in Cylindrical Coordinates

The Reynolds equation in cylindrical coordinates can be developed from the Reynolds equation (3.18) in Cartesian coordinates. The relations

$$x = r\cos\varphi,\ y = r\sin\varphi \ \text{ and } \ r^2 = x^2 + y^2 \tag{3.19}$$

are used for this transformation. This gives

$$\begin{aligned}&\frac{1}{r}\frac{d}{dr}\left(rh^3\frac{dp}{dr}\right) + \frac{1}{r^2}\frac{d}{d\varphi}\left(h^3\frac{dp}{d\varphi}\right) = \\ &6\eta\left((u\cos\varphi + v\sin\varphi)\frac{dh}{dr} + (-u\sin\varphi + v\cos\varphi)\frac{1}{r}\frac{dh}{d\varphi} + \frac{d}{d\varphi}(h\omega) + 2(w_h - w_0)\right),\end{aligned} \tag{3.20}$$

where ω is the angular velocity of the surface in the xy-plane (Cameron, 1966).

Reynolds Equation in Spherical Coordinates

Meyer (2003) derived the Reynolds equation in spherical coordinates. For this purpose, a sphere of radius R_i lies in a hemispherical shell of the radius R and can be tilted by the angle ψ with respect to the xy-plane. She obtained the equation

$$\begin{aligned}&\frac{1}{\sin\theta}\frac{d}{d\theta}\left(h^3\sin\theta\frac{dp}{d\theta}\right) + \frac{1}{\sin^2\theta}\frac{d}{d\phi}\left(h^3\frac{dp}{d\phi}\right) = \\ &6R^2\eta\left(\omega\cos\psi\sin\phi\frac{dh}{d\theta} + \left(\omega\sin\psi + \omega\cos\psi\frac{\cos\theta}{\sin\theta}\cos\phi\right)\frac{dh}{d\phi} + 2\frac{dh}{dt}\right),\end{aligned} \tag{3.21}$$

where θ is the zenith angle from the positive z-axis, ϕ is the azimuth angle from the positive x-axis in the xy-plane and ω is the angular velocity vector of the inner sphere. As there is no need for an inclination angle ψ in the present study, the equation

$$h = c - e_x\cos\phi\sin\theta - e_y\sin\theta\sin\phi - e_z\cos\theta \tag{3.22}$$

derived by GOENKA & BOOKER (1980) is adequate for the expression of the film thickness h. Here, c stands for the radial clearance $R - R_i$, while e_x, e_y and e_z are the eccentricities in the different coordinate directions.

3.3.2 Squeezing Flow

Pure squeezing flows are characterized by exclusive motions of the surfaces in the z-direction. There are neither relative motions in the x- and y-direction, nor rotational motions with the angles φ, ϕ and θ. Simplifying the REYNOLDS equation (3.18) in Cartesian coordinates according to these requirements gives

$$\frac{d}{dx}\left(h^3\frac{dp}{dx}\right) + \frac{d}{dy}\left(h^3\frac{dp}{dy}\right) = 12\eta(w_h - w_0) \tag{3.23}$$

for the description of a squeezing flow between two surfaces.

In the following derivations the lower surface is assumed to be fixed. In contrast, the upper surface moves down with a uniform velocity. That means that the film thickness h diminishes with the time t. The equation

$$\frac{d}{dx}\left(h^3\frac{dp}{dx}\right) + \frac{d}{dy}\left(h^3\frac{dp}{dy}\right) = -12\eta\frac{dh}{dt} \tag{3.24}$$

depicts the resulting squeezing flow.

Analogously, the equations for the squeezing flow are

$$\frac{1}{r}\frac{d}{dr}\left(rh^3\frac{dp}{dr}\right) = -12\eta\frac{dh}{dt} \tag{3.25}$$

in cylindrical coordinates and

$$\frac{d}{d\theta}\left(h^3\sin\theta\frac{dp}{d\theta}\right) = 12R^2\eta\frac{dh}{dt}\sin\theta \tag{3.26}$$

in spherical ones. The change in the algebraic sign arises from the fact that in the present

consideration the sphere is the movable component shifting against the upper hemisphere.

Applying these equations, the geometrical arrangements of both surfaces and the fluid film between the two surfaces are variable in their shape. The oldest paper from STEFAN (1874) deals with a fluid film thickness h, which is constant along the radial coordinate r of the circular plane plates. This approach is often used as a reference in food science, as has been shown in the analytical approaches of section 2.2.4.

REYNOLDS (1886) derived a solution for the pressure distribution between two plane elliptic plates. This approach is introduced here, as the projection plane of the numerical model is elliptic.

Later attempts also investigated the fluid flow behavior due to a varying film thickness h along the radius r of circular plates. In order to mimic the increasing fluid-film thickness, which can be found in the numerical model, a double exponential function is employed. This approach was first published by MURTI in 1975.

Based on the previously introduced REYNOLDS equation in spherical coordinates it is possible to derive equations describing the fluid flow along θ between a sphere and a hemisphere. This approach reflects the three-dimensional nature of the human oral cavity simulated in the numerical calculations.

All of the approaches introduced above belong to the few exceptions that are solvable analytically. There are some cases in which a semi-analytical solution is appropriate. One example is the squeezing flow in a journal bearing (KHONSARI & BOOSER, 2001). Here, a function for the fluid-film thickness h can be obtained. However, substituting the fluid-film thickness h in the REYNOLDS equation by this function requires further numerical treatment of the equation.

3.3.3 Plane Circular Parallel Plates - STEFAN Equation

Figure 3.5 shows the geometrical arrangement of the two plane circular parallel plates employed by STEFAN (1874). As the fluid film thickness h is constant along the radius r, it is

renamed h_0. Introducing this in the squeezing-flow equation (3.25) in cylindrical coordinates, multiplying by r and integrating once leads to

$$rh_0^3\frac{dp}{dr} = -12\eta v_\mathrm{p}\frac{r^2}{2} + C_1, \tag{3.27}$$

where the uniform plate velocity v_p substitutes the term $\frac{dh_0}{dt}$ for reasons of convenience.

According to the boundary condition $\frac{dp}{dr} = 0$ at $r = 0$, the constant of integration C_1 becomes zero. The resulting equation is

$$\frac{dp}{dr} = -\frac{6\eta v_\mathrm{p}}{h_0^3}r \tag{3.28}$$

after dividing through by rh_0^3. Integrating again gives

$$p = -\frac{6\eta v_\mathrm{p}}{h_0^3}\frac{r^2}{2} + C_2 \tag{3.29}$$

and considering the boundary condition $p = p_0$ at $r = R$

$$p - p_0 = 3\frac{\eta v_\mathrm{p}}{h_0^3}(R^2 - r^2), \tag{3.30}$$

which is called the STEFAN equation.

According to this equation, the pressure will go to infinity as the film thickness goes to zero. This would mean that we could never achieve the force required to press our tongue against our palate. As this is possible in reality, tiny film thicknesses need to be compensated

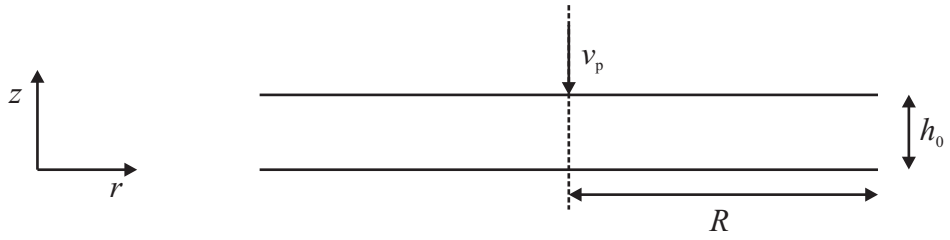

Figure 3.5: The squeezing flow between two plane parallel plates whereby the upper plate is moved down with the uniform plate velocity v_p.

by moving the tongue with smaller velocities the closer it comes to the palate. Hence, the tongue velocity cannot be kept constant during the whole process of deglutition.

Knowing the pressure profile it is possible to derive the corresponding velocity distribution. As the squeezing flow is axisymmetric, the equations are derived in cylindrical coordinates yielding velocity components in the z- and r-directions.

Starting from the equation of continuity,

$$\frac{1}{r}\frac{\partial}{\partial r}\left(ru_r\right) + \frac{1}{r}\frac{\partial u_\varphi}{\partial \varphi} + \frac{\partial u_z}{\partial z} = 0, \tag{3.31}$$

the expression for u_r can be derived first (Middleman, 1998, Engmann, Servais & Burbidge, 2005). This equation reduces to

$$\frac{1}{r}\frac{\partial}{\partial r}\left(ru_r\right) + \frac{\partial u_z}{\partial z} = 0 \tag{3.32}$$

as the fluid flow is axisymmetric. At the surface of the plates, there can only be a velocity component u_z in the z-direction due to the no-slip condition. This assumption is valid along the radial coordinate r. For that reason, the equation can be rearranged to

$$\frac{1}{r}\frac{\partial}{\partial r}\left(ru_r\right) = -\frac{\partial u_z}{\partial z} = f(z,t), \tag{3.33}$$

where the partial differentiation $\frac{\partial u_z}{\partial z}$ is only a function f of the direction z and the time t. In the next step, this result is substituted in the conservation of momentum equation. This equation reads

$$\frac{\partial p}{\partial r} = \eta\left(\frac{\partial}{\partial r}\left(\frac{1}{r}\frac{\partial}{\partial r}\left(ru_r\right)\right) + \frac{1}{r^2}\frac{\partial^2 u_r}{\partial \varphi^2} - \frac{2}{r^2}\frac{\partial u_\varphi}{\partial \varphi} + \frac{\partial^2 u_r}{\partial z^2}\right) \tag{3.34}$$

in the r-direction considering only the dominant terms in lubrication theory, representing pressure and friction, and can be reduced to

$$\frac{\partial p}{\partial r} = \eta\left(\frac{\partial}{\partial r}\left(\frac{1}{r}\frac{\partial}{\partial r}\left(ru_r\right)\right) + \frac{\partial^2 u_r}{\partial z^2}\right) \tag{3.35}$$

as a result of the axisymmetry. Inserting equation (3.33) yields

$$\frac{\partial p}{\partial r} = \eta \left(\frac{\partial}{\partial r} \left(f(z,t) \right) + \frac{\partial^2 u_r}{\partial z^2} \right) \tag{3.36}$$

and

$$\frac{\partial p}{\partial r} = \eta \frac{\partial^2 u_r}{\partial z^2} \tag{3.37}$$

respectively, as the function $f(z,t)$ is independent of the r-direction. Integrating twice with respect to z results in

$$u_r = \frac{1}{2\eta} \frac{\partial p}{\partial r} z^2 + C_1 z + C_2 \tag{3.38}$$

for the velocity component u_r. Taking the no-slip condition into consideration, the boundary conditions are $u_r(0) = 0$ and $u_r(h_0) = 0$. From these values, the integration constants C_1 and C_2 can be determined with the results being

$$C_2 = 0 \tag{3.39}$$

and

$$C_1 = -\frac{1}{2\eta} \frac{\partial p}{\partial r} h_0. \tag{3.40}$$

These values lead to the equation

$$u_r = \frac{1}{2\eta} \frac{\partial p}{\partial r} h_0 z \left(\frac{z}{h_0} - 1 \right) \tag{3.41}$$

and after inserting equation (3.30) to

$$u_r = 3 \frac{v_\mathrm{p}}{h_0^2} r z \left(1 - \frac{z}{h_0} \right) \tag{3.42}$$

for the velocity component u_r.

The second velocity component u_z can be derived by means of the continuity equation

in cylindrical coordinates (3.32). The result is

$$\frac{1}{r}\frac{\partial}{\partial r}\left(3\frac{v_\mathrm{p}}{h_0^2}r^2 z\left(1-\frac{z}{h_0}\right)\right)+\frac{\partial u_z}{\partial z}=0 \tag{3.43}$$

substituting the relationship for the velocity component u_r. This equation is simplified and rearranged yielding

$$\frac{\partial u_z}{\partial z}=6\frac{v_\mathrm{p}}{h_0^3}z^2-6\frac{v_\mathrm{p}}{h_0^2}z \tag{3.44}$$

and integrating with respect to z

$$u_z=3\frac{v_\mathrm{p}}{h_0^2}z^2\left(\frac{2}{3}\frac{z}{h_0}-1\right)+C_1 \tag{3.45}$$

for the velocity component u_z. The boundary condition is $u_z(0)=0$. This condition yields the result

$$C_1=0 \tag{3.46}$$

for the integration constant C_1. Therefore, the final equation is

$$u_z=3\frac{v_\mathrm{p}}{h_0^2}z^2\left(\frac{2}{3}\frac{z}{h_0}-1\right) \tag{3.47}$$

for the velocity component in z-direction. In contrast to the pressure distribution, the velocity components are independent from both viscosity η and the geometrical dimension, R, of the plates. Differentiation of the function shows that the maximum and minimum velocity values are found at the surfaces of the plates and that the inflection point is in the middle of the fluid film.

Starting from the equation (3.42) for the velocity component in main fluid-flow direction, u_r, the shear rate can be derived by differentiating with respect to the coordinate z. This yields the equation

$$\frac{du_r}{dz}=3\frac{v_\mathrm{p}}{h_0^2}r\left(1-2\frac{z}{h_0}\right), \tag{3.48}$$

which is only dependent on the constants v_p and h_0. The result is most interesting at the

surfaces of the models as the mechanoreceptors receive the stimuli here. The results are

$$\frac{du_r}{dz} = 3\frac{v_\mathrm{p}}{h_0^2}r \tag{3.49}$$

for $z = 0$ and

$$\frac{du_r}{dz} = -3\frac{v_\mathrm{p}}{h_0^2}r \tag{3.50}$$

for $z = h_0$. This means that the same absolute values of shear rate occur at the different surfaces. The absolute value of the shear stress,

$$\tau_{zr} = 3\frac{\eta v_\mathrm{p}}{h_0^2}r\left(1 - 2\frac{z}{h_0}\right), \tag{3.51}$$

results from the multiplication of the absolute value of the shear rate with the viscosity η.

The external force F that is required to drive the plates together can be obtained by integrating the normal stress τ_{zz} over the radial coordinate of the plates (Middleman, 1998). The result reads

$$F = 2\pi\int_0^R \tau_{zz} r dr \tag{3.52}$$

and can be further simplified assuming a Newtonian fluid. The equation

$$\tau_{zz} = p - 2\eta\frac{\partial u_z}{\partial z} \tag{3.53}$$

shows the components of the normal stress τ_{zz}. The viscous part of the total normal stress τ_{zz} can be neglected as there cannot be a velocity in the z-direction at the resting surface. Hence, the force can be described by the equation

$$F = 2\pi\int_0^R p(r) r dr \tag{3.54}$$

in which $p(r)$ can be replaced by equation (3.30). Therefore, the equation

$$F = \frac{3}{2}\pi\frac{\eta v_\mathrm{p}}{h_0^3}R^4 \tag{3.55}$$

describes the force F that is necessary to drive the plates together.

3.3.4 Plane Elliptic Parallel Plates

The equation

$$\frac{x^2}{a^2} + \frac{y^2}{b^2} = 1 \tag{3.56}$$

describes the shape of an ellipse in Cartesian coordinates (figure 3.6). In order to calculate the pressure distribution between two plane elliptic parallel plates, equation (3.56) is combined with equation (3.24). Unlike the previous derivation of an equation for the pressure distribution, the ansatz function

$$p - p_0 = f_c \left(\frac{x^2}{a^2} + \frac{y^2}{b^2} - 1 \right) \tag{3.57}$$

is postulated here (Reynolds, 1886, Khonsari & Booser, 2001).

The objective is to determine the constant f_c in such a way that the pressure becomes p_0 at the boundaries of the elliptic plates. For this purpose, equation (3.24) adopts the form

$$\frac{d^2(p - p_0)}{dx^2} + \frac{d^2(p - p_0)}{dy^2} = -12 \frac{\eta v_p}{h_0^3} \tag{3.58}$$

considering the constant fluid-film thickness h_0, which is independent from the x- and y-coordinates, and the uniform plate velocity $\frac{dh_0}{dt} = v_p$. Substituting the pressure difference

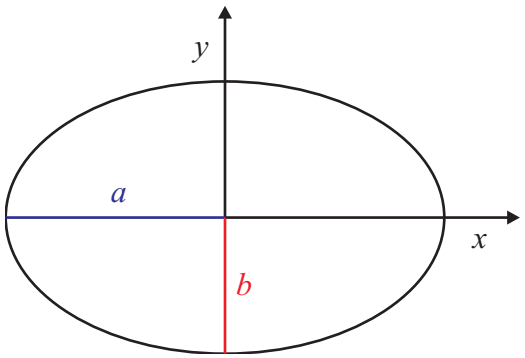

Figure 3.6: The geometry of an ellipse with the semi-major axis a and the semi-minor axis b.

$p - p_0$ by the ansatz function (3.57) yields

$$\frac{d^2\left(\frac{f}{a^2}x^2\right)}{dx^2} + \frac{d^2\left(\frac{f}{b^2}y^2\right)}{dy^2} = -12\frac{\eta v_\mathrm{p}}{h_0^3} \tag{3.59}$$

and equivalent rearrangement

$$f_\mathrm{c} = -6\frac{\eta v_\mathrm{p}}{h_0^3}\frac{a^2b^2}{a^2+b^2} \tag{3.60}$$

for the constant f_c.

Therewith, the equation

$$p - p_0 = -6\frac{\eta v_\mathrm{p}}{h_0^3}\frac{a^2b^2}{a^2+b^2}\left(\frac{x^2}{a^2} + \frac{y^2}{b^2} - 1\right) \tag{3.61}$$

allows the calculation of the pressure distribution between two plane parallel elliptic plates.

In the next step, it is shown that the equation for the pressure distribution between two parallel elliptic plates can be reduced to the one for plane circular parallel plates. This is the case when both axes of the elliptic plates a and b are assumed to be equal to the radius R of a circular plate. Furthermore, the Cartesian coordinates need to be rewritten in cylindrical ones using $x = r\cos\varphi$ and $y = r\sin\varphi$. Inserting these relationships in equation (3.61), the result reads

$$p - p_0 = -6\frac{\eta v_\mathrm{p}}{h_0^3}\frac{R^4}{R^2+R^2}\left(\frac{(r\cos\varphi)^2}{R^2} + \frac{(r\sin\varphi)^2}{R^2} - 1\right). \tag{3.62}$$

When simplified, this yields

$$p - p_0 = -3\frac{\eta v_\mathrm{p}}{h_0^3}R^2\left(\frac{r^2(\cos^2\varphi + \sin^2\varphi) - R^2}{R^2}\right) \tag{3.63}$$

and

$$p - p_0 = 3\frac{\eta v_\mathrm{p}}{h_0^3}\left(R^2 - r^2\right), \tag{3.64}$$

taking into account that $\cos^2\varphi + \sin^2\varphi = 1$. As this equation is the same as the equation for a circular system, this shows that the two models [equations (3.30) and (3.61)] are consistent.

The starting point for the derivation of the equation representing the velocity compo-

nent u_x is equation (3.6). The pressure gradient $\frac{dp}{dx}$ can also be expressed by differentiating equation (3.61) with respect to x. The equation

$$\frac{\partial^2 u_x}{\partial z^2} = -12\frac{v_\mathrm{p}}{h_0^3}\frac{b^2}{a^2+b^2}x \tag{3.65}$$

arises from both relations. Integrating twice with respect to z yields

$$u_x = -6\frac{v_\mathrm{p}}{h_0^3}\frac{b^2}{a^2+b^2}xz^2 + C_1 z + C_2 \tag{3.66}$$

for the velocity component u_x. The boundary conditions of the system are $u_x(0) = 0$ and $u_x(h_0) = 0$ yielding

$$C_2 = 0 \tag{3.67}$$

and

$$C_1 = 6\frac{v_\mathrm{p}}{h_0^3}\frac{b^2}{a^2+b^2}xh_0 \tag{3.68}$$

for the integration constants C_1 and C_2. Inserting these constants leads to the final equation

$$u_x = 6\frac{v_\mathrm{p}}{h_0^2}\frac{b^2}{a^2+b^2}xz\left(1-\frac{z}{h_0}\right) \tag{3.69}$$

for the velocity component u_x. The equation

$$u_y = 6\frac{v_\mathrm{p}}{h_0^2}\frac{a^2}{a^2+b^2}yz\left(1-\frac{z}{h_0}\right) \tag{3.70}$$

for the velocity component u_y can be derived in an analogous manner.

The velocity component u_z can be derived from the equation of continuity in Cartesian coordinates [equation (3.1)]. Inserting the velocity components u_x and u_y yields the equation

$$\frac{\partial u_z}{\partial z} = -6\frac{v_\mathrm{p}}{h_0^2}z\left(1-\frac{z}{h_0}\right), \tag{3.71}$$

which was determined in the previous section. Therefore, the final expression for the velocity component u_z is the same as equation (3.47). This result is not surprising as the equation

is independent of the coordinates of the main fluid-flow direction and only dependent on z. Both geometrical configurations are similar in the z-direction due to the constant height of the gap between the plane plates.

The shear rate can be calculated by differentiating the equations of velocity (3.69) and (3.70) with respect to z. The equations

$$\frac{du_x}{dz} = 6\frac{v_\mathrm{p}}{h_0^2}\frac{b^2}{a^2+b^2}x\left(1-2\frac{z}{h_0}\right) \tag{3.72}$$

and

$$\frac{du_y}{dz} = 6\frac{v_\mathrm{p}}{h_0^2}\frac{a^2}{a^2+b^2}y\left(1-2\frac{z}{h_0}\right) \tag{3.73}$$

show the result. The most interesting shear rates are those at the surfaces of the geometry, where $z = 0$ and $z = h_0$, which are the wall shear stresses. These are

$$\frac{du_x}{dz} = 6\frac{v_\mathrm{p}}{h_0^2}\frac{b^2}{a^2+b^2}x \tag{3.74}$$

and

$$\frac{du_y}{dz} = 6\frac{v_\mathrm{p}}{h_0^2}\frac{a^2}{a^2+b^2}y \tag{3.75}$$

considering only their absolute values. Multiplying those equations with the viscosity η gives the shear stress. The resulting equations read

$$\tau_{zx} = 6\frac{\eta v_\mathrm{p}}{h_0^2}\frac{b^2}{a^2+b^2}x\left(1-2\frac{z}{h_0}\right) \tag{3.76}$$

for the x-component and

$$\tau_{zy} = 6\frac{\eta v_\mathrm{p}}{h_0^2}\frac{a^2}{a^2+b^2}y\left(1-2\frac{z}{h_0}\right) \tag{3.77}$$

for the y-component.

The force F that is necessary to drive the plates together can be calculated by integrating over the ellipse (Lorentz & Schmidt, 1922). The y-values at the outflow for certain x-

values can be derived from the equation of the ellipse (3.56). The equation

$$y = \left| \frac{b}{a} \sqrt{a^2 - x^2} \right| \tag{3.78}$$

shows the absolute values. The outermost values of x are a and $-a$. Therefore, the integral

$$F = -6 \frac{\eta v_\mathrm{p}}{h_0^3} \frac{a^2 b^2}{a^2 + b^2} \int_{-a}^{a} \int_{-\frac{b}{a}\sqrt{a^2-x^2}}^{\frac{b}{a}\sqrt{a^2-x^2}} \left(\frac{x^2}{a^2} + \frac{y^2}{b^2} - 1 \right) dx dy \tag{3.79}$$

leads to the final expression

$$F = 3\pi \frac{\eta v_\mathrm{p}}{h_0^3} \frac{a^3 b^3}{a^2 + b^2}. \tag{3.80}$$

This equation can directly be transformed into equation (3.55) considering $a = b = R$.

3.3.5 Plane and Curved Circular Parallel Plates

Figure 3.7 depicts the geometrical configuration employed by Murti (1975). The fluid film thickness h is expressed by the double exponential function

$$h = h_0 e^{-\beta r^2}, \tag{3.81}$$

which obviously changes along the radius r. The distance h_0 stands for the closest distance between the two plates. The thickness h of the lubrication film increases to h_max at the outer radius R of the circular plates. The variable β stands for the curvature parameter. If β is zero, the upper plate will be planar. In this case, the derivation in section 3.3.3 is valid.

Equation (3.25) adopts the form

$$\frac{1}{r} \frac{d}{dr} \left(r h_0^3 e^{-3\beta r^2} \frac{dp}{dr} \right) = -12\eta \frac{d}{dt} \left(h_0 e^{-\beta r^2} \right) \tag{3.82}$$

after insertion of the function representing the film thickness h. The curvature parameter β and the radial coordinate r are not dependent on the time t. This leaves the derivative $\frac{dh_0}{dt}$ on the right hand side, which is substituted by the uniform plate velocity v_p. Multiplying

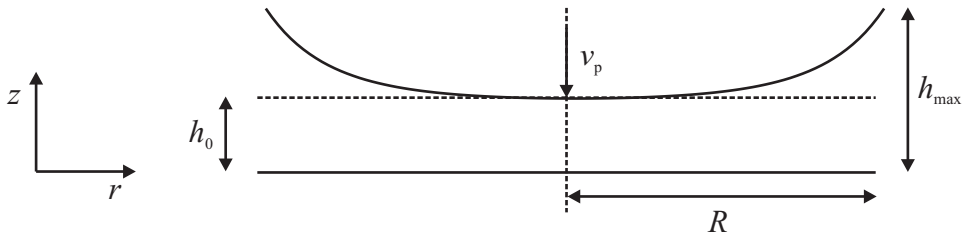

Figure 3.7: The squeezing flow between a plane and a curved plate in parallel whereby the upper plate is moved down with the uniform plate velocity v_p.

by r and integrating once gives

$$rh_0^3 e^{-3\beta r^2} \frac{dp}{dr} = -12\eta v_\mathrm{p} \frac{r^2}{2} + C_1 \tag{3.83}$$

where the constant C_1 becomes zero. Division by $rh_0^3 e^{-3\beta r^2}$ gives

$$\frac{dp}{dr} = -6\frac{\eta v_\mathrm{p}}{h_0^3} e^{3\beta r^2} r \tag{3.84}$$

and integrating with respect to r

$$p = -\frac{\eta v_\mathrm{p}}{h_0^3} \frac{e^{3\beta r^2}}{\beta} + C_2 \tag{3.85}$$

according to Wolfram (2008). The final equation

$$p - p_0 = \frac{1}{\beta} \frac{\eta v_\mathrm{p}}{h_0^3} \left(e^{3\beta R^2} - e^{3\beta r^2} \right) \tag{3.86}$$

is obtained by introducing the boundary condition $\frac{dp}{dr} = 0$ at $r = 0$.

Knowing the pressure distribution along the radial coordinate r, the velocity component u_r in the main fluid-flow direction can be derived. Equation (3.35) shows the conservation of momentum equation in an axisymmetric form. Starting from this equation, the equation

$$\frac{\partial p}{\partial r} = \eta \frac{\partial^2 u_r}{\partial z^2} \tag{3.87}$$

can be deduced from the assumption of lubrication theory that the gradient of the velocity component u_r in the r-direction is negligible. In the next step, the equation representing the pressure distribution (3.86) needs to be obtained. The resulting equation

$$\frac{\partial^2 u_r}{\partial z^2} = -6\frac{v_\mathrm{p}}{h_0^3} r e^{3\beta r^2} \tag{3.88}$$

is integrated twice with respect to z yielding

$$u_r = -3\frac{v_\mathrm{p}}{h_0^3} r e^{3\beta r^2} z^2 + C_1 z + C_2 \tag{3.89}$$

for the velocity component u_r. Due to the no-slip condition the boundary conditions are $u_r(z = 0) = 0$ and $u_r(z = h_0 e^{-\beta r^2}) = 0$. These give values of

$$C_2 = 0 \tag{3.90}$$

and

$$C_1 = 3\frac{v_\mathrm{p}}{h_0^2} r e^{2\beta r^2} \tag{3.91}$$

for the integration constants. Insertion of these values leads to the final equation

$$u_r = 3\frac{v_\mathrm{p}}{h_0^2} r z e^{2\beta r^2} \left(1 - \frac{z}{h_0} e^{\beta r^2}\right) \tag{3.92}$$

for the velocity component u_r in the main fluid-flow direction.

The shear rate

$$\frac{du_r}{dz} = 3\frac{v_\mathrm{p}}{h_0^2} r e^{2\beta r^2} \left(1 - 2\frac{z}{h_0} e^{\beta r^2}\right) \tag{3.93}$$

can be derived by differentiating the velocity u_r with respect to z. The absolute value of the shear rate at the surfaces is

$$\frac{du_r}{dz} = 3\frac{v_\mathrm{p}}{h_0^2} r e^{2\beta r^2} \tag{3.94}$$

taking into account $z = 0$ and $z = h_0 e^{-\beta r^2}$. The shear stress,

$$\tau_{zr} = 3\frac{\eta v_\mathrm{p}}{h_0^2} r e^{2\beta r^2} \left(1 - 2\frac{z}{h_0} e^{\beta r^2}\right), \tag{3.95}$$

is obtained by multiplying the shear rate with the viscosity η.

The force F that is required to move the plates together can be calculated by integration again. The equation reads

$$F = 2\pi \int_0^R r p(r) dr \tag{3.96}$$

and can be transformed into

$$F = \frac{1}{3}\pi \frac{\eta v_\mathrm{p}}{\beta^2 h_0^3} \left(e^{3\beta R^2}(e^{3\beta R^2} - 1) + 1\right) \tag{3.97}$$

taking into account equation (3.86).

3.3.6 Sphere in a Hemisphere

On the basis of the given Reynolds equation (3.21) in spherical coordinates (Meyer, 2003) an equation for a pure squeezing flow between a sphere and a hemisphere can be deduced. This novel equation reflects the situation in the oral cavity best and is solvable analytically with several simplifications. It is assumed that the inner sphere lies centric in the outer hemisphere with regard to the x- and y-direction. Consequently, the resulting fluid flow must be axially symmetric with respect to the z-axis (figure 3.8).

The Reynolds equation in spherical coordinates (3.21) can be simplified, resulting in

$$\frac{d}{d\theta}\left(h^3 \sin\theta \frac{dp}{d\theta}\right) = 12R^2 \eta \frac{dh}{dt} \sin\theta \tag{3.98}$$

considering the above defined restrictions for a pure squeezing flow. The equation (3.22) for the film thickness h reduces to

$$h = c - e_z \cos\theta \tag{3.99}$$

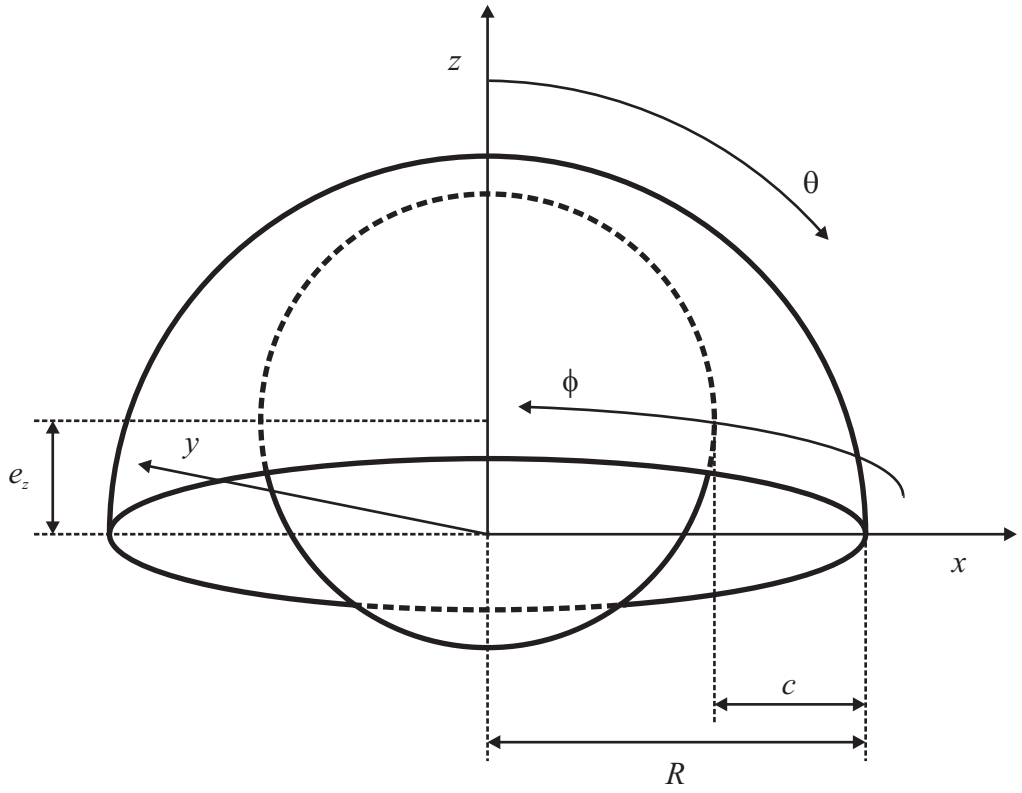

Figure 3.8: A sphere in a hemisphere whereby the geometrical configuration is characterized by an axial symmetry to the z-axis, the radial clearance c and the eccentricity e_z in the z-direction.

due to the rotational symmetry along the z-axis. Strictly speaking, this equation is only valid in the θ-range from 0 to $\arctan\left(\frac{R-c}{e_z}\right)$. If the angle θ is larger, the gradient of the tangent to the inner sphere is positive. This means that the film thickness h increases more than equation 3.99 suggests. The difference is small as long as the clearance c is small. The equation

$$E = \left(1 - \frac{\sqrt{(R-c)^2 - e_z^2}}{R-c}\right) \cdot 100\% \tag{3.100}$$

defines the resulting error E in percent. For reasons of mathematical convenience, equation (3.99) is employed for the further derivations.

Inserting equation (3.99) into equation (3.98) yields

$$\frac{d}{d\theta}\left(h^3 \sin\theta \frac{dp}{d\theta}\right) = -12R^2\eta v_\mathrm{p} \sin\theta\cos\theta, \tag{3.101}$$

taking into account that only the eccentricity e_z depends on the time and that the uniform velocity $\frac{de_z}{dt}$ can be replaced by v_p in analogy to the previous sections.

Integrating this equation results in

$$h^3 \sin\theta \frac{dp}{d\theta} = -6R^2\eta v_\mathrm{p} \sin^2\theta + C_1 \tag{3.102}$$

with $C_1 = 0$ due to the boundary condition $\frac{dp}{d\theta} = 0$ at $\theta = 0$. Dividing through by $h^3 \sin\theta$ and substituting h by equation (3.99) gives the equation

$$\frac{dp}{d\theta} = -\frac{6R^2\eta v_\mathrm{p} \sin\theta}{(c - e_z \cos\theta)^3}, \tag{3.103}$$

which needs to be integrated again (Gradshteyn & Ryzhik, 1980). The result

$$p = \frac{3R^2\eta v_\mathrm{p}}{e_z(c - e_z\cos\theta)^2} + C_2 \tag{3.104}$$

contains the second constant of integration C_2. This constant can be determined to be

$$C_2 = p_0 - \frac{3R^2\eta v_\mathrm{p}}{e_z c^2} \tag{3.105}$$

as the pressure becomes p_0 at the angle $\theta = 90°$. The final equation is

$$p - p_0 = \frac{3R^2\eta v_\mathrm{p}}{e_z}\left(\frac{1}{(c - e_z\cos\theta)^2} - \frac{1}{c^2}\right) = 3R^2\eta v_\mathrm{p}\frac{2c\cos\theta - e_z\cos^2\theta}{c^2\,(c - e_z\cos\theta)^2}, \tag{3.106}$$

with the restrictions that both the radial clearance c and the film thickness h [see equation (3.99)] may be small but not zero.

In the next step, the velocity is derived. The conservation of momentum equation in

spherical coordinates reads

$$\frac{1}{r}\frac{\partial p}{\partial \theta} = \eta\left(\frac{1}{r^2}\frac{\partial}{\partial r}\left(r^2\frac{\partial u_\theta}{\partial r}\right) + \frac{1}{r^2}\frac{\partial}{\partial \theta}\left(\frac{1}{\sin\theta}\frac{\partial}{\partial \theta}\left(u_\theta \sin\theta\right)\right) + \frac{1}{r^2\sin^2\theta}\frac{\partial^2 u_\theta}{\partial \phi^2} + \frac{2}{r^2}\frac{\partial u_r}{\partial \theta} - \frac{2\cos\theta}{r^2\sin^2\theta}\frac{\partial u_\phi}{\partial \phi}\right) \tag{3.107}$$

in its complete form in the θ-direction. This equation reduces to

$$\frac{1}{r}\frac{\partial p}{\partial \theta} = \eta\left(\frac{1}{r^2}\frac{\partial}{\partial r}\left(r^2\frac{\partial u_\theta}{\partial r}\right) + \frac{1}{r^2}\frac{\partial}{\partial \theta}\left(\frac{1}{\sin\theta}\frac{\partial}{\partial \theta}\left(u_\theta \sin\theta\right)\right) + \frac{2}{r^2}\frac{\partial u_r}{\partial \theta}\right) \tag{3.108}$$

due to axisymmetry. The main fluid-flow direction is the θ-direction. Again, the assumption that the velocity gradient in this direction is negligible, is valid. This leads to the greatly simplified equation

$$\frac{\partial p}{\partial \theta} = \eta\frac{1}{r}\frac{\partial}{\partial r}\left(r^2\frac{\partial u_\theta}{\partial r}\right), \tag{3.109}$$

which features a comparable structure to the initial equations in the former sections. The equation

$$\frac{\partial}{\partial r}\left(r^2\frac{\partial u_\theta}{\partial r}\right) = -6v_\mathrm{p}\frac{R^2\sin\theta}{(c - e_z\cos\theta)^3}r \tag{3.110}$$

arises from inserting the pressure distribution given by equation (3.106). The following steps are integration with respect to r, dividing by r^2 and integration with respect to r again. This leads to the equation

$$u_\theta = -3v_\mathrm{p}\frac{R^2\sin\theta}{(c - e_z\cos\theta)^3}r - \frac{C_1}{r} + C_2 \tag{3.111}$$

for the velocity component u_θ in the main fluid-flow direction. The boundary conditions are $u_\theta(r = R) = 0$ and $u_\theta(r = R - c + e_z\cos\theta) = 0$. From these values, the integration constants

$$C_1 = -3v_\mathrm{p}\frac{R^3\sin\theta}{(c - e_z\cos\theta)^3}((c - e_z\cos\theta) - R) \tag{3.112}$$

and

$$C_2 = -3v_\mathrm{p}\frac{R^2\sin\theta}{(c - e_z\cos\theta)^3}((c - e_z\cos\theta) - 2R) \tag{3.113}$$

are obtained. Inserting them yields the final equation

$$u_\theta = 3v_\mathrm{p}\frac{R^2(R-r)}{r}\frac{(c-e_z\cos\theta+r-R)\sin\theta}{(c-e_z\cos\theta)^3} \tag{3.114}$$

for the velocity component u_θ.

Starting from the velocity component u_θ, the shear rate,

$$\frac{du_\theta}{dr} = 3v_\mathrm{p}\frac{R^2}{r^2}\frac{(R(R-c+e_z\cos\theta)-r^2)\sin\theta}{(c-e_z\cos\theta)^3}, \tag{3.115}$$

can be derived. The resulting shear rates at the surfaces are

$$\frac{du_\theta}{dr} = -3v_\mathrm{p}\frac{R\sin\theta}{(c-e_z\cos\theta)^2} \tag{3.116}$$

for $r = R$ at the hemisphere and

$$\frac{du_\theta}{dr} = 3v_\mathrm{p}\frac{R^2\sin\theta}{(c-e_z\cos\theta)^2(R-c+e_z\cos\theta)} \tag{3.117}$$

for $r = R-(c-e_z\cos\theta)$ at the sphere. The shear stress

$$\tau_{r\theta} = 3v_\mathrm{p}\eta\frac{R^2}{r^2}\frac{(R(R-c+e_z\cos\theta)-r^2)\sin\theta}{(c-e_z\cos\theta)^3} \tag{3.118}$$

is obtained by multiplying equation (3.115) with the viscosity η.

The external force F that is required to drive the sphere into the hemisphere can be calculated by integrating the pressure in the fluid film. The resulting integral

$$F = \frac{3R^2\eta v_\mathrm{p}}{e_z}\int_0^R\int_0^{2\pi}\int_0^{\frac{\pi}{2}}\left(\frac{1}{(c-e_z\cos\theta)^2}-\frac{1}{c^2}\right)r\,dr\,d\varphi\,d\theta \tag{3.119}$$

can be evaluated to equal

$$\begin{aligned} F &= 3\pi\frac{R^4\eta v_\mathrm{p}}{e_z}\left[\frac{1}{c^2-e_z^2}\left(\frac{e_z\sin\theta}{c-e_z\cos\theta}+\frac{2c}{\sqrt{c^2-e_z^2}}\arctan\left(\frac{\sqrt{c^2-e_z^2}\tan\frac{\theta}{2}}{c-e_z}\right)\right)-\frac{\theta}{c^2}\right]_0^{\frac{\pi}{2}} \\ &= 3\pi\frac{R^4\eta v_\mathrm{p}}{e_z}\left(\frac{1}{c^2-e_z^2}\left(\frac{e_z}{c}+c\left(\frac{2}{\sqrt{c^2-e_z^2}}\arctan\left(\frac{\sqrt{c^2-e_z^2}}{c-e_z}\right)\right)\right)-\frac{\pi}{2c^2}\right) \end{aligned} \tag{3.120}$$

for $c^2 > e_z^2$ according to Gradshteyn & Ryzhik (1980).

3.3.7 Summary of Analytical Equations

In the preceding subsections four different geometries have been introduced to model the squeezing flow in the human oral cavity. Namely, these are

- plane circular parallel plates (case 1),
- plane elliptic parallel plates (case 2),
- plane and curved circular parallel plates (case 3) as well as
- a sphere in a hemisphere (case 4).

A variety of different physical quantities have been determined analytically for these geometries. Table 3.3 presents the equations for the pressure, velocity, shear rate, shear stress and the force required to drive the geometries together.

3.4 Numerical Simulations

The analytical calculation of fluid flow where an exact function value for any point of a flow field can be quantified is possible in few exceptional cases only. Complex flows with complicated boundary conditions can only be calculated by means of numerical methods

Table 3.3: The basic equations resulting from the four different analytical models considered in the present thesis.

	Case 1	**Case 2**
Pressure	$p - p_0 = 3\frac{\eta v_\mathrm{p}}{h_0^3}(R^2 - r^2)$	$p - p_0 = -6\frac{\eta v_\mathrm{p}}{h_0^3}\frac{a^2 b^2}{a^2+b^2}\left(\frac{x^2}{a^2} + \frac{y^2}{b^2} - 1\right)$
Velocity	$u_r = 3\frac{v_\mathrm{p}}{h_0^2} rz\left(1 - \frac{z}{h_0}\right)$; $u_z = 3\frac{v_\mathrm{p}}{h_0^2} z^2\left(\frac{2}{3}\frac{z}{h_0} - 1\right)$	$u_x = 6\frac{v_\mathrm{p}}{h_0^2}\frac{b^2}{a^2+b^2} xz\left(1 - \frac{z}{h_0}\right)$; $u_y = 6\frac{v_\mathrm{p}}{h_0^2}\frac{a^2}{a^2+b^2} yz\left(1 - \frac{z}{h_0}\right)$
Shear rate	$\frac{du_r}{dz} = 3\frac{v_\mathrm{p}}{h_0^2} r\left(1 - 2\frac{z}{h_0}\right)$	$\frac{du_x}{dz} = 6\frac{v_\mathrm{p}}{h_0^2}\frac{b^2}{a^2+b^2} x\left(1 - 2\frac{z}{h_0}\right)$; $\frac{du_y}{dz} = 6\frac{v_\mathrm{p}}{h_0^2}\frac{a^2}{a^2+b^2} y\left(1 - 2\frac{z}{h_0}\right)$
Shear stress	$\tau_{zr} = 3\frac{\eta v_\mathrm{p}}{h_0^2} r\left(1 - 2\frac{z}{h_0}\right)$	$\tau_{zx} = 6\frac{\eta v_\mathrm{p}}{h_0^2}\frac{b^2}{a^2+b^2} x\left(1 - 2\frac{z}{h_0}\right)$; $\tau_{zy} = 6\frac{\eta v_\mathrm{p}}{h_0^2}\frac{a^2}{a^2+b^2} y\left(1 - 2\frac{z}{h_0}\right)$
Force	$F = \frac{3}{2}\pi\frac{\eta v_\mathrm{p}}{h_0^3} R^4$	$F = 3\pi\frac{\eta v_\mathrm{p}}{h_0^3}\frac{a^3 b^3}{a^2+b^2}$
	Case 3	**Case 4**
Pressure	$p - p_0 = \frac{1}{\beta}\frac{\eta v_\mathrm{p}}{h_0^3}\left(e^{3\beta R^2} - e^{3\beta r^2}\right)$	$p - p_0 = \frac{3R^2\eta v_\mathrm{p}}{e_z}\left(\frac{1}{(c - e_z\cos\theta)^2} - \frac{1}{c^2}\right)$
Velocity	$u_r = 3\frac{v_\mathrm{p}}{h_0^2} rze^{2\beta r^2}\left(1 - \frac{z}{h_0}e^{\beta r^2}\right)$	$u_\theta = 3v_\mathrm{p}\frac{R^2(R-r)}{r}\frac{(c - e_z\cos\theta + r - R)\sin\theta}{(c - e_z\cos\theta)^3}$
Shear rate	$\frac{du_r}{dz} = 3\frac{v_\mathrm{p}}{h_0^2} re^{2\beta r^2}\left(1 - 2\frac{z}{h_0}e^{\beta r^2}\right)$	$\frac{du_\theta}{dr} = 3v_\mathrm{p}\frac{R^2}{r^2}\frac{(R(R - c + e_z\cos\theta) - r^2)\sin\theta}{(c - e_z\cos\theta)^3}$
Shear stress	$\tau_{zr} = 3\frac{\eta v_\mathrm{p}}{h_0^2} re^{2\beta r^2}\left(1 - 2\frac{z}{h_0}e^{\beta r^2}\right)$	$\tau_{r\theta} = 3v_\mathrm{p}\eta\frac{R^2}{r^2}\frac{(R(R - c + e_z\cos\theta) - r^2)\sin\theta}{(c - e_z\cos\theta)^3}$
Force	$F = \frac{1}{3}\pi\frac{\eta v_\mathrm{p}}{\beta^2 h_0^3}\left(e^{3\beta R^2}(e^{3\beta R^2} - 1) + 1\right)$	$F = 3\pi\frac{R^4\eta v_\mathrm{p}}{e_z}\left(\frac{1}{c^2 - e_z^2}\left(\frac{e_z}{c} + c\left(\frac{2}{\sqrt{c^2 - e_z^2}}\arctan\left(\frac{\sqrt{c^2 - e_z^2}}{c - e_z}\right)\right)\right) - \frac{\pi}{2c^2}\right)$

(Kowalczyk, Hartmann & Delgado, 2004, Hartmann, Mathmann & Delgado, 2006). Just as with analytical solutions, these calculations are always approximations of reality. Nevertheless, they are helpful in order to visualize processes, which are difficult to access.

The process of deglutition taking place isolated from any *in vivo* insight belongs to such processes. There is no measurement system that can completely deal with the conditions of the oral cavity, namely the wetness and the difficulty of fixing a system. For this reason, numerical simulations offer the appropriate feasibility for studying the process.

Furthermore, numerical simulations offer

- more detailed information about the flow field,
- information about flow variables that are not measurable directly,
- the possibility to eliminate disturbance variables,
- a more flexible adaptation of input variables as well as
- the advantage of being less expensive and time consuming compared to experimental set-ups

according to Böhme (2000). In computational fluid dynamics, the resulting partial differential equations are subsequently solved using the numerical code.

3.4.1 Procedure of a CFD Analysis

The procedure of a computational fluid dynamics (CFD) analysis starts with the preprocessing. A grid is generated covering the whole geometrical domain of fluid flow. This entails a division into discrete cells called control volumes. The basic equations of fluid flow are an essential part of the selected discrete mathematical model, which is applied on the discrete cells. The application of the model results in solutions for pressure and velocity in every single discrete cell of the entire domain for every single time step. The solution for the entire

domain is merged spatio-temporally based on the results for the single cells (Ferziger & Peric, 2002). In the final step, the fluid flow is visualized by a postprocessor. This enables analysis and interpretation of the numerical calculation.

3.4.2 Discretization Methods

The discretization step approximates the non-linear partial differential equations of fluid flow by transferring them into a system of algebraic equations that can be solved iteratively taking into account initial and boundary conditions. Hence, the function that is the analytical solution of the partial differential equations is replaced by a finite amount of values at discrete locations in space and time. This approximation is made for each small discrete domain, either for each node, volume or element depending on the discretization method.

There are different strategies and algorithms for discretization methods. Ultimately, all of them lead to the same solution for the entire flow field. Three methods have proved of value and are the most important ones, namely the methods of finite differences, finite volumes and finite elements. These methods are introduced concisely in the following. Other methods like spectral schemes, boundary element methods and cellular automata are employed for special classes of problems.

The finite difference method dates back to Leonhard Euler in the 18th century. It is the simplest method for solving partial differential equations and is known to be applied on structured grids only. The basic equations of fluid flow in their differential form as presented above are solved at the grid nodes. For that purpose, the partial derivatives are substituted by difference quotients resulting in a system of difference equations that can be solved by means of implicit and explicit algorithms. Knorrenschild (2003) gives an overview of appropriate algorithms.

The finite volume method is the most frequently used method in computational fluid dynamics currently. The requirements regarding the grid structure are small, leading to the application of more flexible unstructured grids. The finite volume method is based on the

basic equations of fluid flow in their integral form. The integrals are solved by approximations in the centers of each finite volume.

The finite element method is comparable to the finite volume method in many aspects. The main difference is that the equations are multiplied by a weight function, which is defined within the elements before they are integrated over the entire domain.

3.4.3 Types of Grids

Discretization methods are applied on the basis of numerical grids. The grids split the entire geometrical domain into a finite number of discrete locations. They can be structured or unstructured.

The structured grid is the simplest grid structure. The regular grid is aligned along the underlying coordinate system. The grid lines intersect only at the nodes. Therewith, each element has a fixed number of neighbor elements and nodes. Structured grids can only be employed for geometrically simple solution domains and are most frequently used with the finite difference method. In some cases, the appropriate distribution of grid points can be difficult.

On the contrary, unstructured grids are highly flexible for complex geometries. They can have arbitrary shapes and no restrictions concerning the number of neighbor elements and nodes. The most common element shapes are triangles and quadrilaterals in two-dimensional domains and tetrahedra and hexahedra in three-dimensional domains. This grid technique is best adapted to both the finite volume and element methods. The most important disadvantage of this kind of grid is the resulting irregularity of the data structure as the matrices are no longer regular or diagonal.

3.4.4 Software

The numerical analysis of the current study is based on several softwares. Each step - preprocessing, solver, postprocessing - needs its own tool. Due to better availability and

easy access, most components of the current study are open-source pieces of software. In the case of the solver, there is the advantage of being able to program special problem cases by hand. The exact tools that were used in the numerical analysis are introduced below.

The geometry and mesh generation was performed with the commercial software ANSYS ICEM CFD (ANSYS, 2008). The open-source software OpenFOAM (OpenCFD Ltd., 2008) acted as a powerful solver. The postprocessing was done by means of ParaView (Kitware Inc., 2008), which is connected closely with the OpenFOAM concept.

Preprocessing

In a first step it is necessary to build up a geometry of the streamed domain independent from the preprocessor. ANSYS ICEM CFD possesses an integrated CAD engine for this purpose.

Afterwards, the mesh needs to be generated. Figure 3.9 shows the different types of elements available. These are lines, triangles and quadrangles for two-dimensional geometries as well as tetrahedra, hexahedra, prisms and pyramids for three-dimensional geometries. ANSYS ICEM CFD is able to generate both structured and unstructured grids out of these elements.

Due to appropriate converters, OpenFOAM is able to handle meshes generated by any of the major CAD and meshing tools. In the current study, the converter `ansysToFoam` was

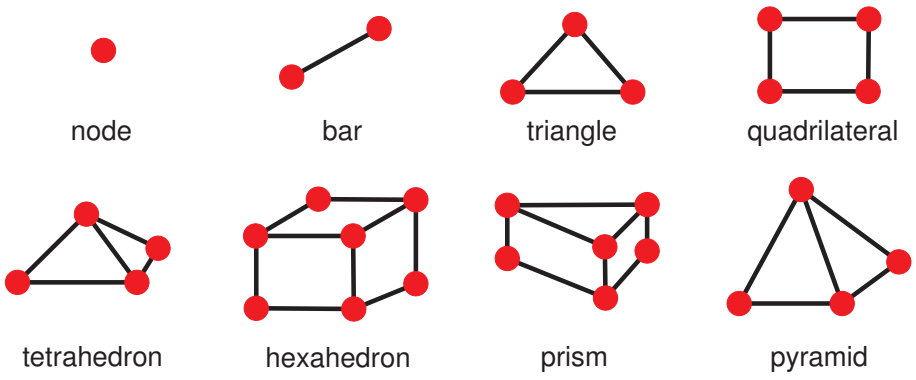

Figure 3.9: The types of elements that can be generated for use in a CFD simulation.

applied in order to transform the geometries and meshes into the format of OpenFOAM.

Solver

The principles of the open-source software OpenFOAM (Open Field Operation and Manipulation) were introduced by Weller, Tabor, Jasak & Fureby (1998). OpenFOAM is a numerical tool for solving partial differential equations of any kind. The solvers are based on C++ modules. The wide range of solvers that are already implemented can be viewed on the website. Emphasis is put on continuum mechanics including computational fluid mechanics. The CFD codes are based on the finite volume method. The different problem-specific solvers are grouped to the topics "basic" CFD codes, incompressible flow, compressible flow, multiphase flow, direct numerical simulation and large eddy simulation, combustion, heat transfer, electromagnetics, stress analysis of solids and even finance.

The solvers that belong to the group of incompressible flow are relevant for the current study. In order to simulate Newtonian fluid flow, the solver `icoDyMFoam` was employed. This solver allows the calculation of laminar and transient flows considering dynamic meshes. For simulating the non-Newtonian fluid flow it was necessary to program a new solver. This took place on the basis of the `nonNewtonianIcoFoam` solver, which supports the calculation of laminar non-Newtonian and transient flow but not dynamic meshes. The new solver was generated analogously to the `icoDyMFoam` solver. The developed `nonNewtonianIcoDyMFoam` code can be found in appendix C. The solvers access the Newtonian module, which contains a linear viscous fluid model, as well as `CrossPowerLaw` and `BirdCarreau`, which both contain nonlinear viscous models.

The solvers output data in terms of pressure and velocity, as well as viscosity in the non-Newtonian case. Additional modules of OpenFOAM are able to transfer these data into the required gradients. The `magU` module calculates the scalar magnitude of the velocity field u_i at each time. Another useful module is `magGradU`, which calculates and writes the scalar magnitude of the gradient of the velocity field u_i for each time.

Postprocessing

Once the necessary data are generated they are transformed into an appropriate format for postprocessing. OpenFOAM features several data converters, which allow the subsequent analysis by means of third party products like Fluent or EnSight. The converter used in the current study is the `foamToVTK` converter. It converts data from its native format to the VTK format. VTK (Visualization Toolkit) is a platform independent open-source graphics toolkit. It is used by ParaView as a data-processing and rendering engine.

The ParaView open-source visualization application represents data in structured as well as in unstructured grids. The software quickly builds visualizations of even extremely large data sets so that they can be analyzed by qualitative and quantitative techniques. Therefore, ParaView needs a list of the grid points with the associated data that is to be visualized. These data are recorded in separate text files.

3.4.5 Introduction of the Geometrical Model

The current thesis continues the previous study of a two-dimensional numerical approach (Mathmann, Kowalczyk, Petermeier, Baars, Eberhard & Delgado, 2007). The aim of that study was to determine numerically the fluid-mechanical forces occurring in food suspensions using a simplified tongue-palate model system consisting of two parallel plates. The calculations by means of the Stefan equation proved the appropriateness of numerical methods for the investigation of fluid flow in models of the oral cavity. Due to this validation of the model consisting of two plane circular parallel plates, further comparisons of numerically and analytically calculated properties of squeezing flows for other geometries have not been performed as it is very likely they will give identical results leading to redundant data. Accordingly, the two-dimensional model used in the first numerical study has been extended to a more complex three-dimensional model directly. However, this model can be considered as the logical continuation of the geometrical models that are discussed analytically.

Figure 3.10 shows the geometry of the model based on the dentist replicas introduced

in section 3.1. The duct-like extension was constructed in order to mimic the upper part of the pharynx. It is 22.5 mm wide and 30 mm long at the outer border.

The geometry is split into 57440 hexahedral elements composing a structured grid. The initial distance between the two ellipsoids is 10 mm, the deformation at the tip of the tongue 9 mm. Due to the movement, the fluid is forced to squeeze out at the rear part of the model.

The density $\rho = 1000$ kg/m^3 is defined for all simulation runs. As the code requires the viscosity in terms of the kinematic viscosity ν the density ρ is specified indirectly via the quotient

$$\nu = \frac{\eta}{\rho} \tag{3.121}$$

of the dynamic viscosity η and the density ρ.

The initial and boundary conditions also remain constant for all simulation runs. The pressure is $p = 0$ at the outflow resulting in an analysis of the dynamic part. The pressure gradient is set to zero at all other surfaces. The initial pressure in the whole field is $p = 0$. The velocity gradient at the outflow is zero. The velocity at the palate and at the sides is $u_i = 0$. The initial velocity field is $u_i = 0$. The boundary condition at the tongue is defined by the `movingWallVelocity` module. The moving velocity of the model tongue increases linearly from $v_z = 0$ cm/s at the outflow to $v_z = 1$ cm/s at the tip of the model tongue. The temporal discretization takes place by the first-order EULER method.

The simulations were performed using four different Newtonian fluids exhibiting constant viscosities. A single simulation of a non-Newtonian fluid was also performed. The rheological constants used for this simulation were determined by modeling the fluid-flow behavior of yogurt with the CROSS model (see section 4.1).

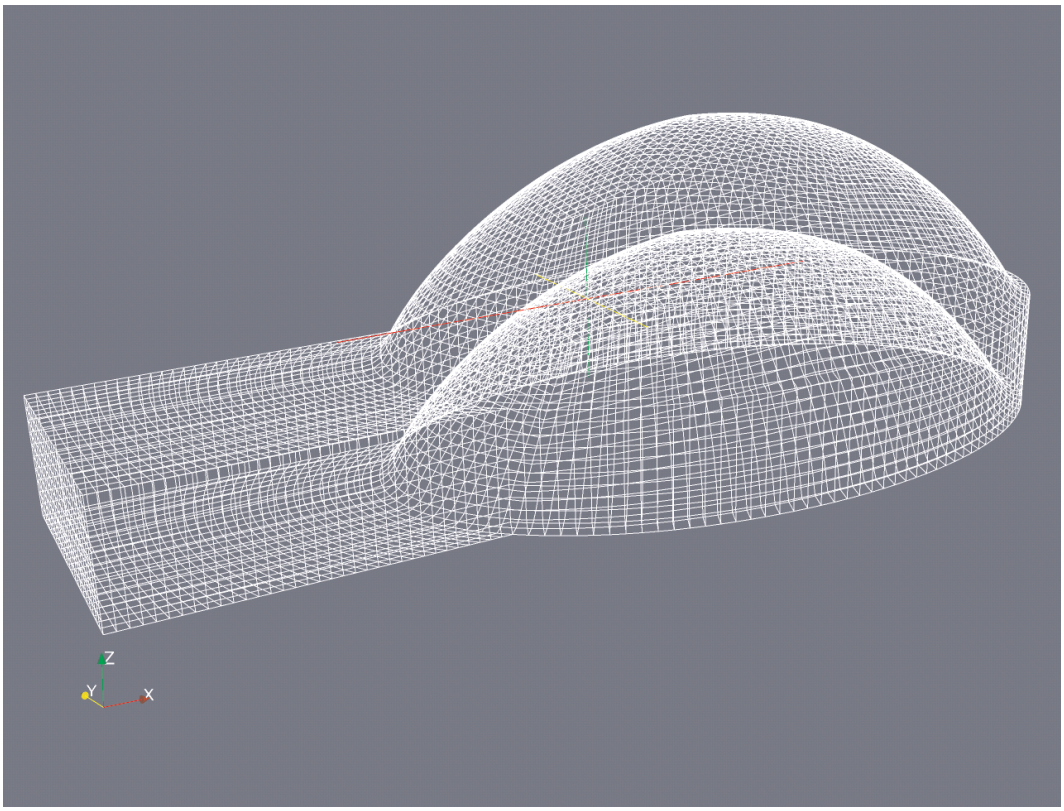

Figure 3.10: The geometrical configuration and grid in the initial state of the simulations.

Chapter 4

Results and Discussion

This chapter presents the results obtained from the rheological measurements, the theory of lubrication and the numerical simulations. The chapter begins with the presentation of the results from the rheological characterization of four different yogurt samples. The Cross model is used to fit the data from one of the yogurt flow curves as an example. The values that were found for the parameters act as input data for the numerical simulation incorporating a non-Newtonian fluid.

The models derived by means of the theory of lubrication yield pressure, velocity, shear rate and shear stress distributions for each approach. In addition, the force that is required to drive the geometries together is investigated. The data are compared and conclusions are drawn concerning the suitability of the different models to represent the human oral cavity realistically. The results give a clue concerning the values that can be expected in the numerical simulations.

The evaluation of the numerical simulation is split into subsections dealing with each fluid-mechanical quantity. The values resulting from the different numerical models are discussed and collated. Afterwards, the results are compared with those of the theory of lubrication and the literature.

The velocity of the moving part of the geometry representing the tongue employed is the same in all studied cases. According to Lee & Camps (1991), the residence time of fluids

in the oral cavity is dependent on the viscosity but is brief in any case. The values vary between 1 s for water, 1.5 s for whipped cream and 3 s for honey. Assuming a gap of 1 cm between the tongue and palate gives a moving velocity of approximately 1 cm/s.

4.1 Rheological Measurements and Fittings

The rheological behavior of yogurt was measured by means of a rotational rheometer. The rheometer employed for this study was the RC30-CPS from RheoTec Messtechnik GmbH, Germany, with the C75-2 cone and plate system. This means that the cone diameter is 75 mm and the cone angle is 2°.

Four different yogurts were characterized. They can be distinguished due to their fat contents of 0.1%, 1.5%, 3.5% and 3.8%, respectively. These yogurts were produced by two different German manufacturers A and B. The samples were stored in a refrigerator at 7°C and took out immediately before the measurement. After they were put on the plate of the rheometer they were heated to 25°C within 30 s.

Afterwards, each sample was characterized rheologically at eight constant shear rates for 30 s. Within this period of time, the gel structure of the samples is irreversibly destroyed. All shear rates lay in the range between $0.3\,\mathrm{s}^{-1}$ and $100\,\mathrm{s}^{-1}$. The minimum value is the smallest value that is obtainable with this model of rheometer. The maximum value was chosen according to Wood (1968) who reported that oral shear rates were in this range. Previous numerical studies employing two parallel plates have confirmed this range (Mathmann et al., 2007). Figure 4.1 shows the measurement of the yogurt containing 3.8% fat at a constant shear rate of $\dot{\gamma} = 100\,\mathrm{s}^{-1}$. The curve shows that the structural breakdown of yogurt occurs quickly after applying stress. Starting with a shear stress of $\sigma = 51.60$ Pa, the shear stress decreases to $\sigma = 41.53$ Pa. This corresponds to a reduction of 20%.

According to Suwonsichon & Peleg (1999) and Mullineux & Simmons (2008), the apparent viscosity of yogurt decreases irreversibly as a function of shear rate and time. Because of the breakdown of the structure it was necessary to renew the samples after each

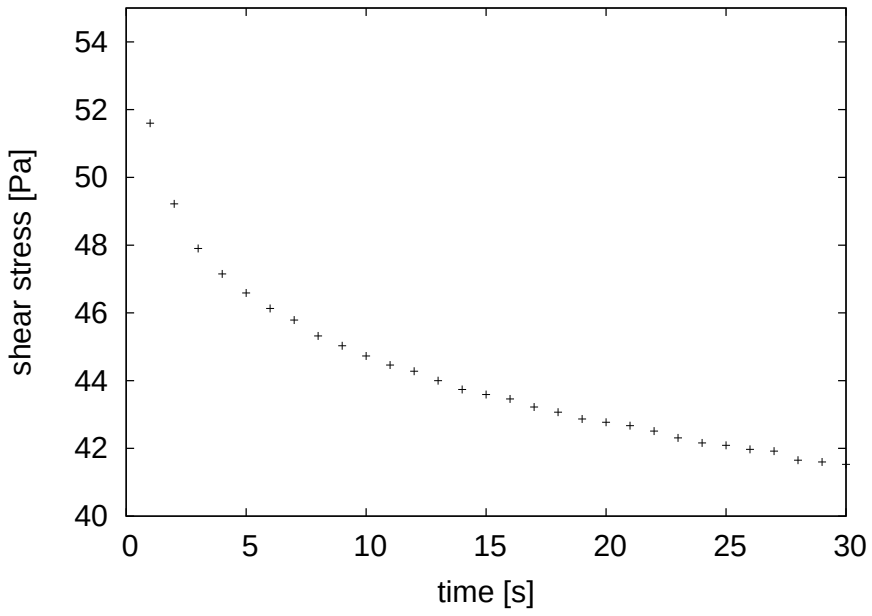

Figure 4.1: The flow curve of yogurt containing 3.8% fat measured for 30 s at a constant shear rate of $100\,\mathrm{s}^{-1}$.

measurement to eliminate this effect in the current study. As yogurt is swallowed quite quickly during normal consumption only the values of the shear stress measurements before the structure breaks down are considered to be important. For this reason, the flow curves were constructed by averaging the first two measurements of the shear stress recorded 1 s and 2 s after applying a particular shear rate. Figure 4.2 shows the result with both linear and logarithmic x-axis scales.

Figure 4.2a shows that yogurt exhibits a shear-thinning fluid-flow behavior like most foodstuffs do. For small shear rates the shear stresses drop down strongly. Figure 4.2b suggests that this tendency continues for even smaller shear rates. Hence, the measurements show the behavior that could be expected following the hypothesis of Barnes & Walters (1985) and the experimental data of Krulis & Rohm (2004). This means that yogurt, in contrast to the popular opinion, does not exhibit a yield stress and that its rheological behavior can be described by the Cross model.

The position of the flow curve depends mainly on the fat content. The higher the fat content, the higher the shear stresses become for each shear rate. The flow behavior of

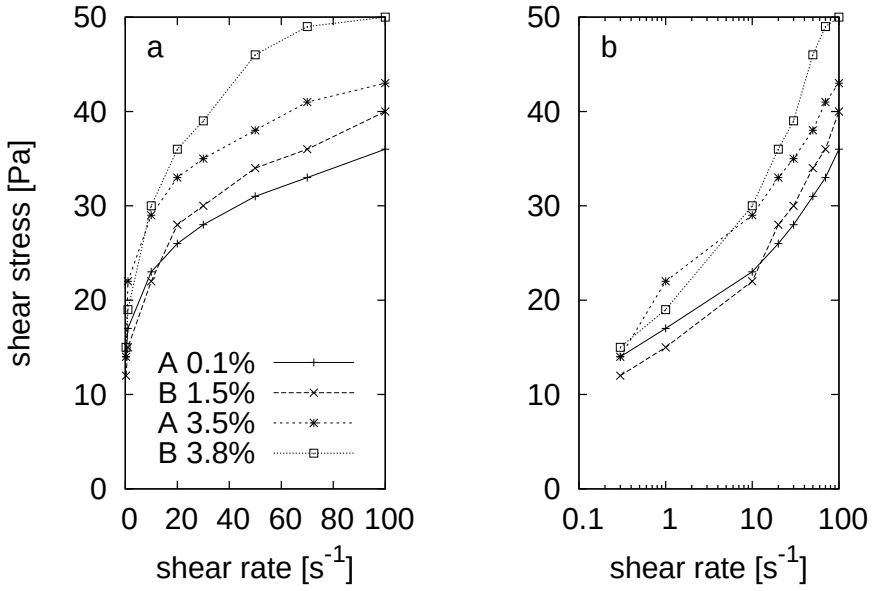

Figure 4.2: The flow curves of four different yogurts of the manufacturers A and B varying in their fat content (0.1%, 1.5%, 3.5% and 3.8%) neglecting their time-dependence by taking into consideration only the data recorded before the structural breakdown takes place for (a) linear and (b) logarithmic x-axis scales.

the yogurts of the same manufacturer is qualitatively equal. This can be seen from the curves, which display the same shape but are shifted along the ordinate. The crossing of the curves in the range of low shear rates might depend on both the different composition of the ingredients as well as the different processing parameters used by the two different manufacturers.

The differences of the diverse yogurts concerning their mouthfeel are evaluated in a separate paper (Mathmann, Kowalczyk & Delgado, 2009). It is important to keep in mind that the measured properties of the yogurt samples do not necessarily agree with the properties of the same samples during consumption. It could be shown that the four different yogurts, which behaved similar from a rheological point of view, were judged very differently in sensory terms. Hence, food rheology is an important main pillar for the description of food but not the only one. Nevertheless, the flow curves were employed exclusively in the current thesis as they have a sound physical basis. Other descriptions of food-matter properties are

still vague or even unknown. For that reason, the complexity of foodstuffs cannot be fully described.

The measured flow curves of yogurt act as input for the numerical simulations. For this purpose, the flow curves were fitted using the Cross law. The fit function of gnuplot (Williams & Kelley, 2008), an open-source software that generates two- and three-dimensional plots of functions and data, enables the fitting of a user-defined function to a set of data points via defined variables. The user-defined function in the current case is equation (3.5).

The data points used in the fitting process were those obtained from the rheological measurements of the yogurt sample from manufacturer B that contained 1.5% fat. The shear rate $\dot{\gamma}$ and shear stress σ are recorded directly. The apparent kinematic viscosity needed for the fitting is calculated by $\nu = \frac{\sigma}{\rho\dot{\gamma}}$. The employed density ρ is defined 1000 kg/m^3, the apparent dynamic viscosity η_∞ at the zero-shear rate is approximately set 100 Pas. The initial values for the fitting parameters were $\nu_\infty = 10^{-5}$ m^2/s, $m = 0.95$ s and $n = 1$. Figure 4.3 shows the result. The dots represent the data measured by the rheometer, while the line represents the fitted function.

The range of apparent viscosities covers a wide spectrum. In the range of low shear rates, from $1\,\mathrm{s}^{-1}$ up to $10\,\mathrm{s}^{-1}$, the apparent viscosity lies in the range between 0.015 m^2/s and 0.002 m^2/s. This value is between three to four orders of magnitude larger than the value for water. The apparent viscosity decreases to 0.0004 m^2/s at a shear rate of $100\,\mathrm{s}^{-1}$. This is still a hundred times larger than the value of water.

The final values of the Cross law variables are displayed in a log file, which is generated while performing the fitting process. The fit of eight data points converged after six iterations. The final set of parameters is $\nu_\infty = 7.88204 \cdot 10^{-4}$ m^2/s, $m = 3.74197$ s and $n = 1.34874$. These parameters are inserted into OpenFOAM for access by the module `CrossPowerLaw`.

In order to introduce the different rheological constants used in the numerical calculations, it is most convenient to present the varying key data in a table. Table 4.1 assigns labels

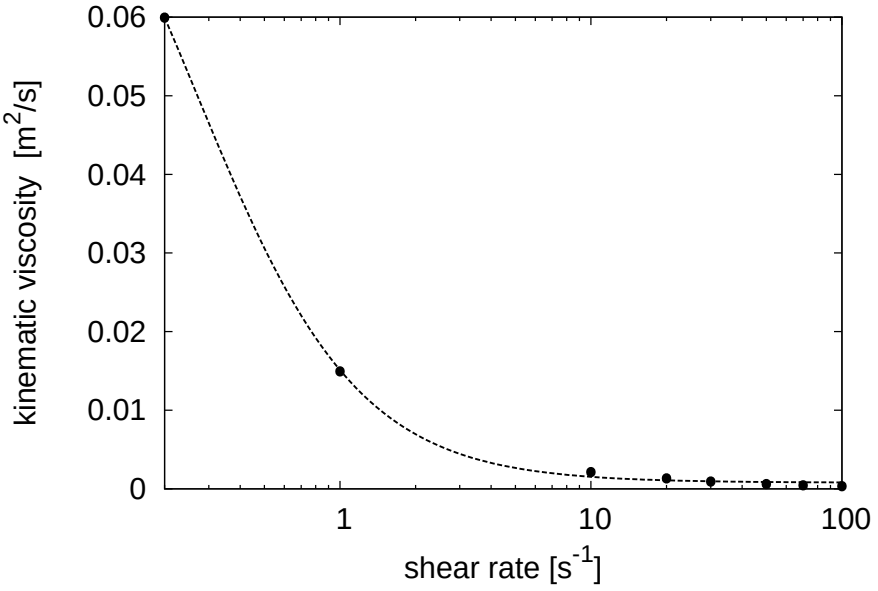

Figure 4.3: The experimental data of the kinematic viscosity ν of yogurt containing 1.5% fat versus the shear rate $\dot{\gamma}$ fitted by the Cross law.

to the different simulation runs and the applied viscosity model with the related rheological constants. The first four runs deal with the Newtonian (N) fluid flow behavior. The runs can be distinguished by the implemented dynamic viscosity ν_0.

Case N1 uses the viscosity of water. Cases N2 and N3 employ slightly higher viscosities. According to Zürcher & Kursawe (1973), those values are the minimum and maximum viscosities occurring in beer within the drinking temperature range of 10°C and 20°C. The authors state that the beer drinker is able to distinguish between these viscosities. The associated simulations serve as an estimate of importance of viscosity related mouthfeel during beer enjoyment. Case N4 uses a hundredfold-higher viscosity than water. Vegetable oils like olive oil exhibit this viscosity. Furthermore, the apparent viscosities of yogurt decreases to this level (see figure 4.3). For this reason, this viscosity is the value used in the analytical approach presented in the following section. The last case CL deals with non-Newtonian fluid-flow behavior fitted by the Cross law as described above.

4.2 Theory of Lubrication

The results of the theory of lubrication are subdivided into the four different approaches of squeezing flow introduced and derived in sections 3.3.3 to 3.3.6. As the fluid flow takes place in the sagittal plane of the oral cavity the focus is mainly on the key points in this plane.

4.2.1 Plane Circular Parallel Plates - STEFAN Equation

The STEFAN equation (3.30) gives a parabolic profile for the pressure distribution $p-p_0$ along the radial coordinate r. Inserting the dynamic viscosity $\eta = 100$ mPas, which lies in the order of magnitude of vegetable oils like olive oil and the apparent viscosity of yogurt presented in the previous section, the uniform plate velocity $v_\mathrm{p} = 1\,\mathrm{cm/s}$ determined in section 3.4.5, the minimum film thickness $h_0 = 1$ mm and the plate radius $R_{\mathrm{p}2} = 29$ mm yields the pressure distribution illustrated in figure 4.4. The maximum pressure difference $p - p_0$ in the center of the plates for this configuration is 2523 Pa.

In order to present the impact of the different radii that can be found in table 3.2, figure 4.5 depicts the maximum pressures occurring in the center of the plates depending on their radius. The STEFAN equation (3.30) simplifies to

$$p_\mathrm{max} - p_0 = 3\frac{\eta v_\mathrm{p}}{h_0^3}R^2 \tag{4.1}$$

for this purpose. The values inserted for the dynamic viscosity η, the uniform plate velocity v_p and the minimum film thickness h_0 remain the same.

The maximum pressure goes from 972 Pa to 3675 Pa for the plate radius varying between 18 mm and 35 mm. Over this range of realistic dimensions for the oral cavity, a huge pressure difference of 2703 Pa is encountered.

The velocity components are evaluated together in terms of the magnitude of velocity.

Table 4.1: The varying rheological key data implemented in the simplified three-dimensional model of the oral cavity.

Label	**Viscosity model**	**Rheological constants**	**Example**
N1	Newtonian	$\nu_0 = 1.0 \cdot 10^{-6}$ m^2/s	water
N2	Newtonian	$\nu_0 = 1.6 \cdot 10^{-6}$ m^2/s	beer (20°C)
N3	Newtonian	$\nu_0 = 3.2 \cdot 10^{-6}$ m^2/s	beer (10°C)
N4	Newtonian	$\nu_0 = 1.0 \cdot 10^{-4}$ m^2/s	vegetable oil
CL	Cross law	$\nu_0 = 1.0 \cdot 10^{-1}$ m^2/s	yogurt
		$\nu_\infty = 7.9 \cdot 10^{-4}$ m^2/s	
		$m = 3.74197$ s	
		$n = 1.34874$	

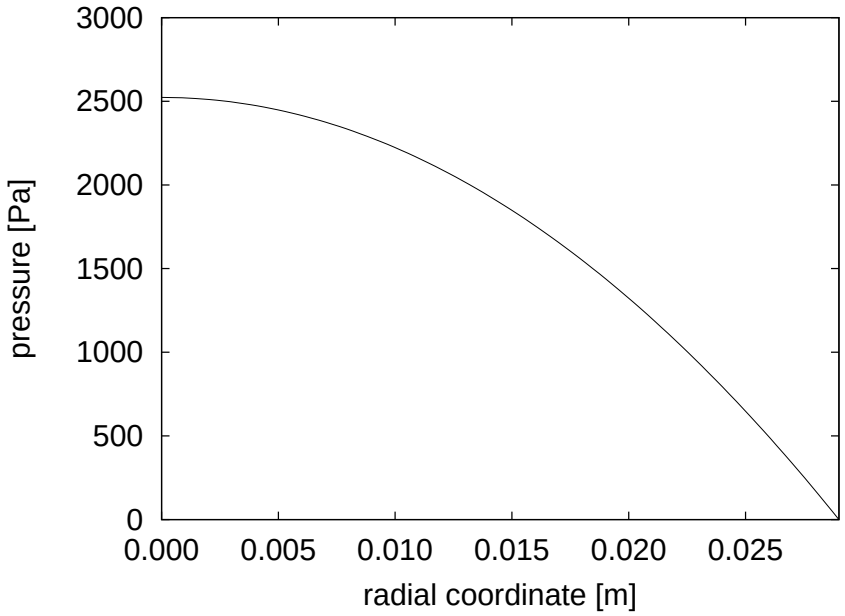

Figure 4.4: The pressure distribution $p-p_0$ between plane circular parallel plates according to the Stefan equation (3.30) with $\eta = 100$ mPas, $v_\mathrm{p} = 1$ cm/s, $h_0 = 1$ mm and $R_{\mathrm{p}2} = 29$ mm.

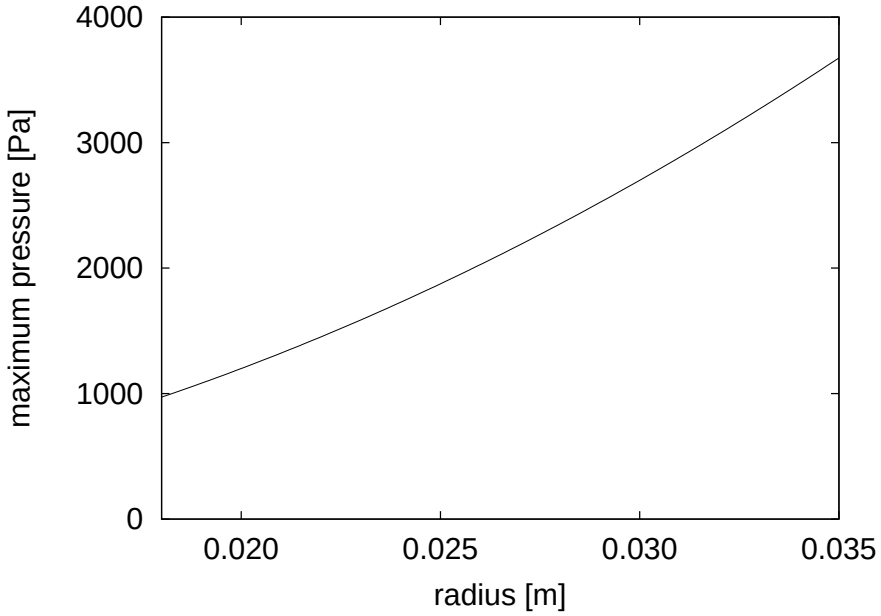

Figure 4.5: The maximum pressures $p_{\max} - p_0$ between plane circular parallel plates according to equation (4.1) in dependence on the outer plate radius R with $\eta = 100$ mPas, $v_\mathrm{p} = 1$ cm/s and $h_0 = 1$ mm.

Taking equations (3.42) and (3.47) into account, the equation

$$u_\mathrm{mag} = \sqrt{u_r^2 + u_z^2} = \sqrt{\left(3\frac{v_\mathrm{p}}{h_0^2} r z \left(1 - \frac{z}{h_0}\right)\right)^2 + \left(3\frac{v_\mathrm{p}}{h_0^2} z^2 \left(\frac{2}{3}\frac{z}{h_0} - 1\right)\right)^2} \tag{4.2}$$

is achieved. Figure 4.6 shows the magnitude of velocity u_mag along the radial coordinate r in the middle of the gap at $z = 0.5$ mm. The magnitude of velocity in the middle of the gap increases linearly apart from the small non-linear interval in the middle of the plates, where the velocity in z-direction dominates. This behavior could be expected as the equation for the velocity component u_z (3.47) is independent from the radial coordinate r and the equation for the velocity component u_r (3.42) is a linear function of the radial coordinate r. The magnitude of velocity starts with 5 mm/s in the middle of the plates and reaches 218 mm/s at the outflow.

Figure 4.7 shows the determined velocity profiles along the gap for four different values of the radial coordinate. In the middle of the plates, only the velocity component u_z contributes

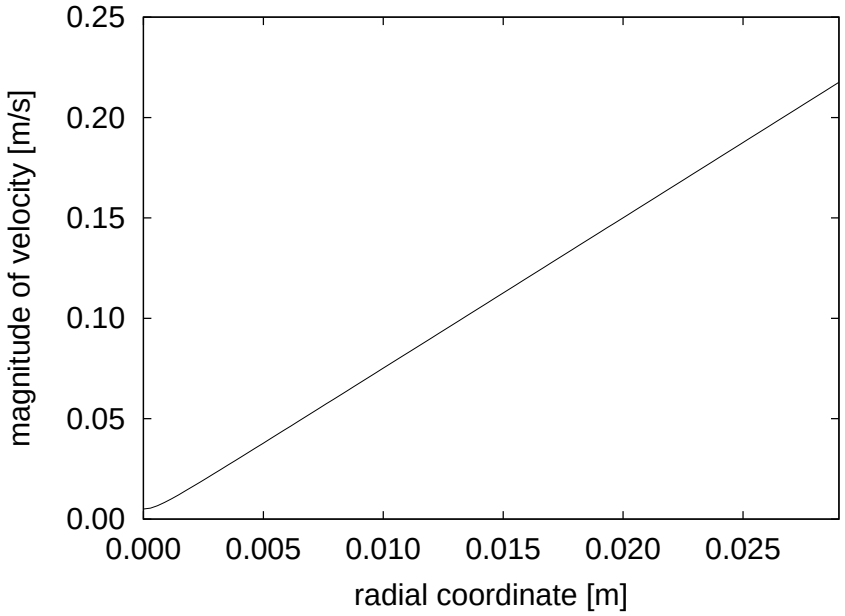

Figure 4.6: The magnitude of the velocity u_{mag} in the middle of the gap at $z = 0.5$ mm between plane circular parallel plates according to equation (4.2) with $\eta = 100$ mPas, $v_{\mathrm{p}} = 1$ cm/s, $h_0 = 1$ mm and $R_{\mathrm{p2}} = 29$ mm.

to the result. In all other cases, the velocity components are superposed. Independent from the radial coordinate, the magnitude of velocity is 0 m/s at $z = 0$ mm and 1 cm/s at $z = 1$ mm due to the no-slip condition. The maximum magnitude of the velocity is reached in the middle of the gap.

Both, figures 4.6 and 4.7 show that the velocity increases with the radial coordinate, r. This is understandable considering the volume flow rate. The volume of the fluid that is squeezed down by the movement of the upper plate must flow out at the radius R of the plates. The upper plate squeezes a volume flow rate of $\dot{V} = \pi R^2 v_{\mathrm{p}}$ dependent on the radius R. The volume flow rate of the fluid across the radius R is $\dot{V} = 2\pi R h_0 \bar{u}$. For this reason, the averaged velocity $\bar{u}$ is proportional to the radius R.

The absolute values of the shear rate $\frac{du_r}{dz}$ at the surfaces of the plates are calculated according to equations (3.49) and (3.50). The derivative of the velocity u_r with respect to z is a linear function of the radial coordinate r. The result is shown in figure 4.8. The shear rate increases to the maximum value of $870\,\mathrm{s}^{-1}$ at the outflow.

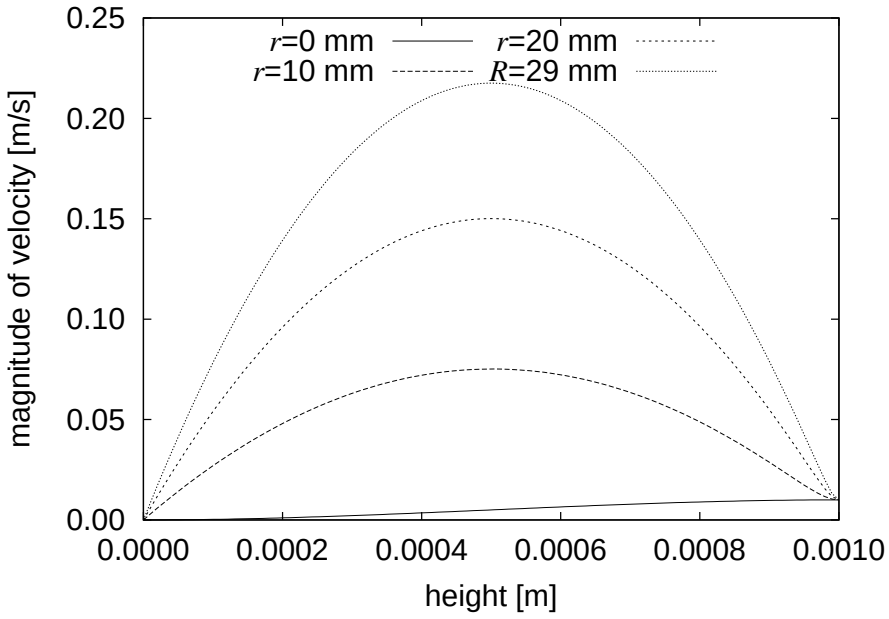

Figure 4.7: The magnitude of velocity u_{mag} along the height of the gap h_0 at different points between plane circular parallel plates of radius R, according to equation (4.2) with $\eta = 100$ mPas, $v_{\mathrm{p}} = 1$ cm/s, $h_0 = 1$ mm and $R_{\mathrm{p2}} = 29$ mm.

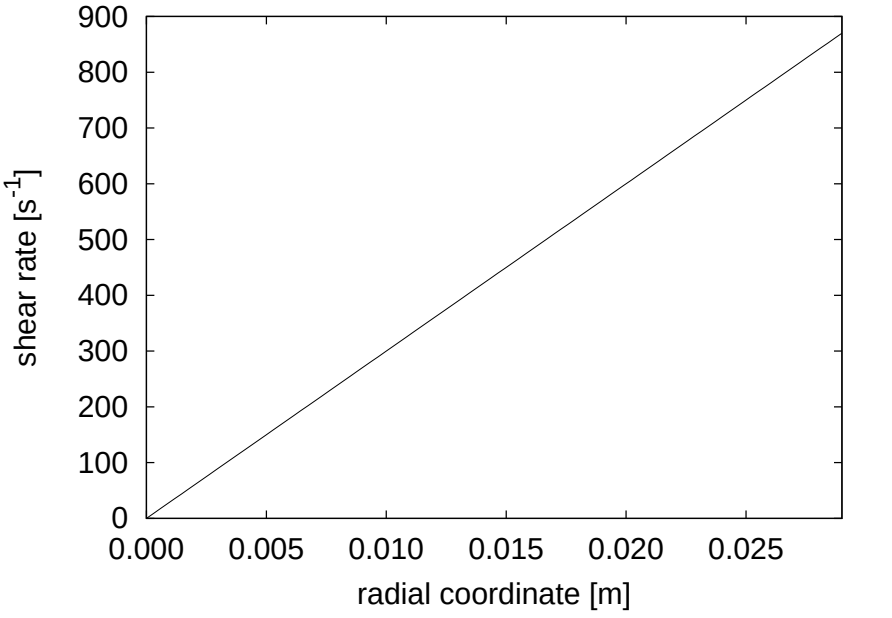

Figure 4.8: The absolute values of the shear rate $\frac{du_r}{dz}$ at the surfaces of the plane circular parallel plates according to equations (3.49) and (3.50) with $v_{\mathrm{p}} = 1$ cm/s, $h_0 = 1$ mm and $R_{\mathrm{p2}} = 29$ mm.

For Newtonian fluids, the absolute value of the shear stress τ_{zr} is a multiple of the shear rate. This means that the form of the curve in figure 4.8 remains the same and the shear stress is not plotted for this reason. The maximum absolute value of the shear stress is 87 Pa for viscosity $\eta = 100$ mPas.

Figure 4.9 shows the force that is required to drive the two plates together. The force increases with the fourth power of the radius R. The force for the smallest plate radius of 18 mm is 0.5 N, while the force for the biggest plate radius of 35 mm is 7.0 N.

4.2.2 Plane Elliptic Parallel Plates

In the case of the plane elliptic parallel plates, two configurations are considered as examples. In the first configuration quantities are evaluated along the transverse projectional plane. The dimensions of the oral cavity are $R_{\mathrm{p1}} = 18$ mm for the semi-minor axis of the ellipse and $R_{\mathrm{p2}} = 29$ mm for the semi-major axis. The second configuration is based on radii taken from the arcs of circles in the frontal and the sagittal planes. Hence, the semi-minor axis has the length $R_{\mathrm{a1}} = 26$ mm and the semi-major axis $R_{\mathrm{a2}} = 35$ mm. The dynamic viscosity is $\eta = 100$ mPas, the uniform plate velocity $v_{\mathrm{p}} = 1$ cm/s and the minimum film thickness $h_0 = 1$ mm once again. Figure 4.10 shows the pressure distribution in the cross section along the semi-major axis of the ellipses resulting from equation (3.61). The pressure distribution again has a parabolic shape. The maximum value for the pressure that arises for these values of the semi axes R_{p1} and R_{p2} is 1403 Pa. The geometrical set-up with the semi axes R_{a1} and R_{a2} gives a maximum pressure of 2614 Pa.

Introducing the ratio of axes $c_{\mathrm{e}} = \frac{b}{a}$, the equation (3.61) can be simplified yielding

$$p_{\max} - p_0 = 6\frac{\eta v_{\mathrm{p}}}{h_0^3}\frac{c_{\mathrm{e}}^2}{1 + c_{\mathrm{e}}^2}a^2 \tag{4.3}$$

for the maximum pressure at $x = y = 0$ mm. For the special case $c_{\mathrm{e}} = 1$, the equation adopts the same form as for the plane circular parallel plates [equation (4.1)]. For any constant ratio c_{e}, the maximum pressure increases with the square of the semi-major axis a.

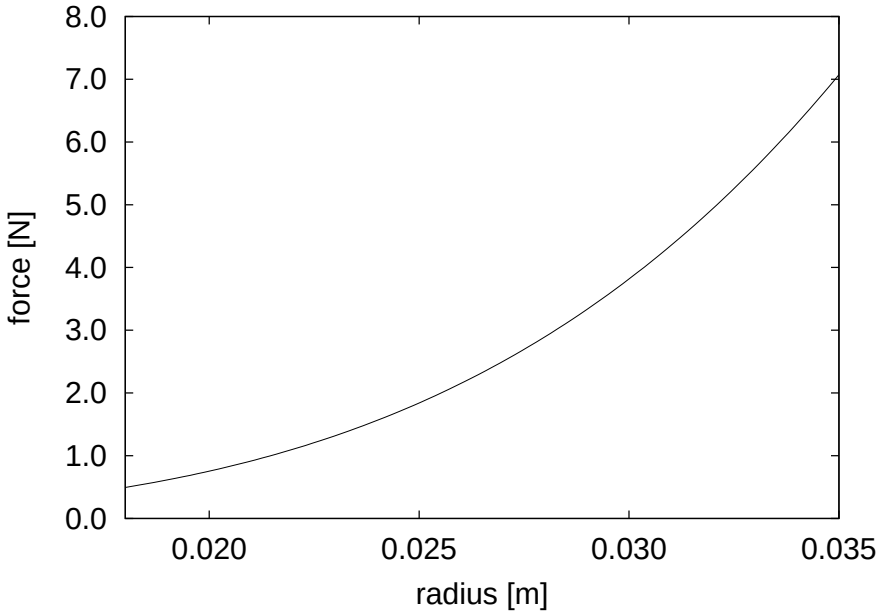

Figure 4.9: The external force F required to drive plane circular parallel plates of different radii together according to equation (3.55) with $\eta = 100$ mPas, $v_\mathrm{p} = 1$ cm/s and $h_0 = 1$ mm.

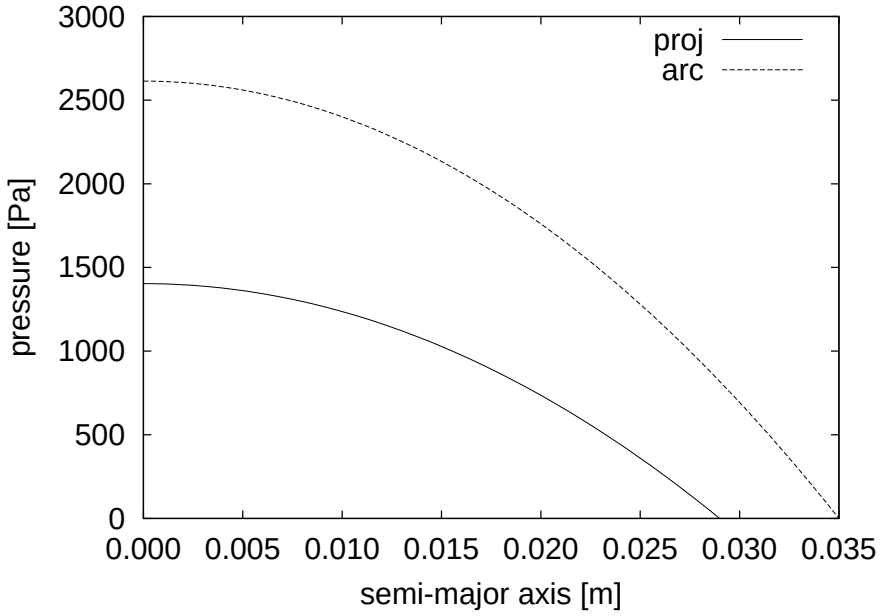

Figure 4.10: The pressure distributions $p - p_0$ between plane elliptic parallel plates along the semi-major axis according to equation (3.61) with $\eta = 100$ mPas, $v_\mathrm{p} = 1$ cm/s and $h_0 = 1$ mm for the semi axes $R_{\mathrm{p}1} = 18$ mm and $R_{\mathrm{p}2} = 29$ mm (projection), and $R_{\mathrm{a}1} = 26$ mm and $R_{\mathrm{a}2} = 35$ mm (arc), respectively.

In the present study, the ratio of the axes is not the same for the arc and projection configurations. It is 0.62 for the projection configuration and 0.74 for the arc configuration. In order to demonstrate the influence of altering ratios c_e, figure 4.11 shows the maximum pressure distribution for both semi-major axes. Concerning the semi-major axis R_{p2}, the pressure increases from 1401 Pa for the ratio $c_e = 0.62$ to 2523 Pa for the ratio $c_e = 1$ representing the system of plane circular parallel plates. The pressures arising according to the semi-major axis R_{a2} are 2041 Pa and 3675 Pa. This means that the maximum occurring pressure of the elliptic configuration is 44% smaller compared to the circular one for a minimum ratio $c_e = 0.62$. For this reason, the shape of plates is of vital importance in the plane configuration.

A comparison between plane circular and elliptic plates using equal plate areas can also be performed. The corresponding radii of the circles can be calculated by $r = \sqrt{ab}$ yielding 23 mm and 30 mm for the configurations discussed above. The corresponding maximum pressures can be calculated as being 1566 Pa and 2730 Pa (figure 4.5). Considering the same areas for both shows that the maximum pressures are smaller for ellipses than for circles. In the case of the projection configuration, the difference is about 10%; in the case of the arc configuration, it is only 4%. Keeping in mind the ratio of the axes, it can again be stated that the difference diminishes the more the ratio c_e converges to 1. Nevertheless, the elliptic shape of the oral cavity suggests that the result of the STEFAN equation (3.30) should be corrected by an factor of up to 10%.

Figure 4.12 shows the magnitudes of the velocity in the main fluid-flow direction along the ellipse axes. In analogy to equation (4.2), the underlying equation equals the square root of the sum of the squares of the velocity components in the x- and z-directions as well as the y- and z-directions [equations (3.47), (3.69) and (3.70)]. The resulting magnitudes of velocity are again linear along the axis apart from the small interval at the middle of the plates where the velocity component in the z-direction dominates. They are bigger along the minor axes than along the major axes. This can be expected from equations (3.69) and (3.70).

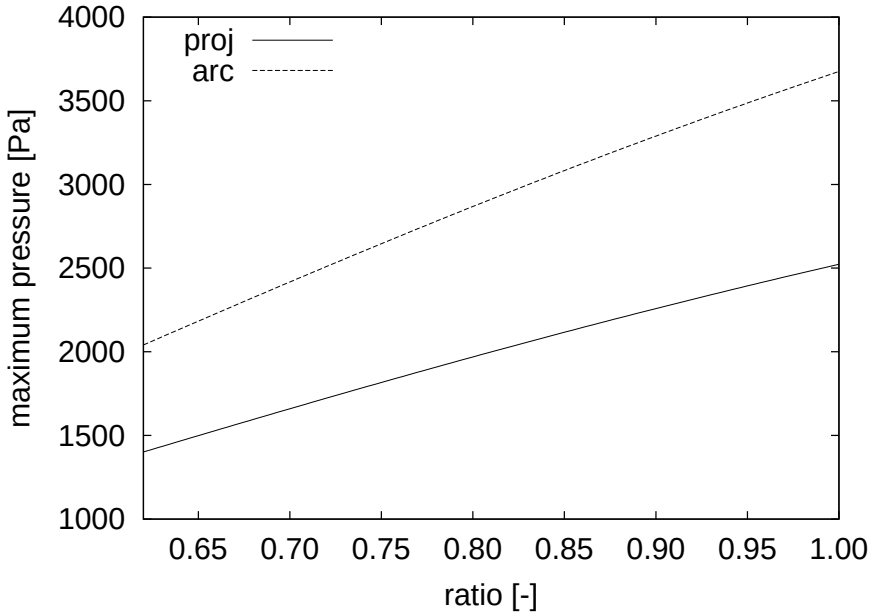

Figure 4.11: The maximum pressures $p_{\max} - p_0$ between plane elliptic parallel plates according to equation (4.3) in dependence on altering ratios c_e with $\eta = 100$ mPas, $v_p = 1$ cm/s and $h_0 = 1$ mm for the semi-major axes $R_{p2} = 29$ mm (projection) and $R_{a2} = 35$ mm (arc), respectively.

Physically, there must be the same pressure difference between the maximum pressure in the middle of the plates and the ambient pressure p_0 at the outflow at any angle φ. For that reason, the pressure gradient must be smaller the further the boundary of the geometry is from the central point. Consequently, the bigger gradient along the semi-minor axis results in larger velocity magnitudes in this direction. For the same reason, it can be expected that the gradient of the magnitude of velocity is bigger in the projection configuration than in the arc configuration, as the ratio c_e of the axes is smaller. The maximum occurring velocities are 121 mm/s at the outer major axis and 192 mm/s at the outer minor axis in the projection geometry, and 187 mm/s at the outer major axis and 250 mm/s at the outer minor axis in the arc configuration. These results are in the same order of magnitude as in the case of plane circular parallel plates.

Figure 4.13 shows the absolute values of the shear rates at the surfaces of the elliptic plates calculated on the basis of the equations (3.74) and (3.75). The shear rate increases

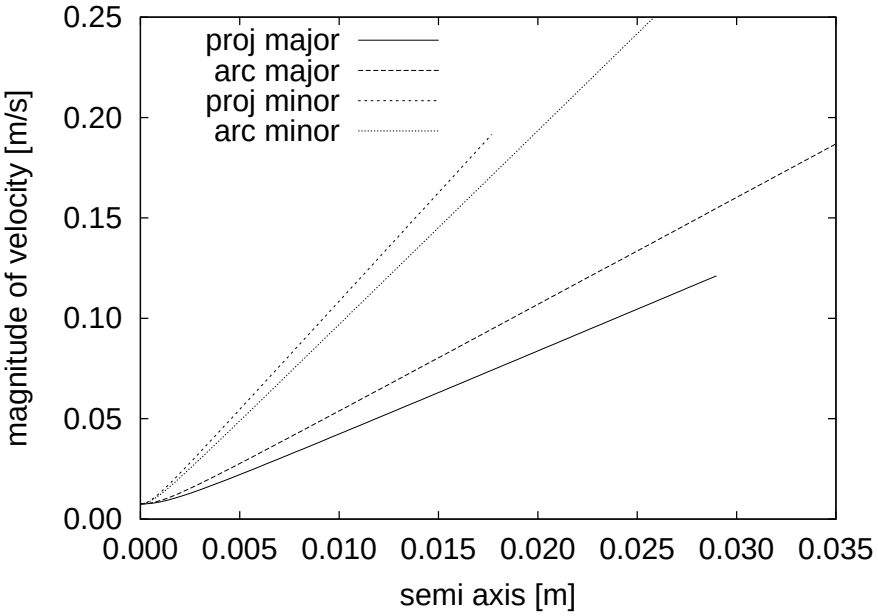

Figure 4.12: The magnitude of velocity u_{mag} in the middle of the gap at $z = 0.5$ mm between plane elliptic parallel plates according to equations (3.47), (3.69) and (3.70) with $\eta = 100$ mPas, $v_{\mathrm{p}} = 1$ cm/s and $h_0 = 1$ mm for the semi axes $R_{\mathrm{p1}} = 18$ mm and $R_{\mathrm{p2}} = 29$ mm (projection), and $R_{\mathrm{a1}} = 26$ mm and $R_{\mathrm{a2}} = 35$ mm (arc), respectively, along both major and minor axes.

linearly with the semi axis. The final values at the outflow are $484\,\mathrm{s}^{-1}$ at the outer major axis and $766\,\mathrm{s}^{-1}$ at the outer minor axis in the projection geometry and $747\,\mathrm{s}^{-1}$ at the outer major axis and $998\,\mathrm{s}^{-1}$ at the outer minor axis in the arc configuration. The form of the shear-stress distributions is the same as that of the shear rates. The shear stresses at the surface of the plates vary between 48 Pa and 100 Pa according to the equations (3.76) and (3.77), assuming a viscosity $\eta = 100$ mPas. These values are in the same order of magnitude as the result for the plane circular parallel plates.

The forces required to drive the plates of the given configurations together are 1.2 N for the axes $R_{\mathrm{p1}} = 18$ mm and $R_{\mathrm{p2}} = 29$ mm and 3.7 N for the axes $R_{\mathrm{a1}} = 26$ mm and $R_{\mathrm{a2}} = 35$ mm. The values for the corresponding circle radii are 1.3 N for 23 mm and 3.9 N for 30 mm. Analogously to the maximum pressures $p_{\mathrm{max}} - p_0$ this means that the required forces F are about 10% and 4% lower in the elliptic configuration than in the circular one.

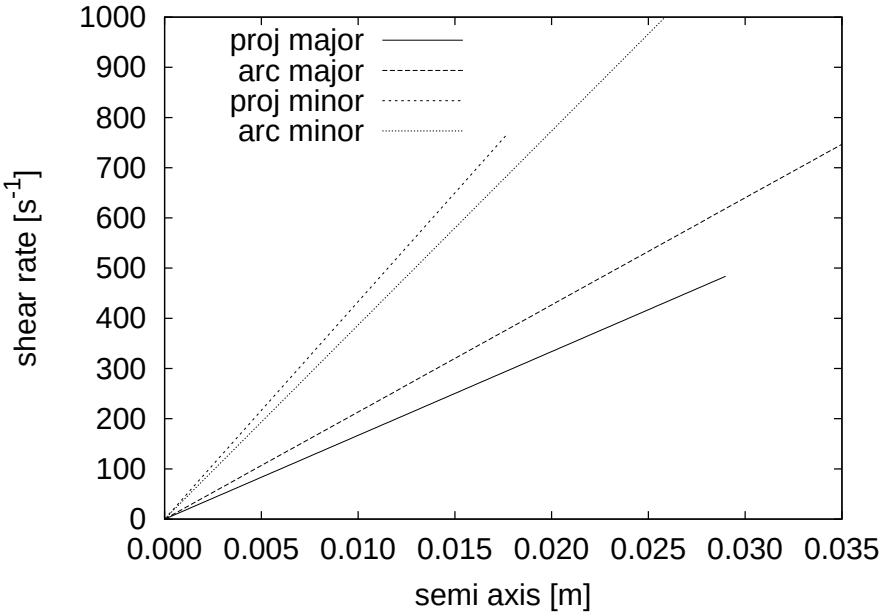

Figure 4.13: The absolute values of the shear rates $\frac{du_x}{dz}$ and $\frac{du_y}{dz}$ at the surfaces of the plane elliptic parallel plates according to equations (3.74) and (3.75) with $v_\mathrm{p} = 1$ cm/s and $h_0 = 1$ mm for the semi axes $R_{\mathrm{p}1} = 18$ mm and $R_{\mathrm{p}2} = 29$ mm (projection), and $R_{\mathrm{a}1} = 26$ mm and $R_{\mathrm{a}2} = 35$ mm (arc), respectively, along both major and minor axes.

Considering the equation

$$F = 3\pi \frac{\eta v_\mathrm{p}}{h_0^3} \frac{c_\mathrm{e}^3}{1 + c_\mathrm{e}^2} a^4, \tag{4.4}$$

which is an rearrangement of equation (3.80), it becomes clear that the force F that is required to drive the disks together is dependent on the ratio c_e of the axes assuming a constant semi-major axis a. Figure 4.14 shows this relationship. The force F increases from 1.2 N to 3.3 N for the projection configuration. In case of the arc configuration the increase is from 2.5 N to 7.1 N. The graphs reveal a decrease of 64% for the minimum ratio $c_\mathrm{e} = 0.62$ compared to the configuration of the plane circular parallel plates.

4.2.3 Plane and Curved Circular Parallel Plates

The analysis of the equations for a squeezing flow between the plane and curved circular parallel plates follows the example given with the STEFAN equation in section 4.2.1. In

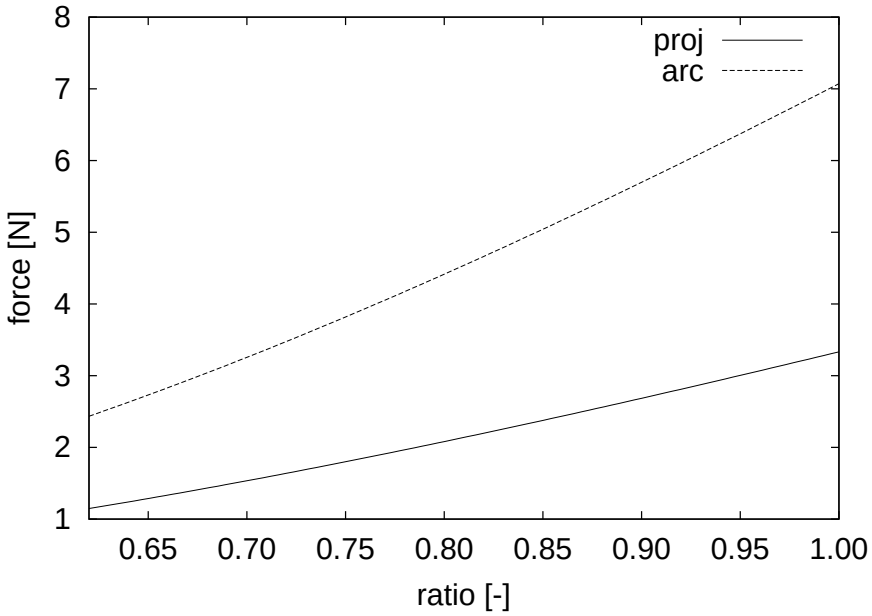

Figure 4.14: The external force F required to drive plane elliptic parallel plates together according to equation (4.4) in dependence on altering ratios c_e with $\eta = 100$ mPas, $v_\mathrm{p} = 1$ cm/s and $h_0 = 1$ mm for the semi-major axes $R_\mathrm{p2} = 29$ mm (projection) and $R_\mathrm{a2} = 35$ mm (arc), respectively.

order to show the pressure distribution $p - p_0$, the plate radius $R_\mathrm{p2} = 29$ mm is used. The dynamic viscosity is $\eta = 100$ mPas, the uniform plate velocity $v_\mathrm{p} = 1$ cm/s and the minimum film thickness $h_0 = 1$ mm.

The fluid film h at the boundary of the plate $r = R$ has the height $h_\mathrm{max} = 1$ cm, which is consistent with the height at the outflow of the numerical model. According to equation (3.81), the curvature parameter is quantifiable by the equation

$$\beta(R) = -\frac{\ln 10}{R^2}, \tag{4.5}$$

where R stands for the plate radius. Inserting $R_\mathrm{p2} = 29$ mm results in the shape of the upper plate that is shown in figure 4.15.

Figure 4.16 shows the pressure distribution $p - p_0$. Compared to figure 4.4, which represents the distribution between plane circular parallel plates, the shape of the curve has

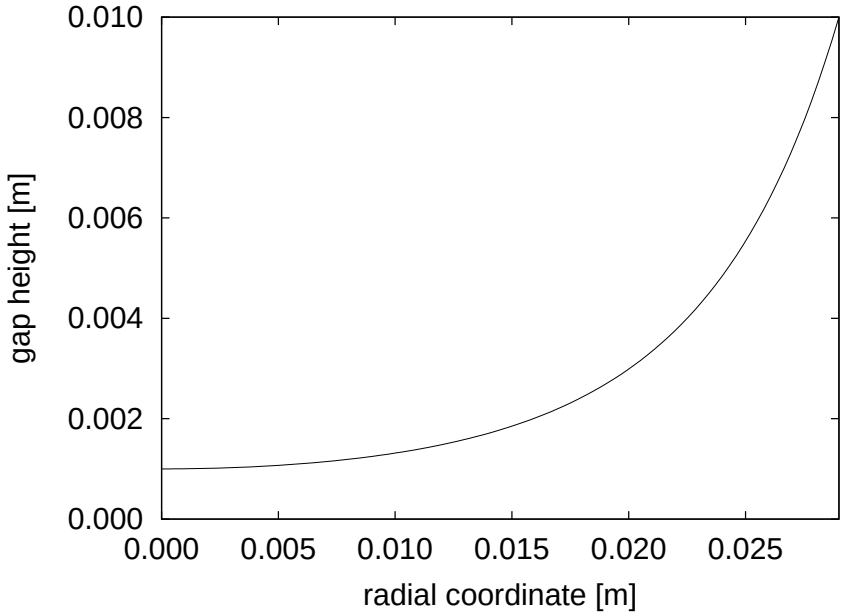

Figure 4.15: The shape of the upper curved plate based on the radius $R_{\mathrm{p2}} = 29$ mm with the initial heights $h_0 = 1$ mm in the middle of the plates and $h_{\max} = 1$ cm at the outflow.

changed. Additionally, the maximum pressure decreases from 2523 Pa to 365 Pa.

In order to make a more detailed statement about this decrease, the equation for the maximum pressure difference $p_{\max} - p_0$, which arises from equation (3.86), is analyzed. Setting the radial coordinate r to zero, as the highest pressure arises in the middle of the plates, and simplifying the equation gives approximately

$$p_{\max} - p_0 = \frac{1}{\ln 10} \frac{\eta v_{\mathrm{p}}}{h_0^3} R^2 \tag{4.6}$$

with $\beta(R)$ following the definition in equation (4.5). Figure 4.17 shows the result in the range of radii from 18 mm to 35 mm. The maximum pressure varies from 141 Pa for $R_{\mathrm{p1}} = 18$ mm to 532 Pa for $R_{\mathrm{a2}} = 35$ mm.

Comparing figure 4.17 with figure 4.5 reveals a constant difference of 86% of the maximum pressures along the outer radius R. Hence, increasing the film thickness h along the radial coordinate r will have an even bigger influence on the maximum pressures than the elliptic shape of the palate. For this reason, the effect must not be ignored.

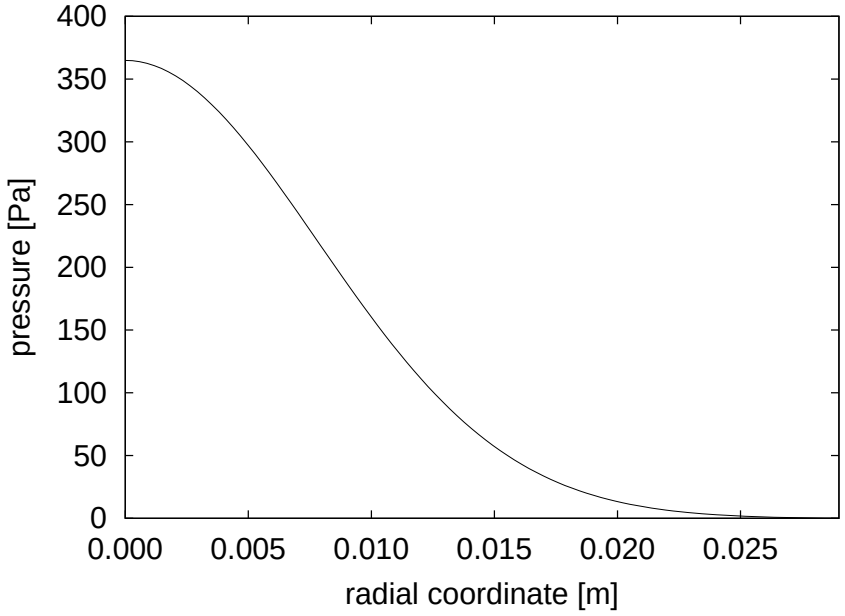

Figure 4.16: The pressure distribution $p-p_0$ between plane and curved circular parallel plates according to equation (3.86) with $\eta = 100$ mPas, $v_\mathrm{p} = 1$ cm/s, $h_0 = 1$ mm, $h_\mathrm{max} = 1$ cm and $R_\mathrm{p2} = 29$ mm.

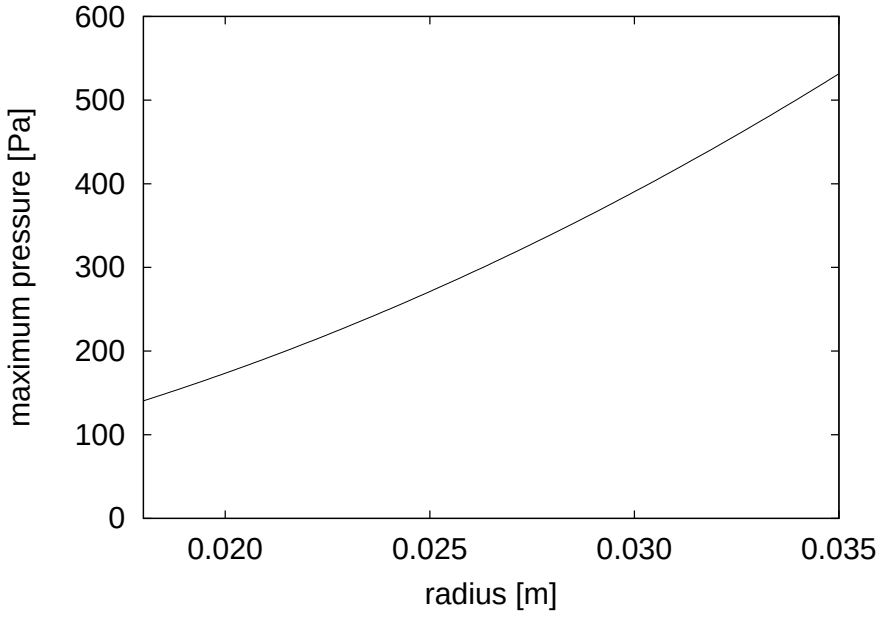

Figure 4.17: The maximum pressures $p_\mathrm{max} - p_0$ between plane and curved circular parallel plates as a function of the outer plate radius R according to equation (4.6) with $\eta = 100$ mPas, $v_\mathrm{p} = 1$ cm/s, $h_0 = 1$ mm and the respective height $h_\mathrm{max} = 1$ cm at the boundary of the plate.

Figure 4.18 shows the velocity distribution in the r-direction based on equation (3.92). The velocity at the outlet is 22 mm/s. In contrast to the previous calculations, the maximum velocity is not reached at the outlet. The maximum value of 61.5 mm/s can be found at $r = 13.5$ mm. From there on the height of the gap increases significantly and the pressure drops down. As the velocity distribution along the radial coordinate is quite different from the previous cases, a direct comparison is not possible. It can only be stated that the maximum occurring velocities drop to about a quarter of that compared with the geometry of two plane circular parallel plates. Figure 4.19 shows the velocity profiles in the gap for four different values of the radial coordinate r. The profiles are symmetric. The maximum values follow the distribution shown in figure 4.18.

Figure 4.20 shows the absolute values of the shear rate at the surfaces of the plates according to equation (3.94). The shear rate has its highest value $\frac{du}{dz} = 174\,\mathrm{s}^{-1}$ at $r = 9.6$ mm. This is only one fifth of the shear rate occurring at the outflow of the plane circular parallel plates. The maximum value of the occurring shear stress in a Newtonian medium with a viscosity $\eta = 100$ mPas is 17.4 Pa.

Figure 4.21 shows the force that is required to drive the plates together in dependence on different values of the plate radius R in the range from 18 mm to 35 mm. The forces range from 21 mN to 296 mN. Compared to the plane circular parallel plates the required force is 96% smaller.

4.2.4 Sphere in a Hemisphere

The calculation of a sphere in a hemisphere by means of equation (3.106) is based on the rounded-down radius through the key points in the sagittal plane $R_2 = 34$ mm, which is employed for the hemisphere. The minimum distance between the sphere and hemisphere in the z-direction adopts the same value occurring in the model of the numerical simulation, namely $h_0 = 1$ mm. This distance is normally maintained in the front part of the numerical model.

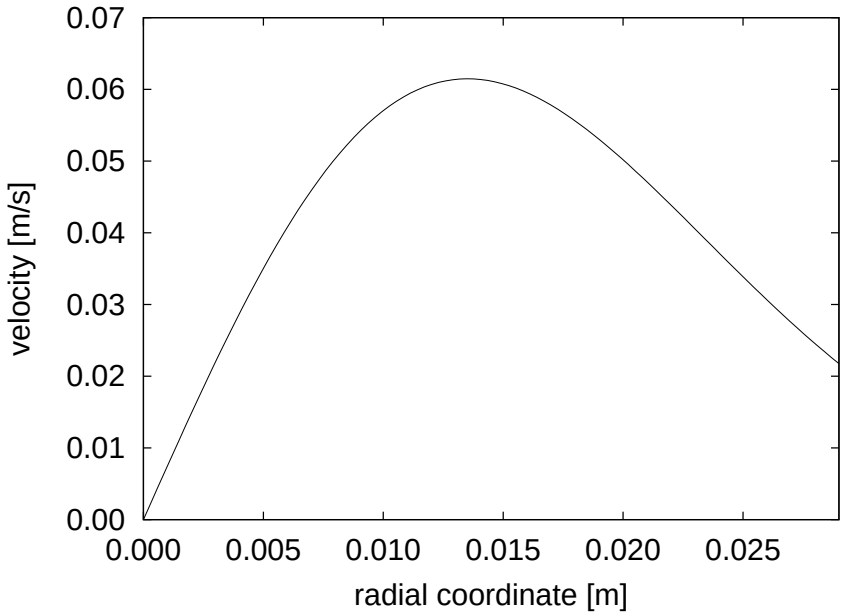

Figure 4.18: The velocity u_r in the middle of the gap at $z = 0.5 \cdot h_0 e^{-\beta r^2}$ between plane and curved circular parallel plates according to equation (3.92) with $\eta = 100$ mPas, $v_\mathrm{p} = 1$ cm/s, $h_0 = 1$ mm and $R_\mathrm{p2} = 29$ mm.

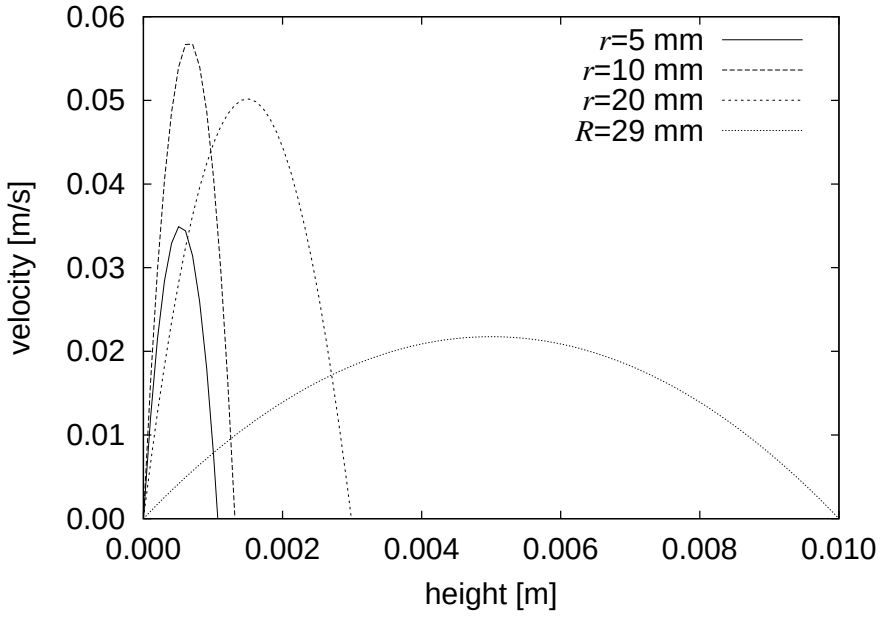

Figure 4.19: The velocity u_r along the height of the gap $h = h_0 e^{-\beta r^2}$ at different values of the radial coordinate r between plane and curved circular parallel plates according to equation (3.92) with $\eta = 100$ mPas, $v_\mathrm{p} = 1$ cm/s, $h_0 = 1$ mm and $R_\mathrm{p2} = 29$ mm.

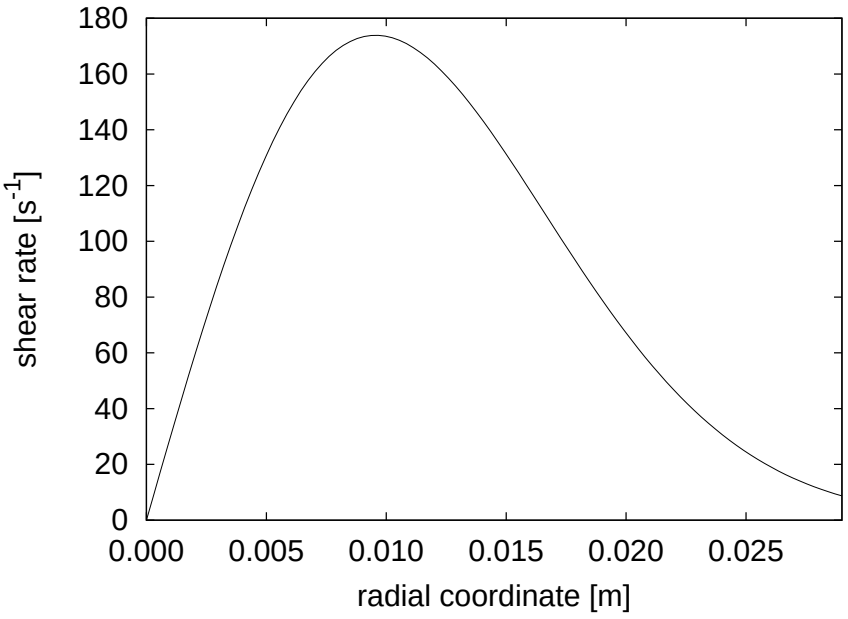

Figure 4.20: The absolute values of the shear rate $\frac{du_r}{dz}$ at the surfaces of the plane and curved circular parallel plates according to equation (3.94) with $v_\mathrm{p} = 1$ cm/s, $h_0 = 1$ mm and $R_{\mathrm{p}2} = 29$ mm.

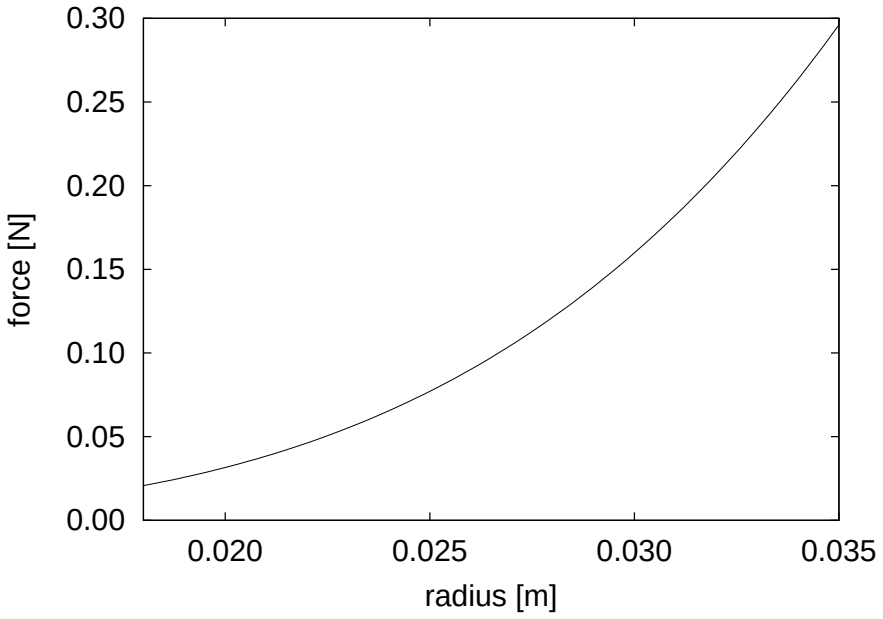

Figure 4.21: The external force F required to drive a plane and a curved circular parallel plates of different radii together according to equation (3.97) with $\eta = 100$ mPas, $v_\mathrm{p} = 1$ cm/s, $h_0 = 1$ mm and the respective height $h_\mathrm{max} = 1$ cm at the boundary of the plates.

In the rear part, the distance between the model tongue and the model palate increases. Strictly speaking, this should be mirrored by the horizontal distance between sphere and hemisphere starting from the key points $P_1(0\,\text{mm}|0\,\text{mm})$ and $P_2(58\,\text{mm}|0\,\text{mm})$ marked in figure B.1. For reasons of convenience, the radial clearance c is used instead. The previous approximations lead to the relation

$$e_z = c - 0.001\,\text{m} \tag{4.7}$$

for the eccentricity e_z.

In a first approach, clearances c in the range between 3.5 mm and 14 mm make sense. These values arise due to considerations according to the model of the numerical calculation. The lower boundary is explainable as follows. The film thickness h approaches zero in the front part of the model and 1 cm at the outflow. The distance of the ellipsoids in the rear part of the model is about 7 mm. These values can be understood as eccentricities. As eccentricities in the x- and y-directions are neglected in the model of a squeezing flow between a sphere and a hemisphere, the film thickness of 7 mm in the rear part of the model is split into a gap of 3.5 mm, which is maintained axi-symmetrically. The clearance $c = 14$ mm originates from the assumption that the film thickness 1 cm between the key points $P_1(0\,\text{mm}|0\,\text{mm})$ and $P_2(58\,\text{mm}|0\,\text{mm})$ and the sphere is upheld. However, as stated in section 3.3.6 an error E occurs in the height of the gap. With regard to equation (3.100), this error increases with an increasing clearance c. Figure 4.22 shows the result in the range of relevant clearances c. To employ a clearance of $c = 1$ cm, which is consistent with the previous analyses, requires accepting an error of 7.3%. In the following results it should be kept in mind that small discrepancies to reality can be expected due to the error in the modeled gap height. Accepting errors up to 10% allows to employ the clearance of $c = 1$ cm, which is consistent with the previous analyses.

In order to evaluate equation (3.106), the radial clearance adopts the maximum value $c = 1$ cm. Therewith, the eccentricity has the value $e_z = 9$ mm. Figure 4.23 shows the resulting profile of the gap.

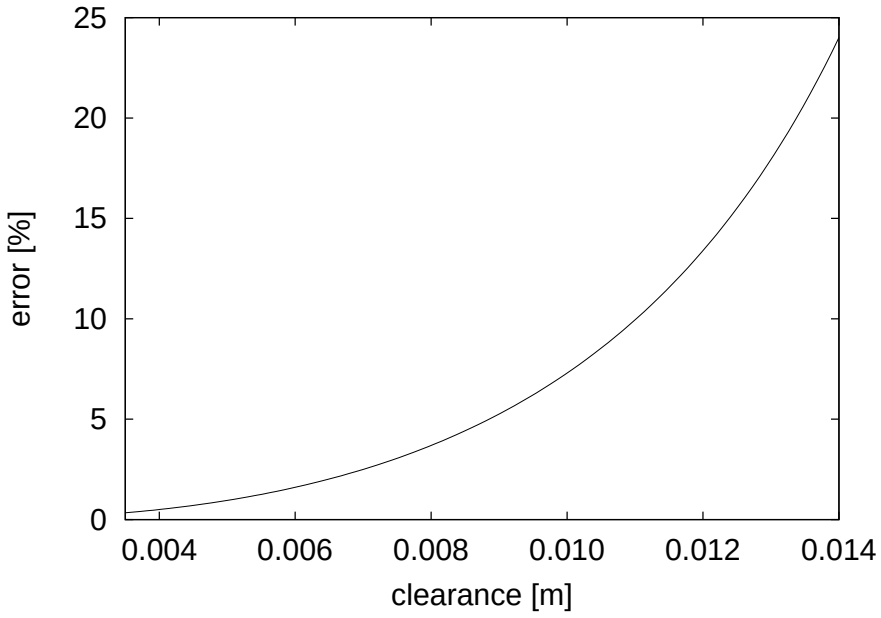

Figure 4.22: The percentage error E of the gap height that occurs between sphere and hemisphere in dependence on the radial clearance c according to equation (3.100) with $h_0 = 1$ mm and the constant radius $R_2 = 34$ mm of the hemisphere.

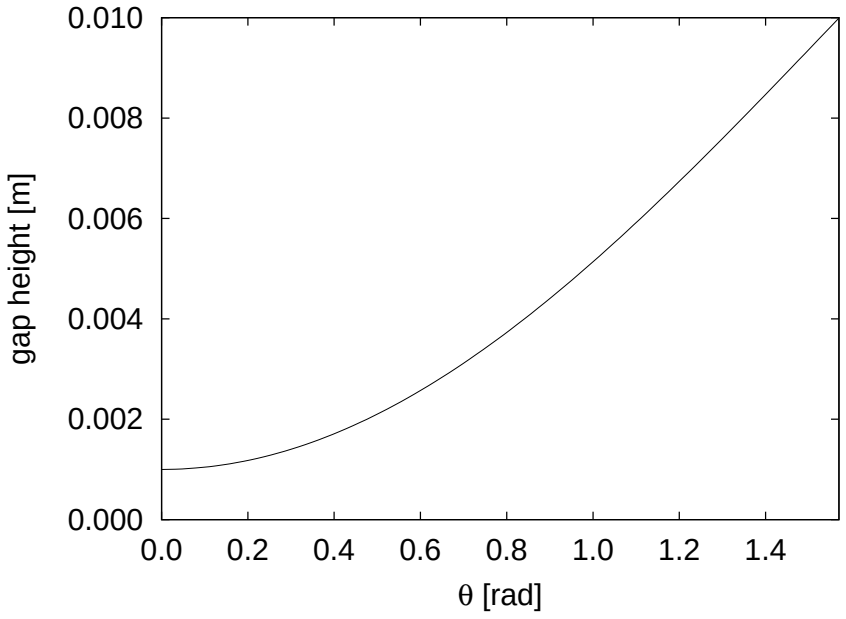

Figure 4.23: The profile of the gap between a sphere and a hemisphere based on the radius $R_2 = 34$ mm of the hemisphere with the initial height $h_0 = 1$ mm at the angle $\theta = 0°$, the clearance $c = 1$ cm and the eccentricity $e_z = 9$ mm.

Figure 4.24 shows the pressure distribution determined using these assumptions. The shape of the resulting pressure distribution is comparable with the one resulting from the arrangement of plane and curved circular parallel plates, although the peak is thinner. It reaches its maximum value for the angle $\theta = 0°$. Here, the pressure is 381 Pa. This is almost the same value that results from the configuration with the plane and curved circular parallel plates of radius $R_{\mathrm{p2}} = 29$ mm and a film thickness $h_{\max} = 1$ cm at the boundary of the plates.

The distribution of the maximum occurring pressures $p_{\max} - p_0$ requires further analysis. For this purpose, equation (3.106) is adapted. The maximum pressures arise at the angle $\theta = 0°$. The additional introduction of equation (4.7) yields

$$p_{\max} - p_0 = \frac{3R^2\eta v_{\mathrm{p}}}{c - 0.001\,\mathrm{m}} \left(1000000 \frac{1}{\mathrm{m}^2} - \frac{1}{c^2} \right) \tag{4.8}$$

for the maximum pressures.

In the first step, the radius of the hemisphere is kept constant $R_2 = 34$ mm. Figure 4.25 shows the result. The maximum pressure difference $p_{\max} - p_0$ decreases as the clearance c increases. While the pressure adopts the value 1274 Pa for the clearance $c = 3.5$ mm, it decreases to only 265 Pa for the clearance $c = 14$ mm.

Alternatively, the clearance $c = 1$ cm can be held constant, while the radius R is varied in the range between $R_1 = 18$ mm and $R_2 = 34$ mm. These radii belong to the circles, which pass through the key points in both the sagittal and the frontal plane of the averaged model of the oral cavity. The result is shown in figure 4.26. The arising pressure is 107 Pa for the radius $R_1 = 18$ mm. It increases to 381 Pa for the radius $R_1 = 34$ mm.

Compared to the results according to the STEFAN equation (3.30), the maximum pressures are smaller by about 90%. The values that come up due to the configuration of plane and curved circular parallel plates are approximately higher by 25%. Hence, the effect of the three-dimensional configuration is not negligible.

The velocity distribution according to equation (3.114) is shown in figure 4.27. Again,

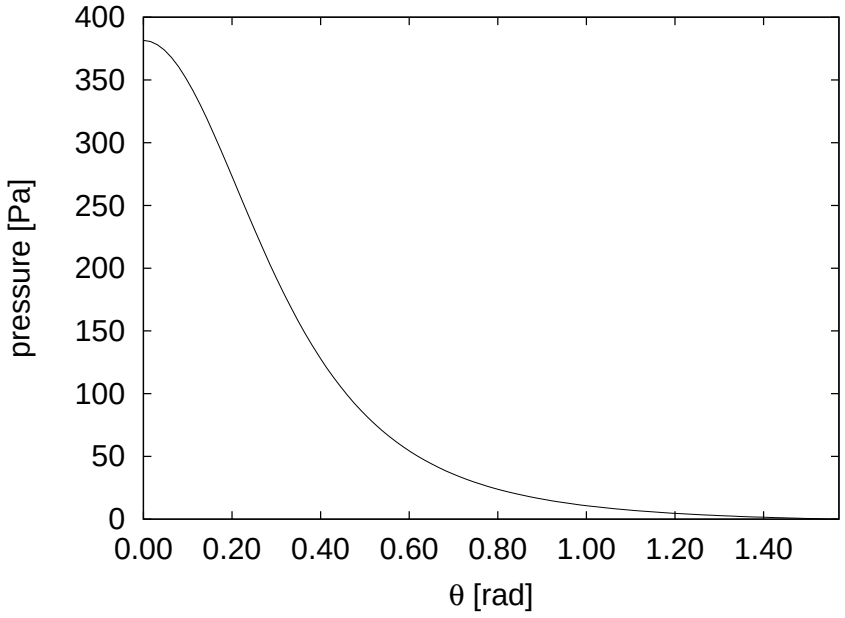

Figure 4.24: The pressure distribution $p - p_0$ between a sphere and a hemisphere according to equation (3.106) with $\eta = 100$ mPas, $v_\mathrm{p} = 1$ cm/s, $R_2 = 34$ mm, $h_0 = 1$ mm, $c = 1$ cm and $e = 9$ mm.

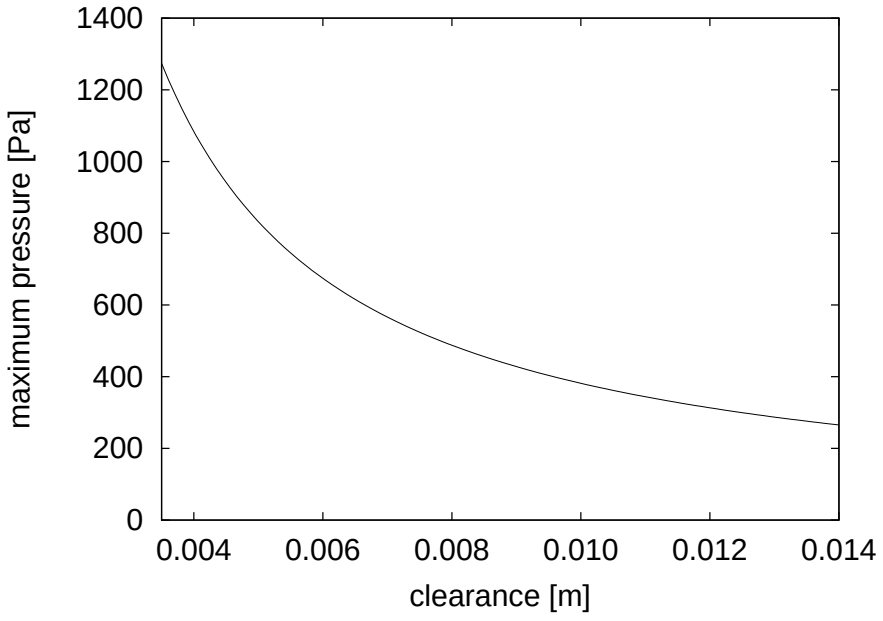

Figure 4.25: The maximum pressure $p_\mathrm{max} - p_0$ between a sphere and a hemisphere as a function of the radial clearance c according to equation (4.8) with $\eta = 100$ mPas, $v_\mathrm{p} = 1$ cm/s, $h_0 = 1$ mm and the constant radius $R_2 = 34$ mm of the hemisphere.

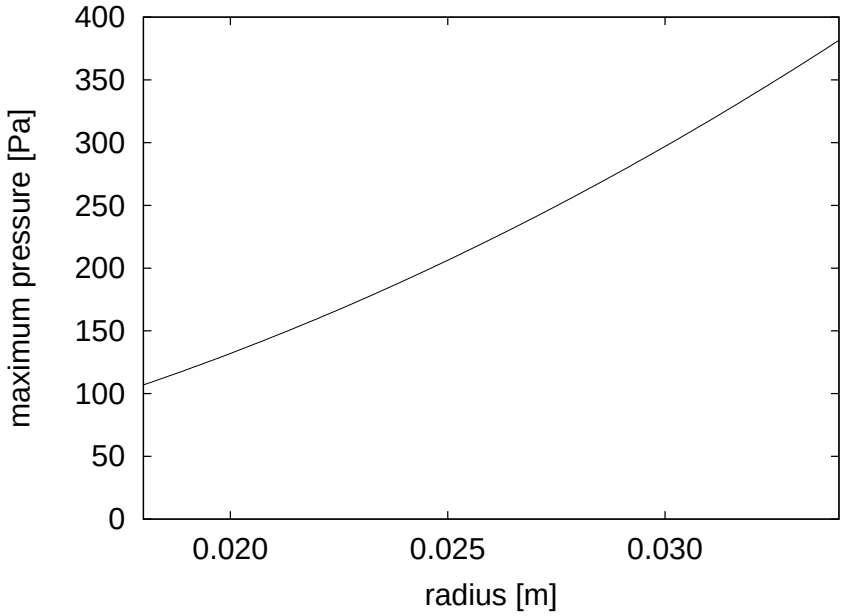

Figure 4.26: The maximum pressure $p_{\max} - p_0$ between a sphere and a hemisphere as a function of the radius R of the hemisphere according to equation (4.8) with $\eta = 100$ mPas, $v_{\mathrm{p}} = 1$ cm/s, $h_0 = 1$ mm and the constant clearance $c = 1$ cm.

the maximum velocity cannot be found at the outflow but at the angle $\theta = 26.4°$. Here, the velocity is 60 mm/s compared to 30 mm/s at the outflow. At this point, the gap height increases significantly again. The distribution is comparable to the one that occurs in the gap between the plane and curved circular parallel plates. The maximum value is reached after 30% along the arc, in the previous case the maximum value is reached after 40% of the radial coordinate of the plates. The values at these positions are almost the same. At the outflows, the velocity in the spherical geometry is slightly higher.

Figure 4.28 shows the absolute values of the velocity distribution in the gap. The distribution is not symmetric as the velocity of the sphere is not always perpendicular to the main fluid-flow direction. Hence, the curves show a small declination in the direction of the inner sphere.

The absolute values of the shear rates are shown in figure 4.29. The distributions reflect the asymmetry of equations (3.116) and (3.117). However, this asymmetry does not have a great effect on the results as figure 4.29 proves. The highest value is reached at 15° for

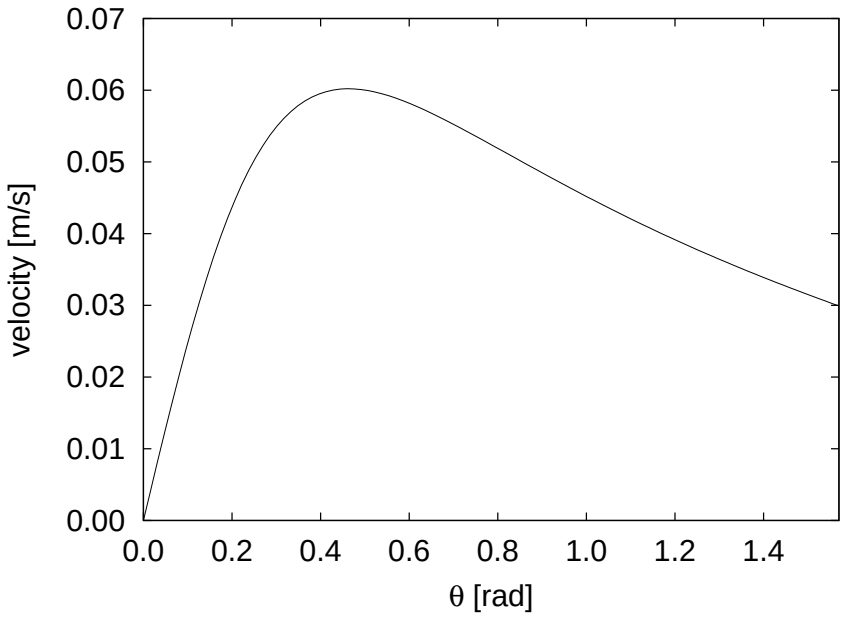

Figure 4.27: The velocity u_θ in the middle of the gap at $z = R - c + e_z \cos\theta$ between sphere and hemisphere according to equation (3.114) with $\eta = 100$ mPas, $v_\mathrm{p} = 1$ cm/s, $h_0 = 1$ mm and the constant clearance $c = 1$ cm.

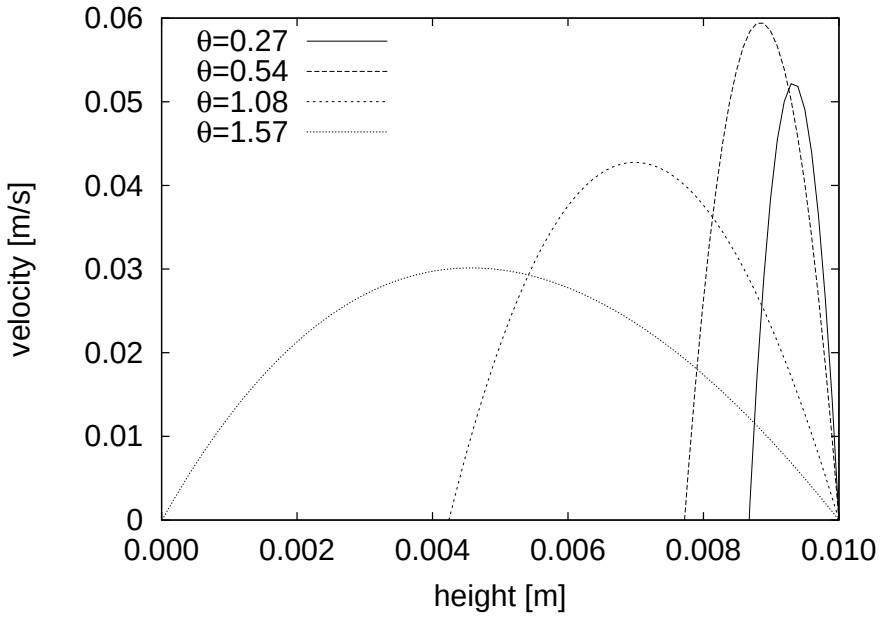

Figure 4.28: The velocity u_θ along the height of the gap $z = R - c + e_z \cos\theta$ at different angles θ between sphere and hemisphere according to equation (3.114) with $\eta = 100$ mPas, $v_\mathrm{p} = 1$ cm/s, $h_0 = 1$ mm and the constant clearance $c = 1$ cm.

both curves. The shear rate occurring at the sphere is $161\,\mathrm{s}^{-1}$, the one at the hemisphere is slightly smaller with $155\,\mathrm{s}^{-1}$. The shear rates at the outflow are $10\,\mathrm{s}^{-1}$ and $14\,\mathrm{s}^{-1}$. These shear rates are comparable to those arising in the configuration of plane and curved circular parallel plates. Therefore, the occurring shear stresses are also comparable.

The force F that is required to drive the sphere in the hemisphere is evaluated taking into consideration equation (3.120). Two approaches were employed. In the first one, the radius $R_2 = 34$ mm was kept constant while the clearance c varied. The result is shown in figure 4.30. The force F decreases with increasing clearances from 2.8 N to 0.3 N. Figure 4.31 shows the distribution for the constant clearance $c = 1$ cm for different values of the radius R. This reveals a range of forces F from 39 mN to 499 mN, which is about twice as big as in the configuration of a plane and curved circular parallel plate. Considering the bigger area of contact in the shell geometry it becomes clear why the force F can be bigger than in the geometry of a plane and curved parallel plate, although the maximum pressure is smaller.

4.2.5 Conclusion

The studies of the different geometrical models and parameters in the previous sections suggest two basic conclusions. The widely-used approach of Stefan yields a parabolic pressure distribution as well as linear functions for the velocity u_r and the shear rates and stresses along the radial coordinate. This approach does not model a changing fluid-film thickness h nor a three-dimensional curvature. In sections 4.2.3 and 4.2.4 these factors are taken into account, with the results showing significant changes. All of the physical quantities exhibit different distributions and have maximum values at different points of the geometries compared to the Stefan geometry. This shows that the three-dimensional nature of the real oral cavity cannot be neglected.

As well as showing different distributions, the values of the different quantities are smaller in all configurations than would be obtained following the approach of Stefan. The effect is quite small for the plane elliptic parallel plates but the other two set-ups exhibit large decreases in the different quantities. For this reason it is suggested that the geometry

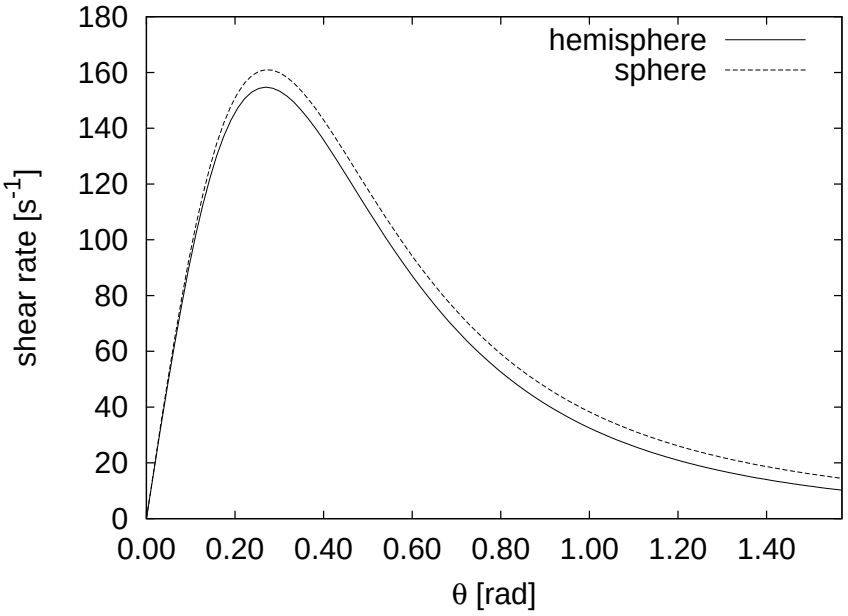

Figure 4.29: The absolute values of the shear rate $\frac{du_r}{dz}$ at the surfaces of the sphere and hemisphere according to equations (3.116) and (3.117) with $\eta = 100$ mPas, $v_\mathrm{p} = 1$ cm/s, $h_0 = 1$ mm and the constant clearance $c = 1$ cm.

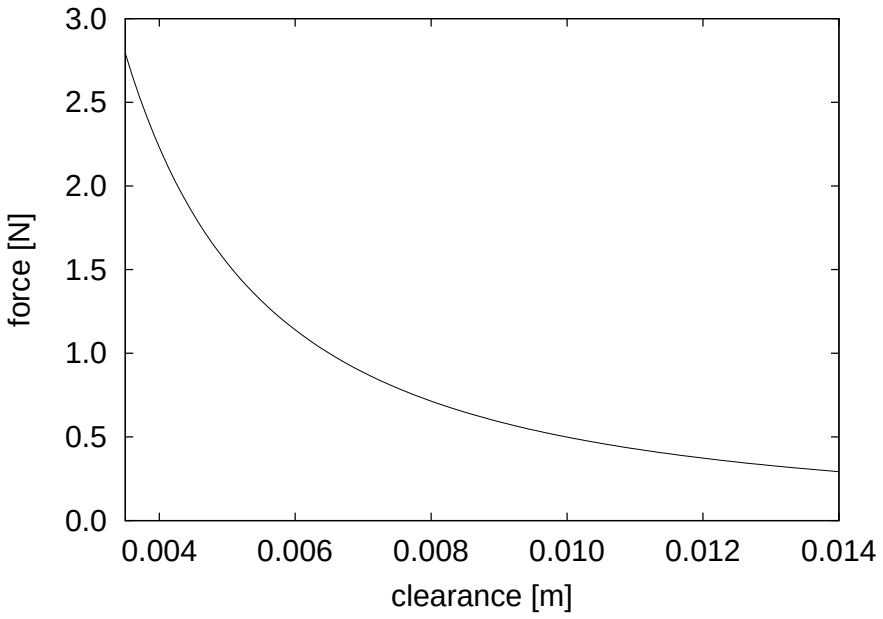

Figure 4.30: The external force F required to drive the sphere towards the hemisphere according to equation (3.120) with $\eta = 100$ mPas, $v_\mathrm{p} = 1$ cm/s, $h_0 = 1$ mm and the constant radius $R_2 = 34$ mm of the hemisphere.

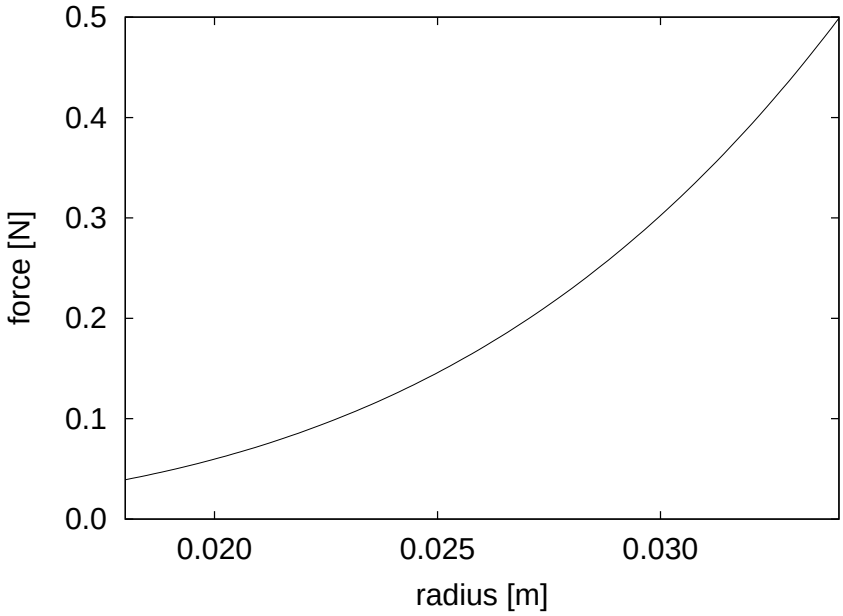

Figure 4.31: The external force F required to drive the sphere in the hemisphere according to equation (3.120) with $\eta = 100$ mPas, $v_\mathrm{p} = 1$ cm/s, $h_0 = 1$ mm and the constant clearance $c = 1$ cm.

of two plane circular parallel plates should be handled with care when employing it as a reference method for a squeezing flow in the oral cavity. It is advisable also to employ the other configurations, especially the one of the sphere driving into a hemisphere, in order to estimate the values of fluid-mechanical quantities in the mouth. This is significant in terms the human mechanoreceptors as it suggests that they must be even more sensitive than would be expected from the STEFAN model.

4.3 Numerical Simulations

The numerical simulations generate three-dimensional data of flow fields. Figure 4.32 shows the calculated pressure distribution for the cases N4 and CL from above. It is clear that the results are qualitatively similar. The pressure has the highest value at the tip of the model tongue in each case and decreases in the rear part of the model. Additionally, the isolines of pressure have a parabolic form in both cases.

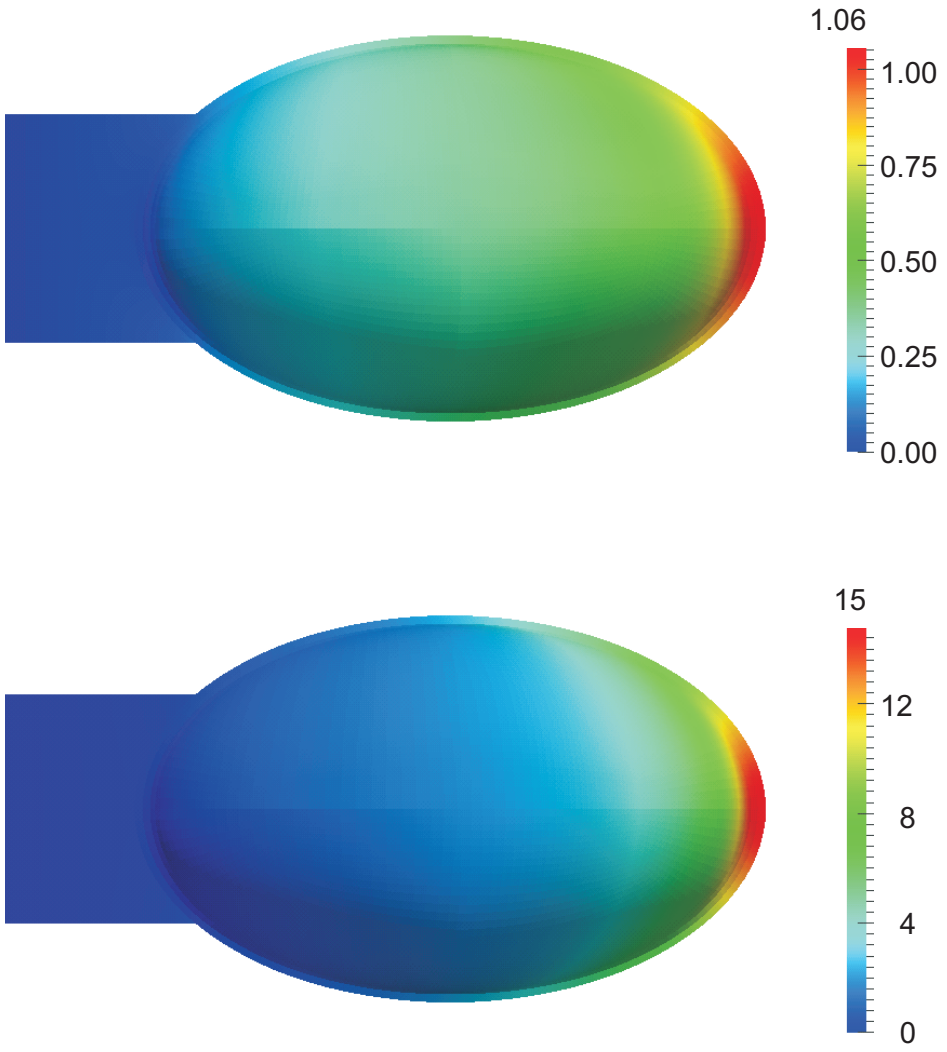

Figure 4.32: The top view of the pressure distributions in the cases N4 and CL.

The similarity of the form of the plots extends to all of the cases and properties considered. Therefore, only colored plots of one simulation case for each quantity are shown below. Due to the general nature of the plots, the color legend has been omitted in the color figures shown below.

Additionally, the models of the oral cavity are evaluated in two slices only. One slice lies in the sagittal plane, the other one in the frontal one. In both cases, slices that run perpendicular through the axis of the projected ellipse are chosen. These slices are chosen as they record the data that can reasonably be compared with the analytical solutions.

The results in these slices are evaluated on the basis of representative points in which the vector-field data are read out at the end of the simulation. One set of points lies directly at the surface of the movable model tongue. The other set is located in the middle of the bulk. Figure 4.33 shows this configuration exemplarily on the basis of the sagittal plane.

The origin of the x-axis is located at the outflow. The y-axis starts at the major axis of the projected ellipse. The evaluation in the sagittal plane only starts from $x = 0.03$ m as the radical changing of the geometry representing the pharynx causes abrupt changes in the flow-field data.

4.3.1 Pressures

Figure 4.34 gives a qualitative impression of the pressure distribution in the bulk between the movable model tongue and the fixed model palate. It is representative for all models used in the current study and is independent from the implemented rheological model and the related constants. The detailed evaluation with quantitative values takes place according to the representative points introduced above.

Figure 4.35 shows the pressure distribution in the middle of the bulk and at the surface of the model tongue in the sagittal plane using the example of case N4. This case was chosen for reference as the analytical calculations in section 4.2 are based on the same viscosity. The values occurring in the bulk and on the surface of the movable tongue do not alter significantly. This is consistent with the assumptions made for the analytical derivation in the theory of lubrication (section 3.3). As expected, the maximum pressures occur at the tip of the model tongue. The qualitative distribution indeed resembles the distributions that were found analytically in sections 4.2.3 and 4.2.4, which discuss squeezing flows between plane and curved circular parallel plates and a sphere in a hemisphere.

The pressure drops rapidly until reaching a plateau in the vicinity of the center of the projected ellipse. The level of this plateau lies at about half the maximum pressure for the low viscosity cases N1, N2 and N3. The higher the viscosity, the more abrupt the decline is before reaching the pressure plateau. In case N4, the pressure falls back to approximately

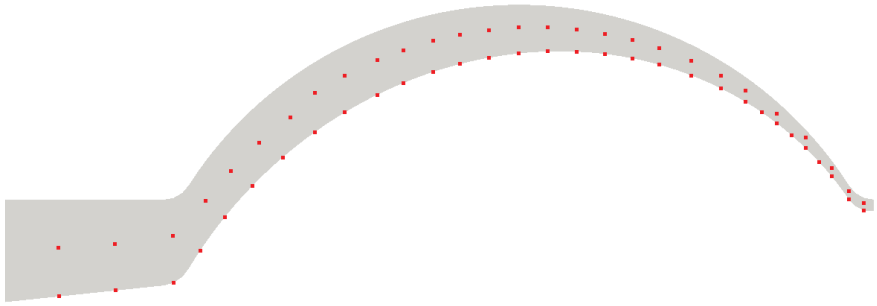

Figure 4.33: The slice in the sagittal plane including the representative points in the middle of the bulk and at the surface of the movable model tongue at the end of the simulations.

Figure 4.34: The qualitative pressure distribution in the bulk between the movable model tongue and the fixed model palate in the sagittal slice. The red color represents high and the blue color low pressures. The distribution exhibits the same characteristics for all of the considered fluids.

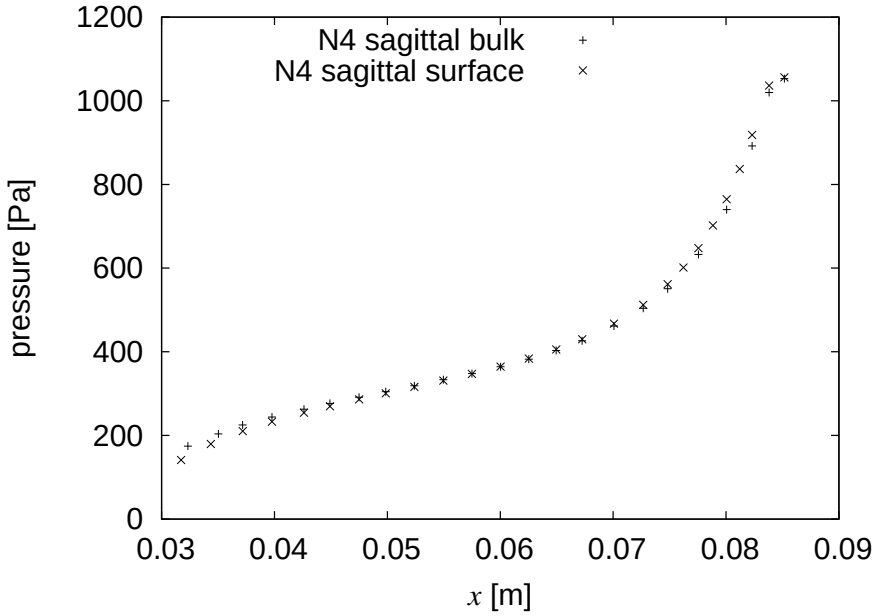

Figure 4.35: The representative pressure distribution in the middle of the bulk and at the surface of the model tongue in the sagittal plane along the x-axis, exemplarily shown by employing case N4.

one third of the maximum value. In case CL, the level of the pressure plateau lies only at about 15% of the maximum pressure. Getting closer to the outflow, the pressure further decreases until it reaches the value of the ambient pressure p_0 at $x = 0$ m.

The pressure in the frontal plane does not vary significantly for the small viscosities of cases N1, N2 and N3. For the higher viscosities of cases N4 and CL, the pressure in the middle of the geometry is lower than at the boundary of the geometry. Figure 4.36 shows this behavior for case N4 as an example. The qualitative distribution remains the same for all higher viscosity cases. The pressure difference in the frontal plane of case N4 makes up about 16% relative to the lower pressure in the middle of the geometry. In case CL it is as much as 25%.

The maximum pressures at the tip of the model tongue depend on the implemented rheological model and the related constants. Table 4.2 gives an overview. As expected by following the findings of the analytical calculations, the maximum pressures increase with fluid viscosity. The difference of the maximum pressures $p_{\max}$ is quite small when comparing

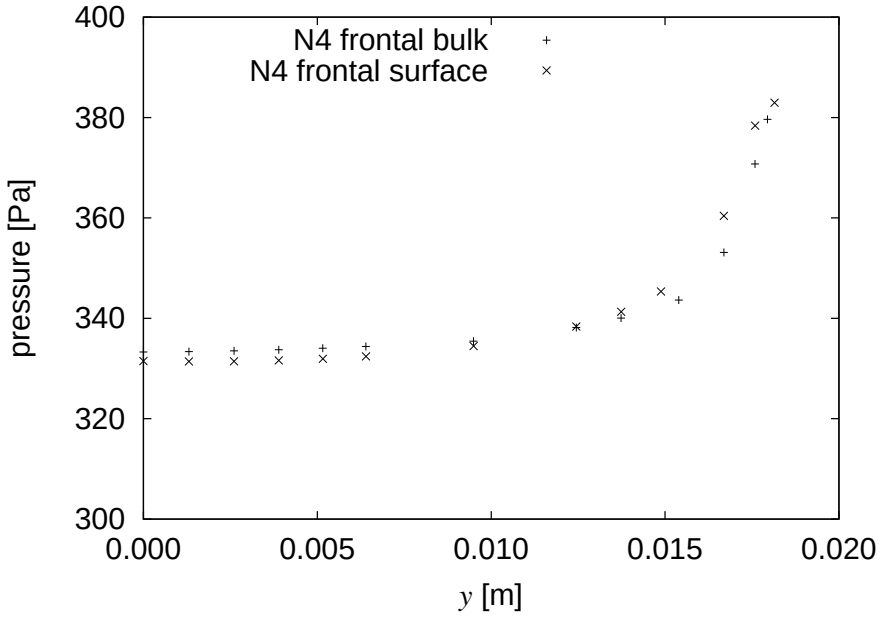

Figure 4.36: The representative pressure distribution in the middle of the bulk and at the surface of the model tongue in the frontal plane along the y-axis, exemplarily shown by employing case N4.

the model N1, representing water, with the models N2 and N3, in which the minimum and maximum viscosities appearing in beer are implemented. The differences add up to 16% and 60%, respectively.

The maximum pressures $p_{\max}$ of the models N4 with a hundredfold-higher viscosity than water and CL representing yogurt reach much higher values. The maximum pressure $p_{\max}$ is about 25 times higher in model N4 than in model N1. Considering case CL, the maximum pressure $p_{\max}$ is about 345 times higher than in the case of water.

The maximum occurring pressure $p_{\max}$ in case N4 is confirmed by the analytical calculation of a sphere in a hemisphere. This model comes closest to the model of the oral cavity, which is employed in the numerical simulations. The radius $R_2 = 34$ mm, which is employed for the hemisphere, is taken for granted as this is the radius that the dimension of the model oral cavity is based on with regard to the sagittal plane. This is the plane that the main direction of fluid flow takes place in.

The maximum value calculated by means of the numerical simulation is $p_{\max} = 1058$ Pa

Table 4.2: The maximum pressures $p_{\max}$ at the tip of the tongue in the model of the oral cavity.

Label	**Maximum pressure [Pa]**
N1	43
N2	50
N3	69
N4	1058
CL	14790

for $\eta = 100$ mPas. This value lies between the analytical calculated values with clearances of $c = 1$ cm, yielding $p_{\max} = 381$ Pa, and $c = 3.5$ mm, resulting in $p_{\max} = 1274$ Pa. Therefore, it is clear that the application of the analytical calculation of a sphere in a hemisphere is useful in order to estimate the resulting pressures in the model oral cavity.

As already mentioned previously in section 3.4.5, Zürcher & Kursawe (1973) state that a beer drinker is able to distinguish between the similar viscosities represented by cases N1 to N3. The question arises which parameter causes this differentiated perception. The pressure-induced deformation is probably out of the question. The sensitivity of oral SA-I mechanoreceptors discussed in section 2.2.2 is 120 Pa. The value was determined by Semmes-Weinstein monofilaments. Hence, a Newtonian fluid would need a viscosity of approximately 0.01 Pas to be sensed, assuming a linear relationship between viscosity and maximum pressure. Beer would definitely be below the necessary threshold.

Indeed, Semmes-Weinstein monofilaments cause a point load while food in the mouth causes a distributed load. Maybe, the simultaneous stimulation of several receptive fields enable the enhanced sensitivity. Additionally, there is no statement about the sensitivity of the other two types of mechanoreceptors occurring in the oral cavity. A crucial involvement of the kinesthetic sense in the evaluation process of food thickness is worth consideration.

The values calculated by employing both analytical methods and computational fluid dynamics agree with the values of the pharyngeal pressure arising during swallowing that were reported by Kim, McCulloch & Rim (2000). These authors found values in the range from 1.3 kPa to 7.3 kPa. In their study, the displacement of the internal lumen of

the pharynx was determined by means of a finite element simulation of the pharynx. The arising pressure in the swallowed bolus was equalized with the pressure that is necessary to counterbalance the external load on the pharyngeal wall.

Only recently, Kieser, Singh, Swain, Ichim, Waddell, Kennedy, Foster & Livingstone (2008) published pressures measured *in vivo* in the oral cavity. Five subjects were asked to swallow 10 ml of water. Eight miniature pressure transducers recorded the intraoral pressures. Figure 4.37 shows their positions. The data transferred *via* the channels 4 to 8 are most relevant for comparison with the calculated values due to their location in the mouth. Table 4.3 gives an overview of the range of recorded pressures in dependence on the positions of the pressure transducers. The large differences occurring can be ascribed to the individual swallowing characteristics of the subjects.

These values range from 13.05 kPa to 289.75 kPa and by far exceed the simulated values. In contrast to the simulations, the pressures increase with a decreasing distance to the pharynx. These results might be traced back to the fact that the simulation in the current study works with a stiff model tongue. This approach poorly imitates the dynamic movements of the real muscular hydrostat. Nevertheless, the application of the numerical simulations is vindicated as it generates additional knowledge about single parameters of the flow field, which cannot be determined by measuring pressures only.

Table 4.3: The ranges of pressures measured during in vivo water swallows in five subjects.

Channel	**Name**	**Pressure range [kPa]**
4	palatal molar	13.05–26.82
5	palatal canine	24.23–49.29
6	palatal central	22.49–98.30
7	mid palate	24.57–122.03
8	posterior palate	30.93–289.75

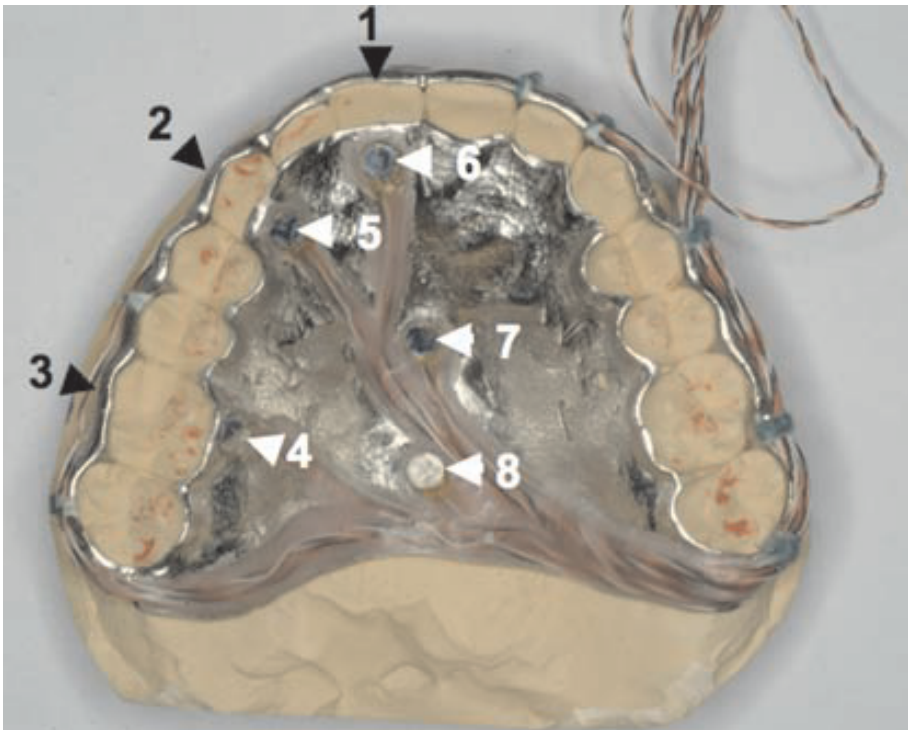

Figure 4.37: The position of the eight miniature pressure transducers used by KIESER ET AL. (2008).

4.3.2 Velocities

Figures 4.38 and 4.39 show the representative qualitative distributions of the magnitude of velocity in the sagittal and frontal slice. As expected, the velocities in the bulk are higher than those at the surfaces of the model oral cavity. Again, the data are evaluated quantitatively on the basis of the selected points in both slices. Although the multicolored qualitative distributions suggest that the different fluids behave similarly, closer attention reveals essential differences.

The qualitative distribution of the magnitude of velocity in the bulk is similar for all cases in the sagittal plane. Figure 4.40 shows these distributions. The magnitude of velocity is small at the tip of the model tongue and increases in the direction of the rear part. This increase takes place quite fast in the beginning, shows a plateau in the middle region of the model tongue, and further increases until it reaches its maximum value shortly before

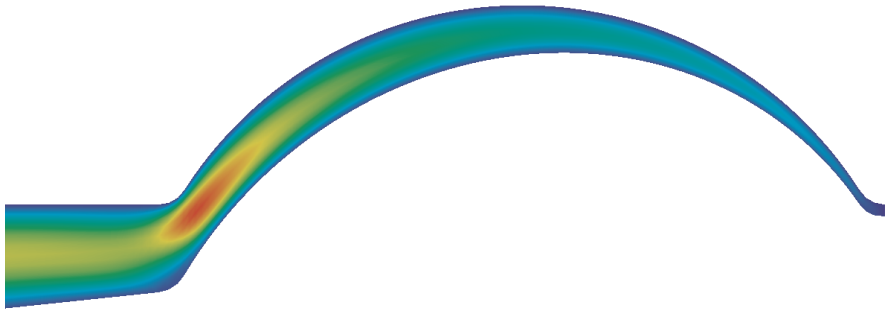

Figure 4.38: The qualitative distribution of the magnitude of velocity in the bulk between the movable model tongue and the fixed model palate in the sagittal slice. The red color represents high and the blue color low magnitudes of velocity. The distribution exhibits the same characteristics for all of the considered fluids.

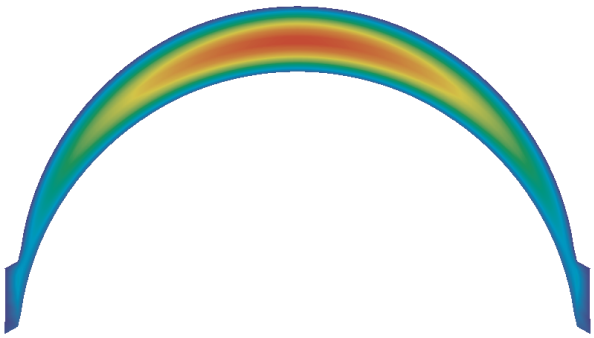

Figure 4.39: The qualitative distribution of the magnitude of velocity in the bulk between the movable model tongue and the fixed model palate in the frontal slice. The red color represents high and the blue color low magnitudes of velocity. The distribution exhibits the same characteristics for all of the considered fluids.

the geometry narrows into the model pharynx. The distribution shape of the magnitude of velocity is thereby mirrored against the shape of the pressure distribution. This behavior conforms with the well-known BERNOULLI equation

$$\frac{u^2}{2} + gz + \frac{p}{\rho} = \text{constant}, \tag{4.9}$$

which is based on the assumption of an inviscid flow (SPURK & AKSEL, 2007).

The distribution is different from the one found in the analytical calculation of velocities in the gap between a sphere and hemisphere. This observation can be explained by the different characteristics of the geometries of the models. While the geometry used in the analytical calculation opens out, the geometry of the numerical model narrows to the model pharynx. For that reason, the velocity must increase here, while it drops down for the analytical model. Nevertheless, the order of magnitude is the same.

Table 4.4 gives an overview of the maximum values of the velocity magnitude arising in the rear part of the model oral cavity. Comparison shows that the magnitude of velocity increases slightly with an increasing viscosity ν in the Newtonian cases N1 to N4. On the contrary, the velocity in the non-Newtonian fluid implemented in case CL exhibits the same value as water.

Another peculiarity in the non-Newtonian case CL attracts attention. Contrary to the Newtonian cases, the magnitude of velocity at the surface of the model tongue does not agree with the maximum velocity of the movement at the tip of the model tongue along

Table 4.4: The maximum magnitudes of velocity $u_{\text{mag,max}}$ occurring in the model of the oral cavity at the rear part of the tongue.

Label	**Maximum magnitude of velocity [m/s]**
N1	0.15
N2	0.15
N3	0.16
N4	0.22
CL	0.15

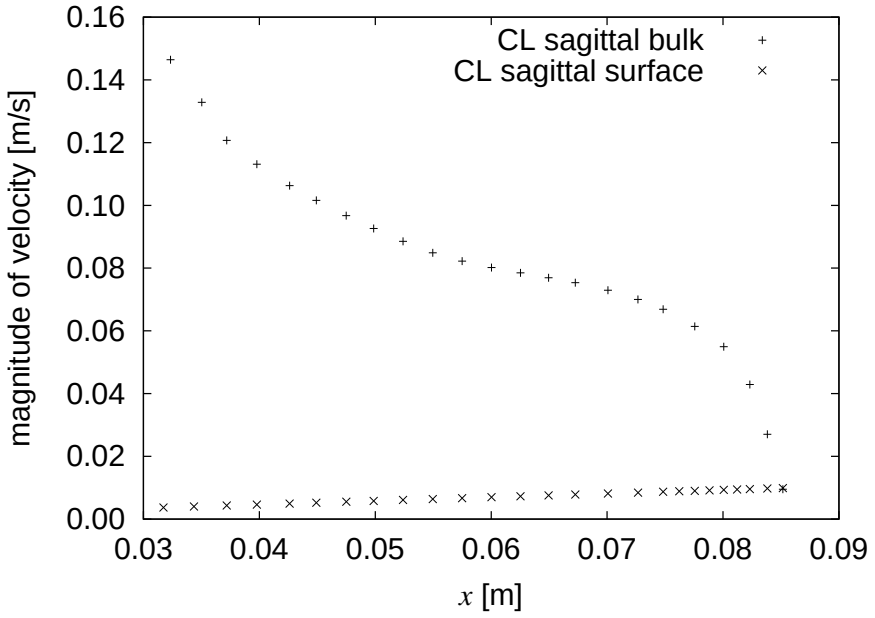

Figure 4.40: The distribution of the magnitude of velocity in the middle of the bulk and at the surface of the model tongue in the sagittal plane along the x-axis, using case CL as an example.

the complete x-axis, as can be seen in figure 4.40. Instead, it decreases with the linearly decreasing velocities of the movable model tongue along the x-axis. This behavior can be explained by the high viscosities of the implemented flow curve at low shear rates. The fluid only begins to deform significantly beyond a certain stress level. Obviously, this leads to the previously described behavior that the fluid responds completely to the imposed deformation.

The observation that the velocities increase with increasing viscosities in Newtonian media needs further clarification. The flow becomes more sluggish the more viscous the medium is. This behavior accompanies lower flow velocities. At first glance, this expectation conflicts with the observation in the numerical simulations of increasing fluid-flow velocities.

In any account, the volume flow rate in each model must be constant independent of the implemented viscosity, since the volume flow rate is solely determined by the movement of the model tongue. The equation

$$\dot{V} = \frac{dV}{dt} = u \cdot A \tag{4.10}$$

describing the volume flow rate is based on the assumption that the streaming velocity u is constant in the cross section. Figure 4.39 shows qualitatively that the velocity field does not exhibit this constancy. In order to fulfill the required condition, the averaged velocity of the entire flow field needs to be equal.

The diversification of the fluid-flow velocities within a cross section is not an issue as long as the averaged velocity is the same. Figure 4.41 reveals that the flow profiles are very different depending on the viscosity of the system. The low viscosity fluid in case N1 features the maximum velocity in the majority of the flow-field points. On the contrary, the maximum velocity of fluid flow is achieved only in a very small section of the geometry considering the high viscosity fluid in case N4. In return, the maximum occurring velocity is higher compared to the maximum velocity arising in low viscosity fluids. Consequently, it can be stated more precisely that the maximum velocity increases with an increasing viscosity of a fluid, while the averaged velocity remains constant.

Getting back to the starting point of a higher viscosity yielding a bigger inertia it can be stated that the velocity of the movement of the tongue is better transferred by low viscosity fluids. Here, the viscosity level is more constant over a wider range. Higher viscosity fluids react inertly to applied movements, as can be seen in the profile of velocities in the frontal slice. The maximum velocity only forms right in the core of the flow profile.

Dantas, Kern, Massey, Dodds, Kahrilas, Brasseur, Cook & Lang (1990) and Takahashi, Nitou, Tayama, Kawano & Ogoshi (2002) both investigated the bolus behavior during deglutition in the pharynx by means of videofluoroscopy and manometry. They found a delay of the bolus transit with higher viscosities. Their results do not disagree with the findings of the current study as the bolus transit separate from its active support by pharyngeal peristaltic waves is more comparable to a pipe flow than to a squeezing flow. In addition, the pharyngeal peristaltic waves are not normalized to one specific speed of movement as is the case for the movement of the tongue in the model of the oral cavity. Hence, the volume flow rate is not necessarily constant.

The literature also permits a quantitative comparison of fluid-flow velocities in the phar-

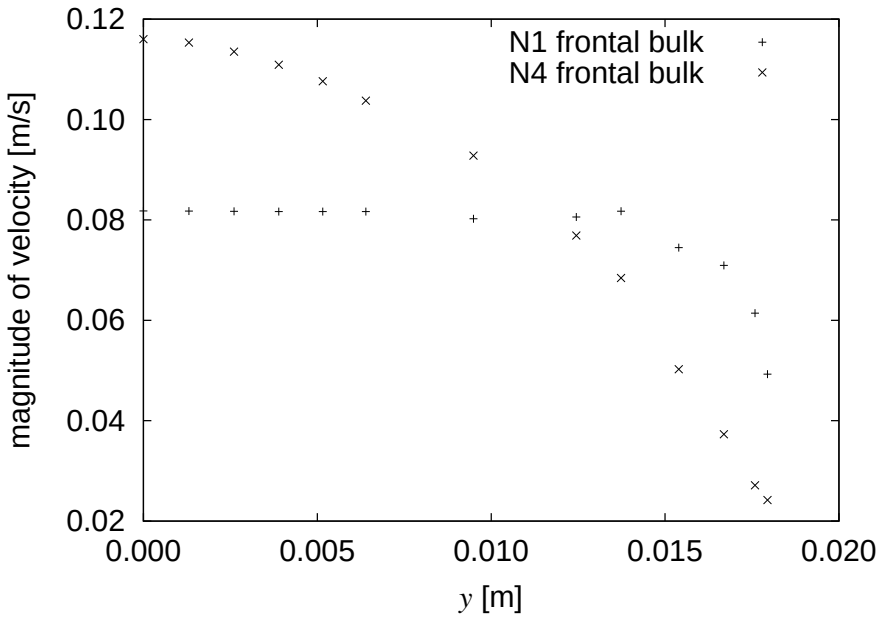

Figure 4.41: The distribution of the magnitude of velocity in the middle of the bulk in the frontal plane along the y-axis in the cases N1 and N4.

ynx. Hasegawa, Otoguro, Kumagai & Nakazawa (2005) measured the velocity spectrum in the bolus by means of the ultrasonic pulse Doppler method. The velocity of all food samples averages out at 0.1 m/s. The maximum velocity of water was 0.5 m/s and 0.2 m/s for yogurt. Miquelin, Braga, Dantas, Oliveira & Baffa (2001) investigated the pharyngeal bolus flow with regard to the pharyngeal transit time. The samples consisted of 10 ml yogurt and 5 g manganese ferrite. The authors observed an average value of 0.75 s. Based on these findings, Chen (2009) calculates a flow speed of about 5 cm/s assuming a pharyngeal cross-section diameter of 2 cm. These results agree fairly well with the results of the numerical simulations presented here.

4.3.3 Shear Rates

Figure 4.42 shows the representative qualitative distribution of the magnitude of the velocity gradient in the sagittal slice. Generally, the shear rates are higher closer to the surface. The lowest shear rates occur in the middle of the bulk. Furthermore, the shear rates near the

surface tend to increase from the tip of the model tongue to the rear part.

Figure 4.43 shows the distribution of the shear rates in the bulk and at the surface of the model tongue for the Newtonian fluid N4. Regarding the shear rates at the surface of the model tongue, an increase from about $20\,\mathrm{s}^{-1}$ at the tip of the model tongue to approximately $150\,\mathrm{s}^{-1}$ in the rear part of the model can be observed. The lower viscous fluids of cases N1, N2 and N3 have comparable shear rates. Only the distributions along the x-axis change slightly. The analytical calculations of the shear rates in the sphere-hemisphere configuration exhibit comparable values. The distribution is necessarily different due to the different velocity distribution discussed in the previous section.

The shear rate range in the bulk is smaller than at the surface of the model tongue. Figure 4.43 reveals values between $14\,\mathrm{s}^{-1}$ and $28\,\mathrm{s}^{-1}$, assuming that the higher value at the tip of the model tongue is an outlier. The values are distributed slightly curved with the smallest values in the center of the geometry. At the tip of the tongue, the shear rate curves of bulk and surface converge. The same observation can be made for the cases N1 to N3. However, the occurring shear rates range from $5\,\mathrm{s}^{-1}$ and $27\,\mathrm{s}^{-1}$. While the upper value is almost the same for all models, the lower value is only about one third of the value arising in the higher viscous medium.

The non-Newtonian fluid shows a slightly different behavior. Figure 4.44 reveals these differences. Concerning the shear rates at the surface, the level is lower by one third in the rear part of the model oral cavity compared to case N4. The curves intersect at about $x = 0.005$ m. For large values of x, the curve representing the Newtonian fluid further decreases while the curve representing the non-Newtonian fluid slightly increases again. The shear rate range covers values from $46\,\mathrm{s}^{-1}$ to $103\,\mathrm{s}^{-1}$.

The qualitative distribution of shear rates in the bulk is comparable to case N4. However, the values are about 60% lower compared to the Newtonian case N4. The values are in the region of $8\,\mathrm{s}^{-1}$. Unlike the curves of Newtonian behavior, the curves of shear rates at the surface of the model tongue and in the bulk do not intersect at the tip of the tongue but scatter.

Figure 4.42: The qualitative distribution of the gradient of the magnitude of velocity in the bulk between the movable model tongue and the fixed model palate in the sagittal slice. The red color represents high and the blue color low gradients of the velocity magnitude. The distribution exhibits the same characteristics for all of the considered fluids.

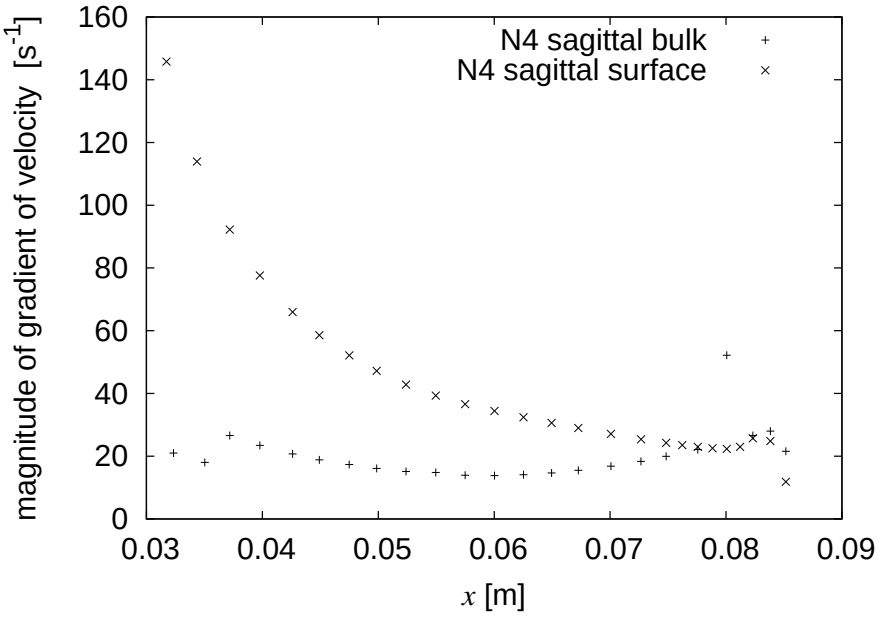

Figure 4.43: The distribution of the magnitude of the gradient of velocity in the middle of the bulk and at the surface of the model tongue in the sagittal plane along the x-axis, for Newtonian fluids using case N4 as an example.

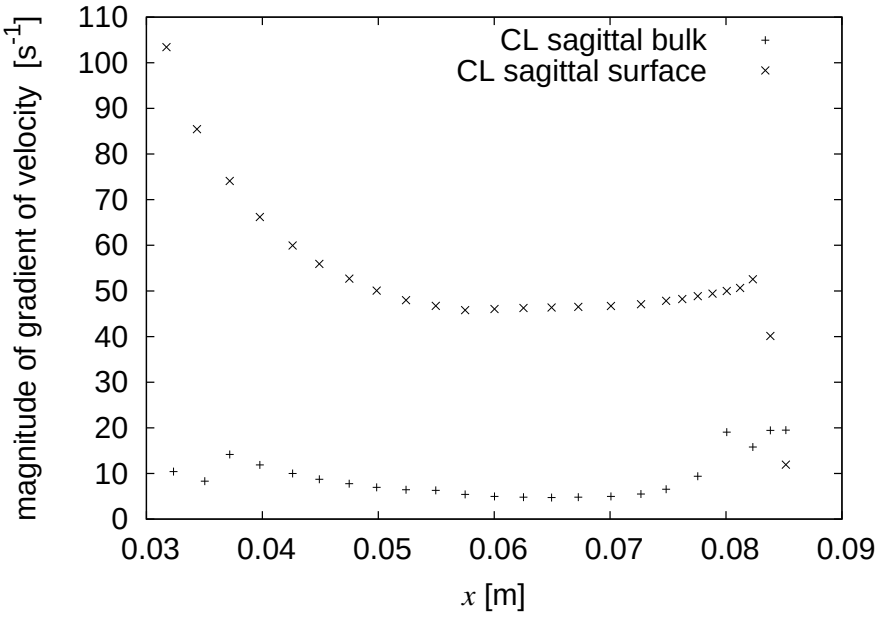

Figure 4.44: The distribution of the magnitude of the gradient of velocity in the middle of the bulk and at the surface of the model tongue in the sagittal plane along the x-axis for the non-Newtonian fluid in case CL.

Figure 4.45 shows the representative spacial distribution in the frontal slice. Here, it can clearly be seen that the layer of highest shear rates is not located directly at the surface of the model tongue but just above it. Hence, the highest shear rates are not evaluated by the given representative points at the surface and in the middle of the bulk. As the shear rates found directly at the surface of the model tongue affect the mechanoreceptors, these values are more important despite being lower.

Regarding the frontal slice, the behavior of the thin fluids can be compared, as well as the behavior of the thicker ones, with the comparisons showing that their behavior is independent of the rheological characterization. In the low-viscosity fluids, the shear rate values increase slightly with an increasing distance from the center and increase significantly at the boundary. Figure 4.46 shows the distribution.

The shear-rate differences at the middle of the surface are small. They only increase by about $2\,\mathrm{s}^{-1}$ each with respect to water, which exhibits a value of $26\,\mathrm{s}^{-1}$. At the boundary of the geometry, the difference is significant. While a shear rate of $151\,\mathrm{s}^{-1}$ can be found for

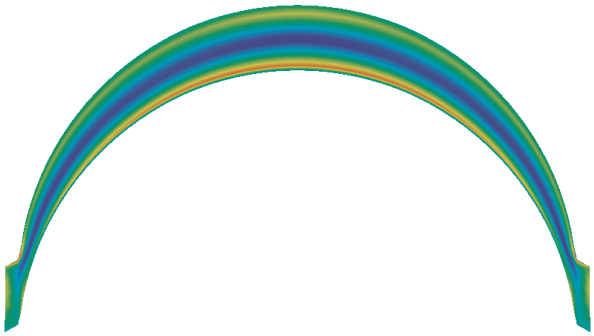

Figure 4.45: The qualitative distribution of the gradient of the magnitude of velocity in the bulk between the movable model tongue and the fixed model palate in the sagittal slice. The red color represents high and the blue color low gradients of the magnitude of velocity. The distribution exhibits the same characteristics for all of the considered fluids.

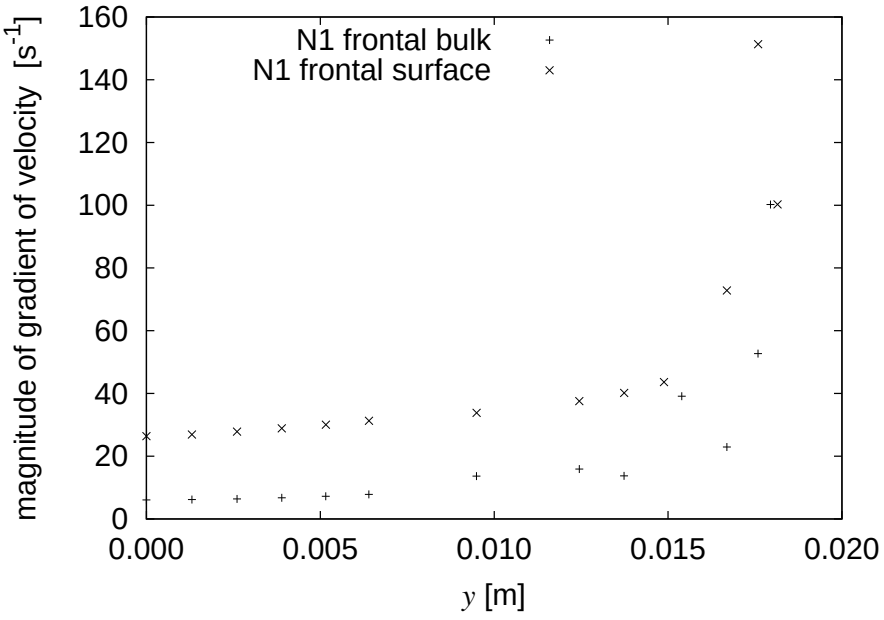

Figure 4.46: The distribution of the magnitude of the gradient of velocity in the middle of the bulk and at the surface of the model tongue in the frontal plane along the y-axis, for low-viscosity fluids using case N1 as an example.

case N1, cases N2 and N3 only feature shear rates of $133\,s^{-1}$ and $108\,s^{-1}$, respectively. This makes up a decrease of 12% and 28%. A similar behavior can be observed for the shear rates in the bulk. In the center of the geometry, the shear rates of each model are smaller than $10\,s^{-1}$. Case N1 shows a shear rate of $100\,s^{-1}$ at the boundary of the geometry. The shear rates of the cases N2 and N3 decrease by 10% and 25%.

In the higher viscosity fluids, the curves increase a bit initially and then slightly drop a greater distance away from the center. Only at the boundary, do they increase again. Figure 4.47 shows the distribution based on case CL.

The values range from $29\,s^{-1}$ to $66\,s^{-1}$ in case N4. The shear rate that occurs in the center of the geometry is $39\,s^{-1}$. In case CL, the corresponding values are $34\,s^{-1}$, $67\,s^{-1}$ and $47\,s^{-1}$. Thus, the values at the boundary are nearly the same, while the shear rates in the middle of the geometry and the lowest shear rates increase with an increasing viscosity. Hence, the resulting shear-rate range reduces as the viscosity increases.

The shear rates occurring in the bulk are almost constant. They scatter around $15\,s^{-1}$ in case N4 and around $7\,s^{-1}$ in case CL. At the boundary, they increase approximately threefold. In contrast to the values at the surface, the values of the Newtonian case are higher here.

The shear rates at the surface of the model tongue are supposed to be most important for mouthfeel sensations. These shear rates have a direct effect on the mechanoreceptors. In summary, the shear rates occurring on the surface of the tongue range from $20\,s^{-1}$ to $150\,s^{-1}$ in the investigated cases. These shear rates agree well with the values stated in literature and introduced in section 2.2.4.

4.3.4 Viscosities

Naturally, the viscosity is constant in all the Newtonian cases. On the contrary, it changes in dependence of the present shear rates in the non-Newtonian case CL. This dependency was already discussed by means of equation (3.5) and figure 4.3. For this reason, the viscosity also varies in the model of the oral cavity as several different shear rates arise.

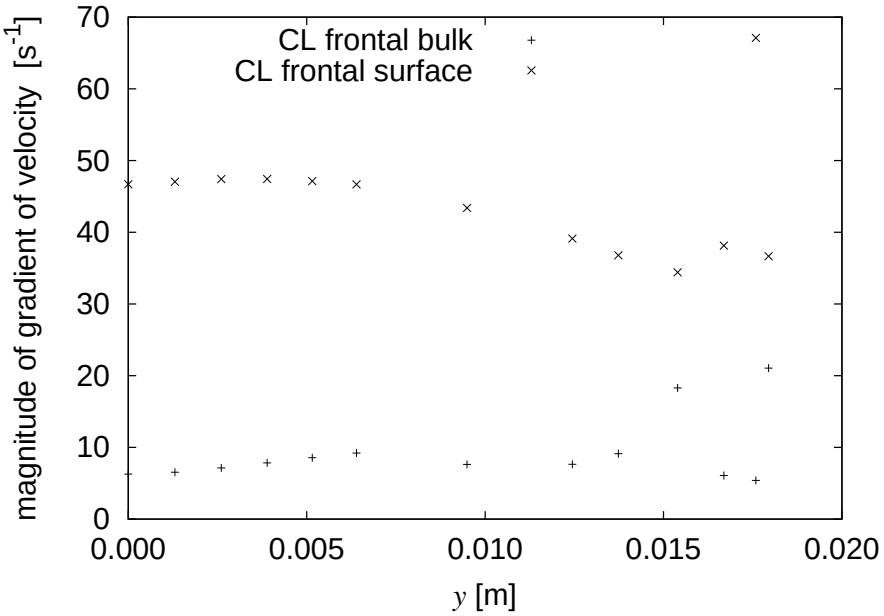

Figure 4.47: The distribution of the magnitude of the gradient of velocity in the middle of the bulk and at the surface of the model tongue in the frontal plane along the y-axis, for high-viscosity fluids using case CL as an example.

Figures 4.48 and 4.49 present quantitative data in the sagittal and frontal planes, respectively. Both figures show that the viscosity is almost constant at about $9 \cdot 10^{-4}$ m^2/s at the surface of the model tongue. This is an almost thousandfold-higher viscosity than water exhibits. The viscosity in the bulk is even higher. The highest values of about $5.6 \cdot 10^{-3}$ m^2/s, neglecting outliers, are reached at the tip of the model tongue. Considering the frontal slice, the values tend to decrease with an increasing distance from the center of the geometry.

It can be concluded that a thin layer develops in which the viscosity is significantly lower than in the rest of the bolus. This makes the food slide better over the surface. Janssen et al. (2007) refer to lubricating layers or shear planes due to relative low viscosities and assume that this effect results in a heterogeneous mouthfeel. However, they ascribe the lower viscosities to the presence of saliva, not to pure fluid mechanics.

Seizing the suggestion of Christensen (1979) introduced in section 2.2.4 that consumers evaluate an averaged viscosity, the question arises as to how this averaged viscosity is constituted. Possibly, the kinesthetic sense plays a decisive role in this evaluation as the

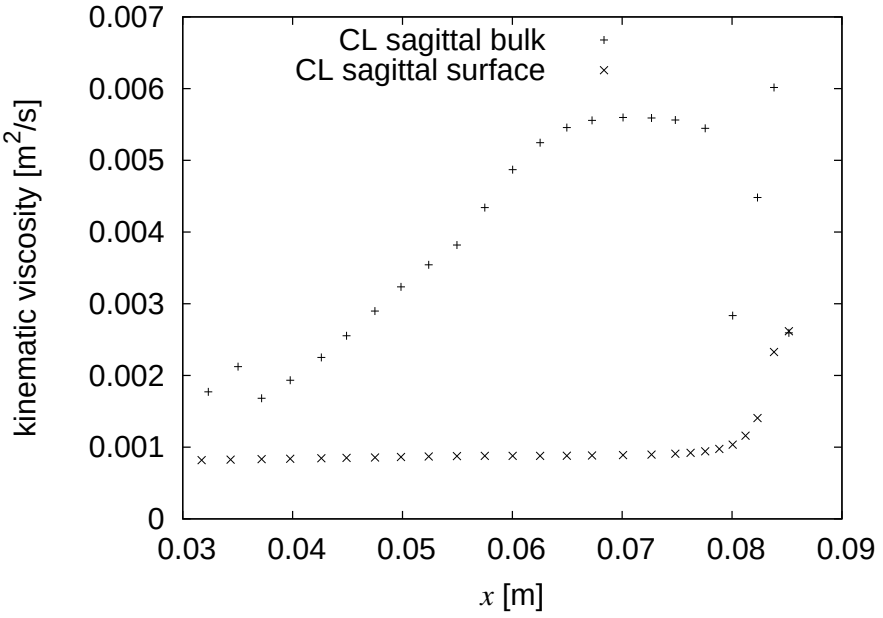

Figure 4.48: The distribution of the viscosity in the middle of the bulk and at the surface of the model tongue in the sagittal plane along the x-axis employing case CL.

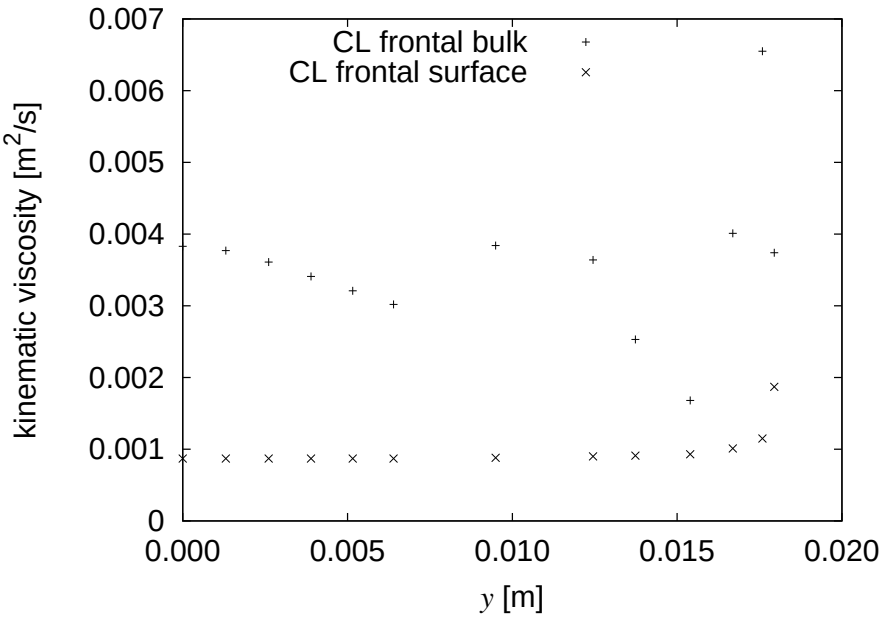

Figure 4.49: The distribution of the viscosity in the middle of the bulk and at the surface of the model tongue in the frontal plane along the y-axis employing case CL.

viscosity-related behavior of the bulk can only be evaluated by motion and the force that is necessary to move the bulk.

4.3.5 Shear Stresses

Shear stresses σ can be calculated by the equation $\sigma = \eta\dot{\gamma}$ where η is the dynamic viscosity and $\dot{\gamma}$ the shear rate. As the dynamic viscosity η is constant for Newtonian fluids, the shear stress is always a specific multiple of the shear rate $\dot{\gamma}$. In the non-Newtonian case, the apparent viscosity changes with the applied shear rate. For this reason, the shear stress depends on the prevailing shear rate $\dot{\gamma}$.

The biggest changes of shear rates and therefore shear stresses take place in the sagittal slice. For this reason, the shear stresses are evaluated in this plane. Additionally, the shear stresses that are detected by the oral mechanoreceptors arise at the surface of the model tongue. Therefore, the evaluation can be further restricted.

Figure 4.50 presents the shear stresses arising at the surface of the model tongue for the cases N1 to N3. Although the shear rates arising in these cases are comparable, the shear stresses are different due to the different viscosities. The lowest maximum shear stress arising in the rear part of the model is 0.15 Pa in case N1. Models N2 and N3 exceed this value by 53% and 207%.

Figure 4.51 shows the distribution of shear stresses for the Newtonian case N4 and the non-Newtonian case CL. The level of the shear stresses is higher in the non-Newtonian case. This observation is not surprising when recalling the fact that the apparent viscosities occurring at the surface of the model tongue are about a thousandfold higher than that of water. Assuming comparable shear rates from $20\,\mathrm{s}^{-1}$ to $150\,\mathrm{s}^{-1}$, the shear stresses developing in a Newtonian fluid exhibiting the viscosity $\eta = 1$ Pas would be about 20 Pa to 150 Pa, which is exactly the range determined by the analytical calculations. These values are larger than those of the non-Newtonian case by about 70%. Therefore, it can be assumed that shear-thinning fluid-flow behavior results in lower shear stresses than Newtonian fluids with comparable apparent viscosities.

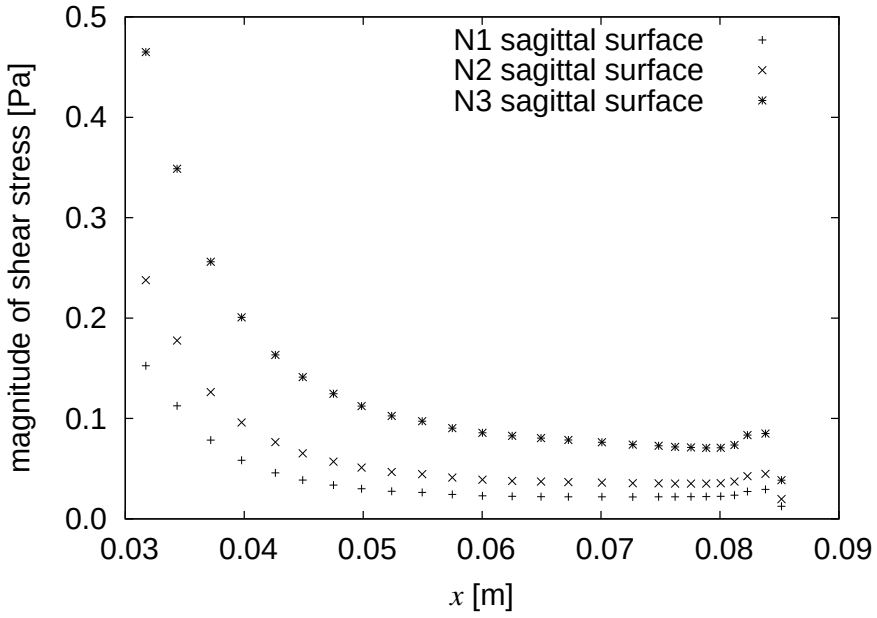

Figure 4.50: The distribution of the magnitude of shear stress at the surface of the model tongue in the sagittal slice along the x-axis for cases N1, N2 and N3.

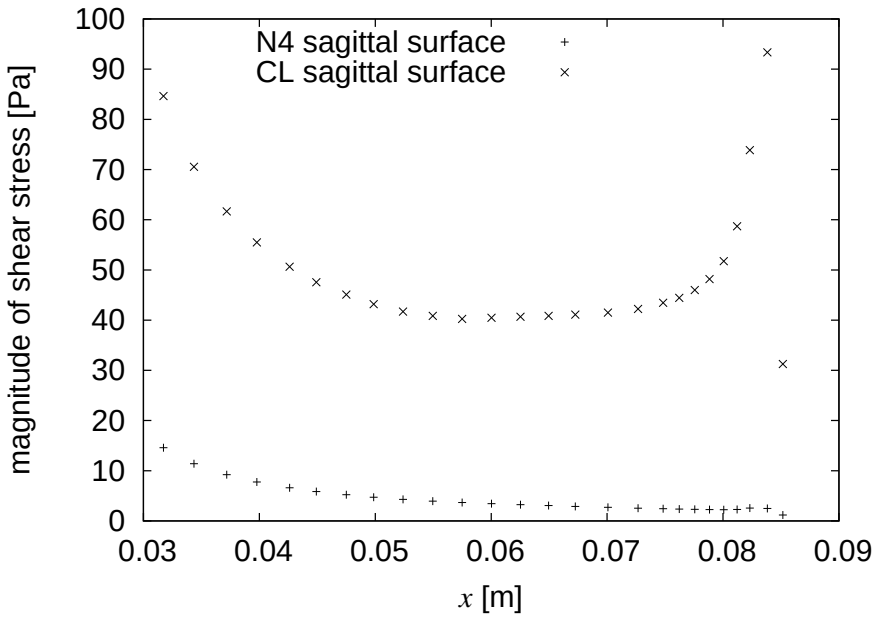

Figure 4.51: The distribution of the magnitude of shear stress at the surface of the model tongue in the sagittal slice along the x-axis employing cases N4 and CL.

Apart from this result, non-Newtonian fluids exhibit a different shear-stress distribution along the x-axis. While the shear stresses increase from the tip of the model tongue to its rear part in Newtonian cases, the shear-rate distribution in the non-Newtonian case is U-shaped due to the altering viscosities. The shear rates near the center of the geometry stay at about 40 Pa, the shear rates at the tip of the model tongue and in the rear part are more than twice as high.

The findings can be compared with the results from the literature presented in section 2.2.4. The previously reported shear-stress ranges amount to 10 Pa to 1000 Pa in general, 4.4 Pa to 131 Pa for syrups, 1 Pa for fresh milk and 683 Pa for chocolate spread. Although the results from the numerical simulation exhibit a smaller minimum value, the order of magnitude agrees well with previous findings.

4.4 Summary of Analytical and Numerical Findings

In the preceding sections novel approaches to investigate the fluid mechanics in the oral cavity during deglutition and the resulting values for different physical quantities have been presented. Table 4.5 compares selected findings from the current analytical and numerical studies as well as the results of previous studies from literature. As the results of the different analytical models and the numerical simulations in the present work take the form of distributions, for comparison with the literature results the maximum value of each quantity for a range of different geometry sizes has been given. The numerical values are taken from case N4, as its viscosity is the same as the one used in the analytical considerations. The physical quantities that are presented are the pressure, velocity, shear rate and shear stress. It can be seen that the analytical and numerical approaches yield similar results, a strong indication of the merits of the two approaches. Their favorable comparison with the literature values is also very encouraging. Hence, the discussed analytical and numerical models offer new possibilities to emulate the fluid flow between the human tongue and palate.

Table 4.5: An overview of the maximum values of the different physical quantities discussed in the current thesis. Pressures are given in Pa, velocities in mm/s, shear rates in s^{-1} and shear stresses in Pa.

Quantity	**Analytical**				**Numerical**	**Literature**
	Case 1	Case 2	Case 3	Case 4	N4	
Pressure	972–3675	1401–3675	141–532	107–1274	1058	1300–7300
Velocity	218	121–250	62	60	220	50–500
Shear rate	870	484–998	174	155/161	150	10–1000
Shear stress	87	48–100	17	16	15	10–1000

Chapter 5

Conclusions

Texture is one of the most important factors of food acceptance besides flavor. However, texture needs to be pointed out to the consumers as it is perceived subliminally as long as it matches their expectancy. Nevertheless, the food industry is interested in a perfect texture in order to win subconscious customer loyalty. Thus, food scientists aim at understanding and objectifying texture perception.

Food texture is a multifaceted attribute. Those attributes have been philosophically discussed for more than 2000 years. The earliest attempt at description dates back to Aristotle who lived in the 4th century BC. He stated in his principle work "Metaphysics" that *"the whole is more than the sum of its parts"*. The modern understanding of this hypothesis is called gestalt psychology. Credited as the founder is Christian von Ehrenfels who published his essay "Über Gestaltqualitäten" (On the Qualities of Form) in 1890.

Food texture follows this concept of gestalt. Texture is not one single attribute but consists of many different properties, which together account for the overall mouthfeel sensation. Nevertheless, it is impossible to investigate texture as a whole without analyzing and understanding its components individually. For this reason, the literature describes a multitude of approaches for understanding textural attributes and their contribution to mouthfeel. These approaches have aimed at analyzing texture by means of measurable quantities to objectifying the descriptors. This knowledge helps the food industry to control and influence

the texture parameters actively, yielding an improvement of products and customer loyalty. Complete knowledge about the interaction of food-texture attributes will be a milestone in food research.

Texture can be understood as a collective term of physics-related terms such as hardness, cohesiveness, viscosity, elasticity and adhesiveness. Of these terms, viscosity is the dominant attribute for foods capable of flowing. For this reason, the current thesis has focused on the enhancement of existing and the development of novel fluid-mechanical models for describing the squeezing flow in the oral cavity during deglutition. The models considered are analytically solvable ones, which have been derived on the basis of the theory of lubrication, as well as numerical models that are based on the geometry of two ellipsoids mimicking the complex dimensions of the human oral cavity.

5.1 Analytical Models

Simple models of the fluid mechanics of thin Newtonian fluid films can be calculated analytically by means of the theory of lubrication. In the context of the current thesis, four different tongue-palate model systems have been introduced and developed on the basis of this theory. These include systems of plane circular parallel plates, plane elliptic parallel plates, plane and curved circular parallel plates, and a sphere in a hemisphere. All these systems have been discussed with regard to squeezing in order to imitate the process of deglutition in a simplified manner. Only the first model has been used as a reference for the squeezing flow in the oral cavity so far. The other models are introduced as tongue-palate model systems for the first time.

The first system of plane circular parallel plates dates back to Stefan's paper "Versuche über die scheinbare Adhäsion" (Experiments on the Apparent Adhesion) from 1874 and was also discussed by Reynolds twelve years later. Until today, the system has been used as the reference to estimate fluid-mechanical quantities occurring in the oral cavity during deglutition. These include the distributions of pressure, velocities, shear rates and

shear stresses as well as the force required to drive the plates together. Obviously, different approximations have to be accepted when employing the model. The human tongue and palate are not circular nor is the fluid film of constant height while the bolus is being squeezed out of the oral cavity. These important factors are taken into account by the other models and studied separately. Nevertheless, the rigid nature of the geometries is a fundamental drawback of this analytical approach.

The model of plane elliptic parallel plates reflects the shape of the projected palate. The derivations of the pressure distribution in the system and the force required to drive the geometries together also date back to Reynolds (1886). As far as is known, the equations for the other physical quantities have been derived for the first time.

The model of the plane and curved circular parallel plates is much more recent. Murti developed it in 1975. The model is characterized by an increasing film thickness along the radial coordinate. For this reason, it mimics the squeezing flow in the oral cavity better than the previously introduced models. Again, the derivation was limited to the equations for pressure and force. The current thesis additionally shows the derivations for the equations of the radial velocity component as well as the shear rates and shear stresses.

The last model of a sphere in a hemisphere has for the first time been deduced from the given Reynolds equation in spherical coordinates. A comparable approach cannot be found in literature of any branch of research. It is the best possibility to imitate the squeezing conditions in the oral cavity realistically.

The comparison of the different models shows that the changes in geometry have significant effect on the shapes of distribution and the orders of magnitude of the fluid mechanical quantities. Slightly viscous fluids with a hundredfold-higher viscosity than water have been chosen as a reference. Foods that feature this viscosity include vegetable oils and stirred yogurt. The previously-used reference model introduced by Stefan leads to a parabolic pressure distribution with maximum values of about 1000 Pa to 3700 Pa for the reference viscosity and oral-cavity dimensions. The functions standing for velocity, shear rate and shear stress exhibit linear behavior. The maximum value of velocity at the outflow of the

geometry is in the order of magnitude of 20 cm/s. Here, the velocities have been shown to be independent from the viscosity of the fluid, which does not reflect the true behavior of the system. However, the shear rate and shear stress are dependent on the fluid viscosity, as expected. The shear rates at the surface of the geometry show maximum values up to 900 s^{-1} at the outflow. This results in a shear stress up to 90 Pa. The force required to drive the upper plate of the geometry against the lower one is strongly dependent on the radius of the plates. It increases with the fourth power of the plate radius. The required force can be as high as 7 N.

The small changes in geometry in the other tongue-palate model systems could be shown to be responsible for significant changes in the different fluid-mechanical quantities. Concerning the pressure, the application of the elliptical configuration results in a decrease of about 10% of the maximum pressures. The effect of a variable film thickness is even bigger. Not only does the maximum pressure drop down by more than 80% and 90% compared to the STEFAN model, respectively, but also the shape of the distribution changes.

The velocity does not change much comparing the STEFAN model with the elliptical geometry. This is different considering the two models with varying film thicknesses. Again, the shape of the distribution changes, in fact more rapidly than for pressure. The function is no longer linearly increasing with the radial and angular coordinate but exhibits a large gradient in the first third of the interval followed by the maximum value of the velocity and a gentle decrease to the outflow of the geometry. The maximum values both decrease to about 6 cm/s, which is about 70% of the STEFAN-model value.

Due to their strong relation with the velocity, the curves for shear rate and shear stress show a similar behavior concerning their shape. The amount of change is also comparable; it sums up to more than an 80% decrease compared to the STEFAN model. Notable is the fact that the absolute values are not the same for both surfaces in the configuration of the sphere and hemisphere. The effect is not big but can be drawn back to the asymmetry of the geometry at the surfaces.

The force required to drive the geometry together stays nearly the same for the elliptical

configuration. It drops down significantly to 0.3 N and 0.5 N for the other configurations. This amounts to values that are about 95% smaller than in the STEFAN model.

Hence, the results of the analytical calculations show that the application of the STEFAN model for the estimation of the profiles and values of the fluid-mechanical quantities in the oral cavity must be called into question. Employing the same geometrical dimensions for each model reveals significant decreases in the analyzed quantities as well as significant changes in the distributions the more complex and the more anatomically realistic the geometries become. For this reason, it is advisable to use the most realistic model of a sphere in a hemisphere as a reference model exclusively.

5.2 Numerical Models

The calculation of the fluid flow through movable ellipsoidal shells takes place by means of numerical analysis. Four different Newtonian viscosities representing water, beer as well as olive oil and the order of magnitude of strongly-sheared yogurt, respectively, and the non-Newtonian CROSS law representing the shear-thinning behavior of yogurt have been implemented. The CROSS law has been chosen for this study as a previously published paper reports on its suitability for yogurt over a wide range of shear rates and on its particular appropriateness in low shear-rate ranges. Moreover, the concept of the more frequently used rheological models featuring yield stress is questionable following an often-cited hypothesis of BARNES & WALTERS (1985). These authors state that no material exhibits yield stress but that only the measurement techniques are too insufficient to record the real material behaviors.

The results of the numerical studies have been visualized by multicolored plots in representative slices of the geometry. Any flow variable can be displayed here. The quantitative evaluation concentrates on defined points of the flow field. They are located in the slices of the semi-minor and semi-major axes of the ellipse projected in the xy-plane. One set of points is located directly at the surface of the model tongue, the other one in the middle of

the bulk.

The maximum pressure calculated numerically is approximately 1000 Pa for a viscosity of 100 mPas. Comparison with the analytical model of a sphere in a hemisphere suggests that quite a small radial clearance of about 4 mm should be chosen to match the analytical and numerical results. Despite the currently chosen clearance of 1 cm for evaluation of the analytical model in line with the other models, the smaller clearance does make sense. The system is rotational symmetrical with regard to the z-axis. This means that there is a gap height of 1 cm around the whole system. In the ellipsoidal model used for the numerical simulations, the film thickness only exhibits this value at one side where the fluid streams out. Consequently, the area of the outflow relative to the volume of the geometry is much smaller. This effect can obviously been compensated by choosing a smaller clearance in the analytical model. Apart from the maximum pressure, the model of a sphere in a hemisphere also shows good agreement with the numerical results of the qualitative pressure distribution. The pressures that can be expected for yogurt lie in the range from 1 to 15 kPa. Comparable pressures are reported in the literature.

The magnitude of velocity ranges from 15 cm/s to 22 cm/s in the middle of the bulk in all cases. This finding is in agreement with the literature. It shows also the same order of magnitude as the analytical calculations of the plane circular parallel plates and the plane elliptic parallel plates. The distribution is not linearly though. Also the velocity distribution determined by the other analytical models does not fit. This observation is not surprising bearing in mind the above mentioned difference of the ratio from the area of the outflow to the squeezed volume. Due to the well-known law of Bernoulli the velocity in the numerical model must increase in comparison to the analytical model of a sphere in a hemisphere. As mentioned in the previous section, the velocities calculated due to the analytical models are not dependent on the viscosity of the fluid. This relationship cancels out in the derivation of the equations. Nevertheless, the effect is present in the numerical investigation leading to slight velocity increases with increasing viscosities. Only the non-Newtonian case does not follow this tendency but only develops velocities comparable to those arising in water.

The higher velocities with higher viscosities in the Newtonian cases are not immediately acceptable. According to the higher inertia effects in the fluid, one would expect lower velocities with increasing viscosities. The clue is the necessity of a constant volume flow in all considered cases. As the streamed areas are constant from case to case, the solution lies in the velocity profiles. In the case of the lower viscosity fluids, the maximum velocity is achieved over wide parts of the cross section. The profile becomes more tapered with increasing viscosities. As the averaged velocity over the cross-section needs to be constant in continuity with the constant volume-flow rate, the magnitude of velocity is necessarily higher for higher viscosity fluids due to the observed profile.

The shear rates that were found lie in the range between 20 s^{-1} and 150 s^{-1}. These results agree well with the literature. Most authors report ranges between 10 s^{-1} and 1000 s^{-1} with an emphasis on the values up to approximately 100 s^{-1}. Naturally, the values that can be found at the surface of the model tongue are higher than those that are observed in the middle of the bulk. The analytical calculations of the geometries featuring increasing fluid-film thicknesses confirm these findings exactly.

The viscosity in the non-Newtonian case varies between 0.9 Pas at the surface of the model tongue and 5.6 Pas in the bulk at the tip of the model tongue. The surface of the tongue is therefore covered by a thin film of constant low viscosity. This finding agrees with the observed high shear rates at the surface of the model tongue. The higher viscosities in the middle of the bulk might be detected by the kinesthetic sense during active manipulation of the food.

The shear stresses are directly proportional to the shear rates in the Newtonian cases. Due to the altering viscosities in the non-Newtonian case the profile changes considerably. Additionally, shear-thinning non-Newtonian behavior reduces the developing shear stresses significantly by about 70% compared to the expected shear stresses in a Newtonian case of comparable viscosity. The shear stresses of all considered models range from approximately 0.01 Pa to 90 Pa. These lie exactly in the range the literature predicts for liquid foods, including yogurt and syrups. The analytical calculations arrive at the same result.

5.3 Mechanoreception

The role of the mechanoreceptors in texture perception needs further clarification. Medical scientists use a different vocabulary for measured quantities than engineers do. For that reason, the data given in the literature are not always clear from the engineering point of view. Moreover, the information about mechanoreception in the mouth is rather small.

Nevertheless, a rough estimation and comparison of detectable and occurring quantities is achievable by calculating the average values of force per area. Considering the mechanoreceptors, the sizes of the receptive fields and the detection thresholds in mN are known (see table 2.4). The forces that are required to drive the analytical models together have been calculated. Additionally, the areas of the geometries can be determined.

The resulting averaged thresholds for the pressure perception are 190 N/m^2 for the SA I receptors, 58 N/m^2 for the SA II receptors and 55 N/m^2 for the RA I receptors. The averaged pressures for the analytical fluid-mechanical models are 1819 N/m^2 for the plane circular parallel plates, 2484 N/m^2 for the plane elliptic parallel plates, 77 N/m^2 for the plane and curved circular parallel plates taking the area of the plane plate, and 69 N/m^2 for the sphere in a hemisphere with respect to the area of the hemisphere.

These estimations show that the detection thresholds of all mechanoreceptors lie under the averaged pressures in the analytical models. Hence, it seems to be reasonable that the superficial mechanoreceptors are partly responsible for the texture evaluation of foods capable of flowing. Additionally, the receptors responsible for the kinesthetic perception will contribute to the texture perception.

5.4 Outlook

Summarizing, the current thesis confirms a multitude of different findings and aspects. The most important result is that the established tongue-palate model system according to STEFAN has been called into question. The newly developed squeezing model of a sphere driving

into a hemisphere brings out values for the fluid-mechanical quantities that are closer to reality. Only the velocity cannot be modeled correctly because of the wrong ratio of streamed outflow area to squeezed volume. Here, the established model yields better values although the geometrical imitation is even worse and also does not include the right area-volume ratio.

Moreover, the current thesis clarifies the fluid-mechanical relationships by bringing together all flow variables and their dependencies. In the future, it is conceivable to intensify the research on non-Newtonian fluid-flow behavior. An extension to the newly found analytical models is imaginable, possibly along the lines of the analytical approach of calculating non-Newtonian fluids between two parallel plates. In the same way, further material laws representing non-Newtonian fluids can be incorporated into the numerical code. The consideration of particle flow would improve considerably the emulation of real food systems. Both approaches would yield a better understanding of different foodstuffs.

A further challenge is the improved emulation of the human tongue. The rigid model does not, of course, mimic the nature of the highly flexible muscular hydrostat realistically. Combining existing simulations of muscle-induced tongue movement with the fluid-mechanical investigations presented in this thesis might be the most powerful simulation technique. Therewith, the vision of a tailored texture that meets all desires comes closer step by step.

Bibliography

ANSYS, 2008. *ICEM CFD*. http://www.ansys.com/products/icemcfd.asp/.

Barnes HA, Walters K, 1985. The yield stress myth? *Rheologica Acta* 24 (4) 323–326.

Böhme G, 2000. *Strömungsmechanik nichtnewtonscher Fluide*. Teubner Verlag, Stuttgart.

Bistany KL, Kokini JL, 1983. Comparison of steady shear rheological properties and small amplitude dynamic viscoelastic properties of fluid food materials. *Journal of Texture Studies* 14 (2) 113–124.

Boliek CA, Rieger JM, Li SYY, Mohamed Z, Kickham J, Amundsen K, 2007. Establishing a reliable protocol to measure tongue sensation. *Journal of Oral Rehabilitation* 34 (6) 433–441.

Bourgin P, Francois JM, Gay B, 1985. Numerical modelling of viscous non-Newtonian effects in lubricating systems. *International Journal for Numerical Methods in Fluids* 5 (9) 831–845.

Bourne MC, 2002. *Food texture and viscosity: concept and measurement*. Academic Press, London.

Buchaillard S, Brix M, Perrier P, Payan Y, 2007. Simulations of the consequences of tongue surgery on tongue mobility: implications for speech production in post-surgery conditions. *International Journal of Medical Robotics and Computer Assisted Surgery* 3 (3) 252–261.

Cameron A, 1966. *The principles of lubrication.* Longmans, London.

Campanella OH, Peleg M, 1987. Lubricated squeezing flow of a Newtonian liquid between elastic and rigid plates. *Rheologica Acta* 26 (4) 396–400.

Chang MW, Rosendall B, Finlayson BA, 1998. Mathematical modeling of normal pharyngeal bolus transport: a preliminary study. *Journal of Rehabilitation Research and Development* 35 (3) 327–334.

Cheer AY, Ogami Y, Sanderson SL, 2001. Computational fluid dynamics in the oral cavity of ram suspension-feeding fishes. *Journal of Theoretical Biology* 210 (4) 463–474.

Chen JS, 2009. Food oral processing - a review. *Food Hydrocolloids* 23 (1) 1–25.

Christensen CM, 1979. Oral perception of solution viscosity. *Journal of Texture Studies* 10 (2) 153–164.

Christensen CM, 1984. Food texture perception. *Advances in Food Research* 29 159–199.

Christensen CM, Casper LM, 1987. Oral and nonoral perception of solution viscosity. *Journal of Food Science* 52 (2) 445–447.

Cook D, Hollowood TA, Linforth RST, Taylor AJ, 2003. Oral shear stress predicts flavour perception in viscous solutions. *Chemical Senses* 28 (1) 11–23.

Cross MM, 1965. Rheology of non-Newtonian fluids: A new flow equation for pseudoplastic systems. *Journal of Colloid Science* 20 (5) 417–437.

Cutler AN, Morris ER, Taylor LJ, 1983. Oral perception of viscosity in fluid foods and model systems. *Journal of Texture Studies* 14 (4) 377–395.

Dantas RO, Kern MK, Massey BT, Dodds WJ, Kahrilas PJ, Brasseur JG, Cook IJ, Lang IM, 1990. Effect of swallowed bolus variables on oral and pharyngeal phases of swallowing. *American Journal of Physiology* 258 (5) G675–G681.

Datta AK, 1998. Computer-aided engineering in food process and product design. *Food Technology* 52 (10) 44–52.

de Wijk R, Terpstra R, Janssen A, Prinz J, 2006. Perceived creaminess of semi-solid foods. *Trends in Food Science & Technology* 17 (8) 412–422.

DeMartine ML, Cussler EL, 1975. Predicting subjective spreadability, viscosity, and stickiness. *Journal of Pharmaceutical Sciences* 64 (6) 976–982.

Dickie AM, Kokini JL, 1983. An improved model for food thickness from non-Newtonian fluid mechanics in the mouth. *Journal of Food Science* 48 (1) 57–65.

Durst F, 2006. *Grundlagen der Strömungsmechanik - Eine Einführung in die Theorie der Strömung von Fluiden*. Springer, Berlin.

Elejalde CC, Kokini JL, 1992. The psychophysics of pouring, spreading and in-mouth viscosity. *Journal of Texture Studies* 23 (3) 315–336.

Engelen L, de Wijk RA, Prinz JF, Janssen AM, Weenen H, Bosman F, 2003. The effect of oral and product temperature on the perception of flavor and texture attributes of semi-solids. *Appetite* 41 (3) 273–281.

Engelen L, van der Bilt A, 2008. Oral physiology and texture perception of semisolids. *Journal of Texture Studies* 39 (1) 83–113.

Engmann J, Servais C, Burbidge AS, 2005. Squeeze flow theory and applications to rheometry: A review. *Journal of Non-Newtonian Fluid Mechanics* 132 (1-3) 1–27.

Ferziger JH, Peric M, 2002. *Computational Methods for Fluid Dynamics*. Springer, Berlin.

Geng JP, Tan KBC, Liu GR, 2001. Application of finite element analysis in implant dentistry: a review of the literature. *Journal of Prosthetic Dentistry* 85 (6) 585–598.

Geraghty R, Butler F, 1999. Viscosity characterization of a commercial yogurt at 5°C using a cup in bob and a vane geometry over a wide shear rate range (10^{-5} s^{-1}-10^{3} s^{-1}). *Journal Of Food Process Engineering* 22 (1) 1–10.

Goenka PK, Booker JF, 1980. Spherical bearings - static and dynamic analysis via the finite-element method. *Journal of Lubrication Technology - Transactions of the ASME* 102 (3) 308–319.

Gradshteyn IS, Ryzhik IM, 1980. *Table of integrals, series, and products*. Academic Press, London.

Hartmann C, Mathmann K, Delgado A, 2006. Mechanical stresses in cellular structures under high hydrostatic pressure. *Innovative Food Science & Emerging Technologies* 7 (1-2) 1–12.

Hasegawa A, Otoguro A, Kumagai H, Nakazawa F, 2005. Velocity of swallowed gel food in the pharynx by ultrasonic method. *Journal of the Japanese Society for Food Science and Technology* 52 (10) 441–447.

Holdsworth SD, 1993. Rheological models used for the prediction of the flow properties of food products: a literature review. *Transactions of the Institution of Chemical Engineers, Part C* 71 (3) 139–179.

Houska M, Valentova H, Novotna P, Strohalm J, Sestak J, Pokorny J, 1998. Shear rates during oral and nonoral perception of viscosity of fluid foods. *Journal of Texture Studies* 29 (6) 603–615.

Jacobs R, Wu CH, Goossens K, van Loven K, van Hees J, van Steenberghe D, 2002. Oral mucosal versus cutaneous sensory testing: a review of the literature. *Journal of Oral Rehabilitation* 29 (10) 923–950.

Janssen AM, Terpstra ME, de Wijk RA, Prinz JF, 2007. Relations between rheological properties, saliva-induced structure breakdown and sensory texture attributes of custards. *Journal of Texture Studies* 38 (1) 42–69.

Johnson KO, 2001. The roles and functions of cutaneous mechanoreceptors. *Current Opinion in Neurobiology* 11 (4) 455–461.

Jowitt R, 1974. The terminology of food texture. *Journal of Texture Studies* 5 (3) 351–358.

Khonsari MM, Booser ER, 2001. *Applied tribology - bearing design and lubrication*. John Wiley & Sons, New York.

Kieser J, Singh B, Swain M, Ichim I, Waddell JN, Kennedy D, Foster K, Livingstone V, 2008. Measuring intraoral pressure: adaptation of a dental appliance allows measurement during function. *Dysphagia* 23 (3) 237–243.

Kilcast D, Eves A, 1991. *Feeding and the texture of food*, chapter Integrating texture and physiology - techniques, pages 167–183. Cambridge University Press, Cambridge.

Kim SM, McCulloch TM, Rim K, 2000. Pharyngeal pressure analysis by the finite element method during liquid bolus swallow. *Annals of Otology, Rhinology & Laryngology* 109 (6) 585–589.

Kitware Inc, 2008. *ParaView*. http://www.paraview.org/.

Knorrenschild M, 2003. *Numerische Mathematik - Eine beispielorientierte Einführung*. Fachbuchverlag Leipzig im Carl Hanser Verlag, München.

Kokini JL, Cussler EL, 1983. Predicting the texture of liquid and melting semi-solid foods. *Journal of Food Science* 48 (4) 1221–1225.

Kokini JL, Kadane JB, Cussler EL, 1977. Liquid texture perceived in the mouth. *Journal of Texture Studies* 8 (2) 195–218.

Komiyama O, de Laat A, 2005. Tactile and pain thresholds in the intra- and extra-oral regions of symptom-free subjects. *Pain* 115 (3) 308–315.

Komiyama O, Kawara M, de Laat A, 2007. Ethnic differences regarding tactile and pain thresholds in the trigeminal region. *The Journal of Pain* 8 (4) 363–369.

Kowalczyk W, Hartmann C, Delgado A, 2004. Modelling and numerical simulation of convection driven high pressure induced phase changes. *International Journal of Heat and Mass Transfer* 47 (5) 1079–1089.

Krulis M, Rohm H, 2004. Adaption of a vane tool for the viscosity determination of flavoured yoghurt. *European Food Research And Technology* 218 (6) 598–601.

Lee WE, Camps MA, 1991. Tracking foodstuff location within the mouth in real-time - a sensory method. *Journal of Texture Studies* 22 (3) 277–287.

Li MJ, Brasseur JG, 1993. Non-steady peristaltic transport in finite-length tubes. *Journal of Fluid Mechanics* 248 129–151.

Li MJ, Brasseur JG, Dodds WJ, 1994. Analyses of normal and abnormal esophageal transport using computer simulations. *American Journal of Physiology* 266 (4) G525–G543.

Lorentz HA, Schmidt GC, 1922. *Lehrbuch der Differential- und Integralrechnung*. Barth, Leipzig.

Mathmann K, Kowalczyk W, Delgado A, 2009. Development of a hybrid model predicting the mouthfeel of yogurt. *Journal of Texture Studies* 40 (1) 16–35.

Mathmann K, Kowalczyk W, Petermeier H, Baars A, Eberhard M, Delgado A, 2007. A numerical approach revealing the impact of rheological properties on mouthfeel caused by food. *International Journal of Food Science & Technology* 42 (6) 739–745.

Meng Y, Rao MA, Datta AK, 2005. Computer simulation of the pharyngeal bolus transport of Newtonian and non-Newtonian fluids. *Food and Bioproducts Processing* 83 (C4) 297–305.

Meyer D, 2003. Reynolds equation for spherical bearings. *Journal of Tribology - Transactions of the ASME* 125 (1) 203–206.

Middleman S, 1998. *An introduction to fluid dynamics - principles of analysis and design*. Wiley, New York.

Miquelin CA, Braga FJHN, Dantas RO, Oliveira RB, Baffa O, 2001. Pharyngeal clearance and pharyngeal transit time determined by a biomagnetic method in normal humans. *Dysphagia* 16 (4) 308–312.

Mörike KD, Betz E, Mergenthaler W, 1997. *Biologie des Menschen*. Quelle & Meyer, Wiebaden.

Muller HG, 1969. Mechanical properties, rheology, and haptaesthesis of food. *Journal of Texture Studies* 1 (1) 38–42.

Mullineux G, Simmons MJH, 2008. Influence of rheological model on the processing of yoghurt. *Journal Of Food Engineering* 84 (2) 250–257.

Murti PRK, 1975. Squeeze films in curved circular plates. *Journal of Lubrication Technology - Transactions of the ASME* 97 (4) 650–652.

Najji B, Bousaid B, Berthe D, 1989. New formulation for lubrication with non-Newtonian fluids. *Journal of Tribology - Transactions of the ASME* 111 (1) 29–34.

Nicosia MA, 2007. A planar finite element model of bolus containment in the oral cavity. *Computers in Biology and Medicine* 37 (10) 1472–1478.

Nicosia MA, Robbins J, 2001. The fluid mechanics of bolus ejection from the oral cavity. *Journal of Biomechanics* 34 (12) 1537–1544.

OpenCFD Ltd, 2008. *OpenFOAM*. http://www.opencfd.co.uk/.

Parkinson C, Sherman P, 1971. The influence of turbulent flow on the sensory assessment of viscosity in the mouth. *Journal of Texture Studies* 2 (4) 451–459.

Peiran Y, Shizhu W, 1990. A generalized Reynolds equation based on non-Newtonian flow in lubrication mechanics. *Acta Mechanica Sinica* 6 (4) 289–295.

Peleg M, 1993. Tailoring texture for the elderly - theoretical aspects and technological options. *Critical Reviews in Food Science and Nutrition* 33 (1) 45–55.

Peleg M, 2006. On fundamental issues in texture evaluation and texturization: A view. *Food Hydrocolloids* 20 (4) 405–414.

Pinkus O, 1987. The Reynolds centennial - a brief history of the theory of hydrodynamic lubrication. *Journal of Tribology - Transactions of the ASME* 109 (1) 2–20.

Pollen NR, Daubert CR, Prabhasankar R, Drake MA, Gumpertz ML, 2004. Quantifying fluid food texture. *Journal of Texture Studies* 35 (6) 643–657.

Rao MA, 1977. Rheology of liquid foods - a review. *Journal of Texture Studies* 8 (2) 135–168.

Reynolds O, 1886. On the theory of lubrication and its application to Mr. Beauchamp Tower's experiments, including an experimental determination of the viscosity of olive oil. *Philosophical Transactions of the Royal Society of London* 177 (1) 157–234.

Richardson RK, Morris ER, Ross-Murphy SB, Taylor LJ, Dea ICM, 1989. Characterization of the perceived texture of thickened systems by dynamic viscosity measurements. *Food Hydrocolloids* 3 (3) 175–192.

Roberts BJ, 1977. A study of the viscosity of saliva at different shear rates in dentate and edentulous patients. *Journal of Dentistry* 5 (4) 303–309.

Schlutt B, Moran N, Schieberle P, Hofmann T, 2007. Sensory-directed identification of creaminess-enhancing volatiles and semivolatiles in full-fat cream. *Journal of Agricultural and Food Chemistry* 55 (23) 9634–9645.

Schmidt RF, 1998. *Neuro- und Sinnesphysiologie*. Springer, Berlin.

Schmidt RF, Lang F, Thews G, 2005. *Physiologie des Menschen mit Pathophysiologie*. Springer, Heidelberg.

Schuenke M, Schulte E, Schumacher U, 2006. *Atlas of Anatomy - General Anatomy and Musculoskeletal System*. Thieme, Stuttgart.

Shama F, Sherman P, 1973. Identification of stimuli controlling the sensory evaluation of viscosity: II. Oral methods. *Journal of Texture Studies* 4 (1) 111–118.

Sherman P, 1970. *Industrial rheology: with particular reference to foods, pharmaceuticals, and cosmetics*. Academic Press, London.

Spurk JH, Aksel N, 2007. *Strömungslehre: Einführung in die Theorie der Strömungen*. Springer, Berlin.

Stanley NL, Taylor LJ, 1993. Rheological basis of oral characteristics of fluid and semi-solid foods: A review. *Acta Psychologica* 84 (1) 79–92.

Stefan J, 1874. Versuche ueber die scheinbare Adhaesion. *Sitzungsberichte der mathematisch-naturwissenschaftlichen Classe der Kaiserlichen Akademie der Wissenschaften* 69 (1-4) 713–735.

Steffe JF, 1996. *Rheological methods in food process engineering*. Freeman Press, East Lansing.

Stevens SS, Guirao M, 1964. Scaling of apparent viscosity. *Science* 144 (362) 1157–1158.

Strassburg J, Burbidge A, Delgado A, Hartmann C, 2007. Geometrical resolution limits and detection mechanisms in the oral cavity. *Journal of Biomechanics* 40 (16) 3533–3540.

Suwonsichon T, Peleg M, 1999. Rheological characterisation of almost intact and stirred yogurt by imperfect squeezing flow viscometry. *Journal of the Science of Food and Agriculture* 79 (6) 911–921.

Szczesniak AS, 1963. Classification of textural characteristics. *Journal of Food Science* 28 (4) 385–389.

Szczesniak AS, 1979. *Food Texture and Rheology*, chapter Classification of mouthfeel: characteristics of beverages, pages 1–20. Academic Press, London.

Szczesniak AS, 2002. Texture is a sensory property. *Food Quality and Preference* 13 (4) 215–225.

Szczesniak AS, Kahn EL, 1971. Consumer awareness of and attitudes to food texture. I: Adults. *Journal of Texture Studies* 2 (3) 280–295.

Takahashi T, Nitou T, Tayama N, Kawano A, Ogoshi H, 2002. Effects of physical properties and oral perception on transit speed and passing time of semiliquid foods from the mid-pharynx to the hypopharynx. *Journal of Texture Studies* 33 (6) 585–598.

Tanaka E, Detamore MS, Tanimoto K, Kawai N, 2008. Lubrication of the temporomandibular joint. *Annals of Biomedical Engineering* 36 (1) 14–29.

Trulsson M, Essick GK, 1997. Low-threshold mechanoreceptive afferents in the human lingual nerve. *Journal of Neurophysiology* 77 (2) 737–748.

Tyle P, 1993. Effect of size, shape and hardness of particles in suspension on oral texture and palatability. *Acta Psychologica* 84 (1) 111–118.

Unsworth A, Dowson D, Wright V, 1975. Some new evidence on human joint lubrication. *Annals of the Rheumatic Diseases* 34 (4) 277–285.

Vallbo AB, Johansson RS, 1984. Properties of cutaneous mechanoreceptors in the human hand related to touch sensation. *Human Neurobiology* 3 (1) 3–14.

van Aken GA, Vingerhoeds MH, de Hoog EHA, 2007. Food colloids under oral conditions. *Current Opinion in Colloid & Interface Science* 12 (4-5) 251–262.

Verhagen JV, Engelen L, 2006. The neurocognitive bases of human multimodal food perception: Sensory integration. *Neuroscience & Biobehavioral Reviews* 5 (30) 613–650.

Vogt F, Lloyd JE, Buchaillard S, Perrier P, Chabanas M, Payan Y, Fels SS, 2006. Efficient 3D finite element modeling of a muscle-activated tongue. *Lecture Notes in Computer Science - Biomedical Simulation* 4072 19–28.

Wakabayashi N, Ona M, Suzuki T, Igarashi Y, 2008. Nonlinear finite element analyses: advances and challenges in dental applications. *Journal of Dentistry* 36 (7) 463–471.

Weinstein AM, Klawitter JJ, Anand SC, Schuessler R, 1976. Stress analysis of porous rooted dental implants. *Journal of Dental Research* 55 (5) 772–777.

Weller HG, Tabor G, Jasak H, Fureby C, 1998. A tensorial approach to computational continuum mechanics using object-oriented techniques. *Computers in Physics* 12 (6) 620–631.

Williams T, Kelley C, 2008. *Gnuplot*. http://www.gnuplot.info/.

Wolff R, Kubo A, 1996. A generalized non-Newtonian fluid model incorporated into elastohydrodynamic lubrication. *Journal of Tribology - Transactions of the ASME* 118 (1) 74–82.

Wolfram, 2008. *Mathematica online integrator*. http://integrals.wolfram.com/.

Wood FW, 1968. *Psychophysical studies on the consistency of liquid foods*. S.C.I. Monograph No. 27: Rheology and texture of foodstuffs. Staples Printers Limited, London.

Yang W, Fung TC, Chian KS, Chong CK, 2007. Finite element simulation of food transport through the esophageal body. *World Journal of Gastroenterology* 13 (9) 1352–1359.

Zürcher C, Kursawe R, 1973. Das rheologische Verhalten einiger Würze- und Bierinhaltstoffe. *Proceedings of the EBC Congress* 14 445–462.

Zur KB, Genden EM, Urken ML, 2004. Sensory topography of the oral cavity and the impact of free flap reconstruction: A preliminary study. *Head & Neck* 26 (10) 884–889.

Appendix A

Peer-reviewed Papers

Hartmann C, Mathmann K, Delgado A, 2006. Mechanical stresses in cellular structures under high hydrostatic pressure. *Innovative Food Science & Emerging Technologies* 7 (1-2) 1–12.

Mechanical stresses and deformation of cellular structures due to the application of high hydrostatic pressure (HHP) is analysed for two cases. In the first case, a liquid-filled spherical shell with linear elastic material properties is considered as first approximation of a biological cell. The theoretical analysis reveals the existence of severe non-hydrostatic mechanical stresses in the wall of the structure. As second case, a nonlinear model of a yeast cell (*Saccharomyces cerevisiae*) under high hydrostatic pressure is assessed by use of the finite-element method. It is observed that hydrostatic stress conditions are preserved in the interior part of the cell, while nonhydrostatic stress is encountered in the cell wall. There, von-Mises stress reaches its critical value upon failure (70±4 MPa) at a pressure load between 415 MPa and 460 MPa. This confirms observations of cell wall damage at this pressure as reported earlier by other authors.

Mathmann K, Kowalczyk W, Petermeier H, Baars A, Eberhard M, Delgado A, 2007. A numerical approach revealing the impact of rheological properties on mouthfeel caused by food. *International Journal of Food Science & Technology* 42 (6) 739–745.

In contrast to the static chemoreceptor-related flavour perception, texture of food capable of flow is detected dynamically with oral mechanoreceptors while the food is manipulated in the mouth. The resulting sensation called mouthfeel strongly depends on the different physical properties of food. Aim of the current study is to determine numerically the occurring fluid mechanical forces in food suspensions using a simplified tongue-palate model system consisting of two parallel plates. For this purpose, the equations of fluid and particle motion are numerically solved by using structured overlapping grids. In the computational experiment, a density neutral fluid system between the plates is compressed by moving the upper plate with constant velocity down to the other one. It has been found that suspended particles move with the fluid flow but have only minor effect on the global flow field in the applied concentration.

Mathmann K, Kowalczyk W, Delgado A, 2009. Development of a hybrid model predicting the mouthfeel of yogurt. *Journal of Texture Studies* 40 (1) 16–35.

Texture perception and mouthfeel are sensory variables that still need further clarification. A reliable method to describe mouthfeel quantitatively by means of physicochemical measurements is missing so far. The current study focuses on a better understanding of the texture perception of yogurt. The final aim of the study consists of the development of a novel hybrid model, which is able to predict mouthfeel sensations objectively. For this purpose, cognitive methods are used in order to merge underlying data pools with respect to process parameters and the composition of dry matter content. These employed data pools result from rheological characterizations as well as sensory analyses of yogurt and from numerical simulations of fluid flow in a simplified anatomical model of the human mouth. This paper introduces the exact procedure of the study. Furthermore, the methods for generating the underlying data pools are described, and the results are presented.

Appendix B

Calculation of the Arc of Circle

One of the analytical approaches is based on the consideration that the fluid streams in an arc. Figure B.1 shows this concept illustrated for the sagittal plane. The arc of the circle that is relevant for further calculations is marked in red. It is characterized by the three key points $P_1(0\,\text{mm}|0\,\text{mm})$, $P_2(58\,\text{mm}|0\,\text{mm})$ and $P_3(29\,\text{mm}|16\,\text{mm})$.

The equation of a circle,

$$(x - x_M)^2 + (y - y_M)^2 = r^2, \tag{B.1}$$

allows the calculation of the central point M and the radius R_2. The equation is converted equivalently into

$$x^2 + y^2 + 2\underbrace{(-x_M)}_{a}x + 2\underbrace{(-y_M)}_{b}y + \underbrace{x_M^2 + y_M^2 - r^2}_{c} = 0 \tag{B.2}$$

for that purpose. Then a system of linear equations is built up relying on the key points in the sagittal plane. Taking P_1 directly brings $c = 0\,\text{mm}^2$, taking into consideration P_2 yields $a = -29\,\text{mm}$ and setting P_3 into the remaining equation leads to $b = 18.28\,\text{mm}$. Hence, the central point is $M(29\,\text{mm}| - 18.28\,\text{mm})$ and the radius $R_2 = 34.28\,\text{mm}$.

In order to determine the length of the arc of the circle between the key points P_1 and

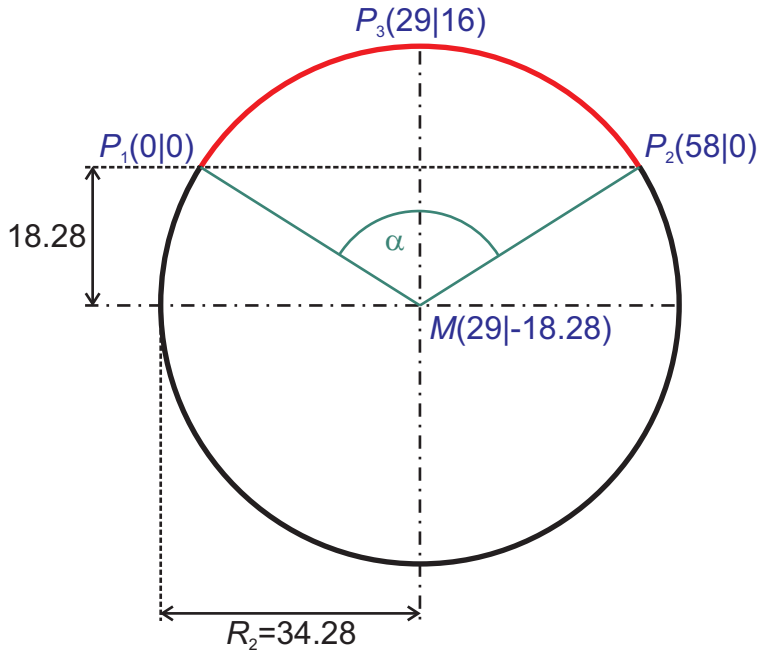

Figure B.1: The circle constructed through the key points of the sagittal plane (all values are given in mm).

P_2, the angle α needs to be calculated. The relationship $\cos\frac{\alpha}{2} = \frac{18.28\,\text{mm}}{34.28\,\text{mm}}$ gives $\alpha = 115.55°$. Employing the equation

$$b = 2\pi r\frac{\alpha}{360°} \tag{B.3}$$

for the calculation of the length of the arc of the circle results in $b = 69.13\,\text{mm}$. Therewith, the radius or semi-major axis adopts the rounded-up dimension $R_{\text{a2}} = 35\,\text{mm}$.

Performing the same procedure for the frontal plane results in the radius $R_1 = 18.13\,\text{mm}$. The angle α is 166.53° and the length of the arc of the circle $b = 52.68\,\text{mm}$. Consequently, the radius or semi-minor axis has the rounded-down value $R_{\text{a1}} = 26\,\text{mm}$.

Appendix C

Code nonNewtonianIcoDyMFoam

```
#include "fvCFD.H"
#include "dynamicFvMesh.H"
#include "incompressible/singlePhaseTransportModel/singlePhaseTransportModel.H"

// * * * * * * * * * * * * * * * * * * * * * * * * * * * * * * * * * * * * * * * * * * * * //

int main(int argc, char *argv[])
{
#   include "setRootCase.H"
#   include "createTime.H"
#   include "createDynamicFvMesh.H"
#   include "initContinuityErrs.H"
#   include "createFields.H"

// * * * * * * * * * * * * * * * * * * * * * * * * * * * * * * * * * * * * * * * * * * * * //

    Info<< "\nStarting time loop\n" << endl;

    while (runTime.run())
    {
#       include "readPISOControls.H"
#       include "readTimeControls.H"
#       include "CourantNo.H"

        if (mesh.moving())
        {
            phi += fvc::meshPhi(U);
        }
```

```
#       include "setDeltaT.H"

        runTime++;

        Info<< "Time = " << runTime.timeName() << nl << endl;

        bool meshChanged = mesh.update();

        if (meshChanged)
        {
#           include "correctPhi.H"
        }

        if (mesh.moving())
        {
            phi -= fvc::meshPhi(U);
        }

#       include "UEqn.H"

        // --- PISO loop

        for (int corr=0; corr<nCorr; corr++)
        {
            rUA = 1.0/UEqn.A();

            U = rUA*UEqn.H();
            phi = (fvc::interpolate(U) & mesh.Sf());

            adjustPhi(phi, U, p);

            for (int nonOrth=0; nonOrth<=nNonOrthCorr; nonOrth++)
            {
                fvScalarMatrix pEqn
                (
                    fvm::laplacian(rUA, p) == fvc::div(phi)
                );

                pEqn.setReference(pRefCell, pRefValue);
                pEqn.solve();

                if (nonOrth == nNonOrthCorr)
                {
```

```
                phi -= pEqn.flux();
            }
        }

#       include "continuityErrs.H"

        if (mesh.moving())
        {
            // Make the fluxes relative
            phi -= fvc::meshPhi(U);
        }

        U -= rUA*fvc::grad(p);
        U.correctBoundaryConditions();
    }

    runTime.write();

    Info<< "ExecutionTime = " << runTime.elapsedCpuTime() << " s"
        << "  ClockTime = " << runTime.elapsedClockTime() << " s"
        << nl << endl;
}

Info<< "End\n" << endl;

return(0);
}
```